Perturbative and ab-initio calculations of electrical susceptibilities of atoms

by

Andrew Spott

B.S. Physics, University of Washington, 2010

M.S. Physics, University of Colorado, 2014

A thesis submitted to the
Faculty of the Graduate School of the
University of Colorado in partial fulfillment
of the requirements for the degree of
Doctor of Philosophy
Department of Physics
2017

This thesis entitled:
Perturbative and ab-initio calculations of electrical susceptibilities of atoms
written by Andrew Spott
has been approved for the Department of Physics

Prof. Andreas Becker

Prof. Agnieszka Jaroń-Becker

Date

The final copy of this thesis has been examined by the signatories, and we find that both the content and the form meet acceptable presentation standards of scholarly work in the above mentioned discipline.

Spott, Andrew (Ph.D., Physics)

Perturbative and ab-initio calculations of electrical susceptibilities of atoms

Thesis directed by Prof. Andreas Becker

Perturbative nonlinear optics consists of many powerful predictive theoretical methods, including the perturbative series of observables related to the interaction of light with matter. The light intensity limits of such series have been studied in the past for highly nonlinear processes such as above threshold ionization and high harmonic generation. A more recent debate focuses on the limits of applicability of perturbation theory for the nonlinear electrical susceptibility and the nonlinear index of refraction of atoms, which are important parameters to study, for example, for filamentation of laser pulses in nonlinear media.

In this thesis we analyze theoretical predictions for the electrical susceptibility of atoms for the transition from the perturbative to the nonperturbative intensity regime. To this end, we apply a numerical basis state method that allows us to perform respective calculations in the framework of perturbation theory as well as using ab-initio methods. The results let us identify the intensity at which the application of perturbation theory breaks down. Furthermore, we provide an analysis of the nonlinear susceptibility as a function of time during the interaction with the laser pulse and find that theoretical predictions are in good agreement with recent experimental data.

To my family: my brother Alex and my parents Tom and Sherry, and to my love Alejandra.

Acknowledgements

No man is an island, and I am no exception. A large part of this thesis has only been completed due to the support of those around me.

Much of a PhD is learning the process and techniques of research, as well as the research itself. Towards this, I am in debt to the members of my research group for their help. Dr. Michelle Miller was an invaluable sounding board of ideas and thoughts, in particular with regards to presenting and writing the results when they occurred. Cory Goldsmith proved a crucial sounding board and compatriot when discussing science. Without our discussions, this thesis would likely contain much more in the way of small misunderstandings and misinterpretations. Towards the end of this journey, Brynn Reiff and Joel Venzke have been important partners in the musings on physical law that are such an important part of research.

My advisers Andreas Becker and Agnieszka Jaroń-Becker have been instrumental in my success in this endeavor. Their support as scientists – both in the direction of the research and navigating the unknown in the quest for an answer – is a large part of what made me the scientist I have become.

I would also like to thank the other members of my thesis committee: Prof. David Jonas, Prof. Margaret Murnane and Dr. José D'incao. It was a privilege to have them on my committee.

Graduate school is not just about the research however. The mental fortitude to keep returning to solve problems despite setbacks and frustration is made easier with the support of friends and family. Gregory Petropoulos and Daniel Weingarten deserve special mention in this capacity. Their friendship turned what might otherwise be a grind into an enjoyable experience, and I am

very grateful for their friendship.

I would not be here without my parents, who instilled in me the creativity, curiosity, and drive that got me where I am today. For this I am inordinately grateful.

I would like to thank my brother, Alexander, as well. His skill at questioning basic assumptions has ensured my own understanding of physics.

Finally, these acknowledgements would not be complete without thanking Alejandra. She has been with me throughout graduate school, and her unfailing optimism and unending support are supremely appreciated.

Contents

Chapter

Figures

Figure

Chapter 1

Introduction

Laser intensities have been increasing steadily since the first demonstration of the laser in 1960 [1]. The first observation of second harmonic generation soon after [2] started the field of nonlinear optics, which has exploded in the years since, and is now one of the largest areas of active research in physics. Second harmonic generation was described using perturbation theory, denoting the electric field of the laser as a small correction to the Coulomb electric field within the atom. As the laser intensities available to experimentalists increased, the successes of perturbation theory made it a widely used model for describing nonlinear optical processes.

By the late 70's however, the discovery of 'above-threshold ionization' – where many photons are absorbed, bringing electrons above the threshold of the continuum, and creating a series of peaks in the photoelectron spectrum spaced by the photon energy – had firmly marked the intensities where perturbation theory no longer described the physics [3]. At 8×10^{12} Wcm^{-2} and 1 μm, the electric fields used in these experiments were still a hundred times lower than the field strength felt by the electron in the ground state of hydrogen, yet even this small relative field had proven too large for perturbation theory to account for.

Filamentation is an important nonlinear process that has been observed around this intensity, making it an important nonlinear process to understand the transition between perturbative and non-perturbative physics. Filamentation, the confinement and self-guiding of light propagating through a medium due to nonlinear self-focusing, has been around almost as long as the laser itself. The first observation of filamentation was in optically induced damage in glasses using a

Q-switched ruby laser by Hercher in 1964 [4], barely four years after the first demonstration of a laser by Maiman in 1960 [1]. This damage presented as a large pulverized spot, and then a "narrow track emerging from the region of gross damage and pointing in the same direction as the incident light" [4]. This narrow track was referred to as a filament in subsequent papers [5, 6], and thus the field of filamentation was born.

Filamentation, as it relates to long (longer than picosecond scale - 1 ps = 10^{-12} s) pulse lengths, is dominated by optical breakdown. Optical breakdown happens when the laser ionizes enough of the atoms to cause a cascade effect: electrons are ionized and then accelerated by the laser field and so collide with other atoms or its parent ion and ionize more electrons. The generated plasma absorbs much of the energy of the long pulse, preventing long propagation distances. The process of optical breakdown as the ultimate result of self-focusing and filamentation has been well understood since the early 1970s [7]. However, more recently, it was observed that much shorter pulses prevent the development of optical breakdown. In 1995, Braun et al. [8] observed that the intensities of a femtosecond (1 fs = 10^{-15} s) light pulses were increasing with distance: at 10 meters downfield, the intensity was strong enough to cause damage to the mirrors in the experiment, while a mirror placed proximal to the output of the laser would show no damage. This self-focusing and intensity increase was the first long range demonstration of filamentation, and the first of this behavior in air. The long range propagation was soon increased, with 50 meter propagation distance (1996) [9], hundreds of meters (1999) [10] and kilometer distances (2004) [11] following.

Beyond the aforementioned long propagation distances, femtosecond filamentation is a host to a slew of interesting physics. Due to nonlinear self-steepening, where the back of the pulse speeds up in relation to the front due to the smaller index of refraction brought on by ionization, a short light pulse propagating through air will get shorter, as the intensity gradient at the end of the pulse gets stronger [12]. Third harmonic generation, the shortening of the pulse from self-steepening, and a chirping of the pulse from self-phase modulation, combine to broaden the spectra of the pulse, leading to white light generation [13]. Coherent sub-terahertz light is generated transverse to the propagation direction in a process that is not entirely well understood [14].

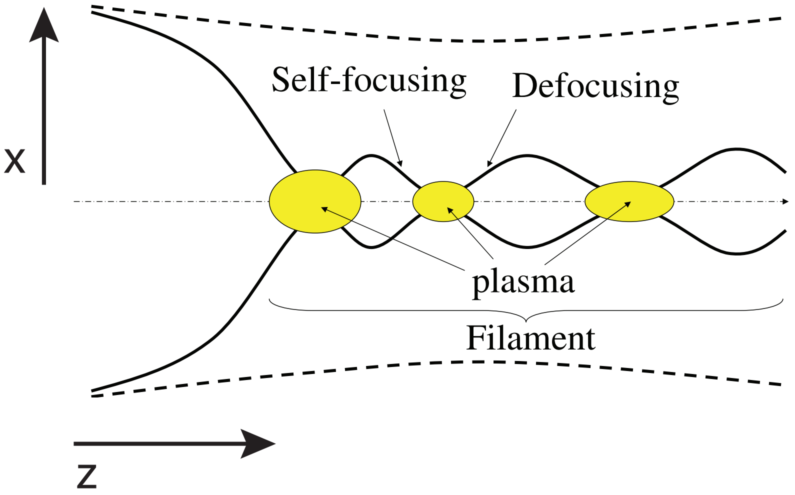

Figure 1.1: The dynamic balance between self-focusing and ionization induced defocusing is shown schematically. The filament is the area after the first initial focusing, while the beam is oscillating between these two regimes. Plasma generation marks the end of the self-focusing regime and the beginning of the defocusing regime. Figure from [15].

The physics of femtosecond filamentation (hereafter referred to as filamentation), is dominated by three processes, schematically shown in Figure 1.1: a) self-focusing, where the beam focuses due to the nonlinear changes in the index of refraction of the medium as the beam propagates; b) ionization, where the beam reaches an intensity large enough to significantly ionize the material that it is traveling through; and finally c) plasma induced defocusing, where the ionized electrons produce a defocusing effect, causing the intensity to decrease until ionization becomes negligible. These three effects interact in a dynamic balance, leading to the phenomenon of filamentation in air and resulting in a long lasting plasma channel behind a so-called “light bullet” [15]. Because the light pulses are so short, absorption by the resultant plasma – the dominant power loss mode of a filament – is limited, in contrast to early picosecond and longer filaments, where the plasma absorption and subsequent optical breakdown lead to drastically shorter filaments.

This balance of self-focusing and ionization induced defocusing defines a maximum intensity in the filament because the ionization prevents the intensity from getting too large, *clamping* the intensity below some material dependent value. Typical measurements have put this clamping at

5×10^{13} Wcm^{-2} for air [16]. This is above the intensity of certain strong laser field effects such as above threshold ionization which was first measured for pulses at intensity of 8×10^{12} Wcm^{-2} [3], and high harmonic generation, first measured for infrared wavelengths in argon at 10^{13} Wcm^{-2} [17]. These processes are well known to be non-perturbative strong-field phenomena. Thus, we expect that the intensity range that filamentation covers also contains the transition between perturbative and non-perturbative effects. Consequently, the physics of filamentation is interesting because it combines physics that we understand in a perturbative regime: harmonic generation, self-focusing, self-phase modulation, etc.; with physics that one studies in a non-perturbative setting: multi-photon ionization, high harmonic generation. Understanding better the crossover between these two different regimes can give insights to improve models for filamentation. In this thesis, we are focusing on examining this boundary.

To provide further insight into the relevance of the crossover between perturbative and non-perturbative physics we discuss the physics of self-focusing and ionization in more detail.

1.1 Self-focusing

The self-focusing of a laser is caused by an intensity dependent index of refraction for any beam profile that monotonically decreases in intensity from the center. For example:

$$n = n_0 + f(I(r)) \tag{1.1}$$

where f is some monotonically increasing function of the intensity I with a zero intercept, n_0 is the linear index of refraction and r is the cylindrical radius coordinate of the beam. The makes the index of refraction larger in the center than the outside. This larger index of refraction causes the center of the beam to move slower than the outside, changing the local Poynting vector towards the area of greatest intensity, focusing the beam, and so causing a higher intensity.

Typically, this is modeled perturbatively: the function f is approximated by a power series in I, assuming I is small (see Chapter 2 for more information):

$$n \approx n_0 + n_2 I(r) + n_4 I^2(r) + n_6 I^3(r) + \ldots, \tag{1.2}$$

where n_2 is known as the Kerr index. At the intensities where filamentation is in the focusing regime, the series is approximated by the first nonlinear term. This approximation is well supported by experiments (see e.g. [18]).

In order for self-focusing to dominate, and eventually cause ionization, it needs to overpower the defocusing inherent to any light beam – diffraction. Diffraction is fundamentally a Fourier uncertainty relation phenomenon: the transverse momentum of the beam cannot be exactly zero, and thus a transversely localized beam will widen as it propagates in space. It can be shown that the balance of these two phenomena, diffraction and self-focusing, will happen in any beam profile that monotonically decreases in intensity from the center if the *power* is equal to the critical power [19]:

$$P_{\text{cr}} = \beta \frac{\lambda_0^2}{8\pi n_0 n_2}, \tag{1.3}$$

where β is a scalar determined by the beam profile, λ_0 is the central wavelength of the laser in vacuum. For Gaussian beams, β is roughly 3.77 [15]. For initial powers larger than P_{cr}, we get self-focusing, while for initial powers less than P_{cr}, self-focusing will ultimately loose out to diffraction. For argon, which has an n_2 of approximately 1×10^{-19} cm^2/W at 1 atm [20], the critical power at 800 nm is roughly 10^{10} W.

1.2 Ionization

Self-focusing cannot lead to an intensity increase without limits. The ionization of the underlying medium of filamentation clamps the intensity that is possible in a filament. When the intensity gets to a certain point – typically 10^{13} to 10^{14} Wcm^{-2} for air – the underlying medium gets ionized significantly and the resultant plasma defocuses the beam, which decreases the intensity.

This clamping intensity is set by the process by which ionization happens. If the photon energy is comparable to the binding energy of the underlying medium the beam is propagating in, then ionization happens fast and the pulse quickly looses energy due to few photon absorption processes before it can propagate very far. This corresponds to well understood perturbative ionization. Conversely, when the binding energy is much larger than the photon energy many photons need to be simultaneously absorbed to overcome the ionization threshold and the corresponding probability for multiphoton absorption is very low until the intensity is large enough to ionize the material.

The intensity inside the filament is not easy to determine experimentally. One method that has been used in the past by Lange et al. [21] to determine the intensity is to introduce a filament, after propagation through air, into a cell containing argon. Inside this cell, the process of high harmonic generation takes place, and the atoms emit harmonics at odd multiple of the fundamental frequency. The largest harmonic n produced is linked to the intensity by the well established relationship [22]:

$$\hbar n\omega_0 = U_i + 3.2U_p, \tag{1.4}$$

where U_i is the ionization energy of the underlying medium (in this case argon), and $U_p = e^2E^2/4m_e\omega_0^2$, where $\omega_0 = c/2\pi\lambda_0$, is the ponderomotive energy of the electron in the laser field. With this method Lange et al. found the peak intensity of a filament to be roughly 5×10^{13} Wcm^{-2}, in agreement with numerical simulations [21].

At a high enough intensity, the atom or molecule undergoing multiphoton absorption will not absorb just enough photons to ionize, but will also have some probability of absorbing additional photons, resulting in the so-called continuum to continuum transitions of the involved electrons. This behavior is popularly known as above threshold ionization [3], and its observation marked the breakdown of perturbation theory. The breakdown intensity of the lowest non-vanishing order of perturbation theory occurs for near optical wavelengths at 5×10^{12} Wcm^{-2} [23]. This is the first indication that the ionization in filamentation has to be considered as a non-perturbative process.

High-order harmonic generation itself is another well known non-perturbative phenomena. In high harmonic generation, photons are absorbed by the electron well beyond the energy needed to ionize the atom, and then the electron is recombined with the parent ion, releasing a photon with energy equivalent to the number of photons absorbed by the electron during ionization. Rather than the perturbative behavior of low-order harmonic generation, where only a few photons are absorbed (typically for a total energy below the ionization threshold), and the probability of absorbing more photons exponentially decays with the number of photons absorbed, high-order harmonic generation generates photons with energy $n\omega_0$ and $(n+1)\omega_0$ with approximately the same probability.

The ionization of the underlying medium adds a defocusing term to the susceptibility. This term is typically modeled as a negative correction to the index of refraction that is proportional to the density of free electrons [15]:

$$\Delta n \approx -\frac{\rho}{2\rho_c}, \tag{1.5}$$

where ρ is the electron density, and $\rho_c \equiv \epsilon_0 m_e \omega_0^2 / e^2$ is the critical plasma density – the density above which it becomes opaque. This term causes a defocusing of the beam, leading to a decrease in intensity. This decrease in intensity eventually halts the process of ionization, which restarts the cycle, putting the beam back into the intensity regime that leads to self-focusing. The multiphoton absorption and ionization of the pulse is the primary loss mechanism of a very short filamentation pulse.

1.3 Higher order Kerr effect (HOKE)

Femtosecond filamentation has been around long enough that much of the basic physics has been thought to be explored. However, in 2009, Loriot et al. challenged the traditional picture of filamentation as *ionization* arrested self-focusing [24]. Instead they proposed that the higher order – greater than two – Kerr terms had a negative value, leading to defocusing due to the saturation and inversion of the Kerr effect as a dominant effect, rather than ionization [25]. They did so by extracting the higher order Kerr terms from the observation of the index of refraction using a cross polarization measurement that they claimed to be insensitive to the plasma contributions. As seen in Table 1.1, from their analysis they found that the higher order terms had alternating signs: n_4 was negative, n_6 was positive again, n_8 negative, and n_{10} positive. This led them to propose that one could describe filamentation without ionization and plasma defocusing. Bejot

Gas	N_2	O_2	Ar	Air
n_2 (10^{-7}cm^2/TW)	2.2 ± 0.4	3.2 ± 0.7	2.01 ± 0.19	2.4 ± 0.6
n_4 (10^{-8}cm^4/TW^2)	-0.16 ± 0.08	-1.55 ± 0.16	-0.11 ± 0.31	- 0.45 ± 0.9
n_6 (10^{-9}cm^6/TW^3)	0.56 ± 0.06	1.9 ± 0.2	1.6 ± 0.2	0.84 ± 0.09
n_8 (10^{-11}cm^8/TW^4)	-2.2 ± 0.2	-10.5 ± 0.7	-8.6 ± 0.5	-4.0 ± 0.3
n_{10} (10^{-13}cm^{10}/TW^5)	-	-	5.3 ± 0.3	-
I_{inv} (TW/cm^2)	33	19	26	26

Table 1.1: The higher order Kerr effect values from [24] for various air components and argon.

et al. then performed a simulation of femtosecond pulse propagation that showed that one could get defocusing, and filamentation, without ionization using the above mentioned higher order Kerr effect values [25].

This new model of filamentation generated a significant amount of discussion. Béjot et al. and others did further theoretical studies of the consequences of higher order Kerr terms [25–28]. Others tried to extract the nonlinear susceptibilities from full *ab-initio* time dependent Schrödinger equation solutions on a grid [29, 30], or to calculate the nonlinear indices using the strong-field approximation [31, 32]. Kolesik et al. took a different path, and simulated the third and fifth harmonic yield assuming only a third order susceptibility or the whole series of higher order Kerr terms [33], this led them to propose a benchmark measurement for the differences between the yields of the third and fifth harmonics. This benchmark was tested, but inconclusive results are reported in [34, 35]. Therefore the result by Loriot et al. remained controversial because it challenged our understanding of the filamentation process, and asked questions about the validity of the perturbative series expansion at intensities that are present in filamentation.

Basic calculations for the values of the various terms of the perturbative series raise questions about the convergence of the index of refraction series extracted in these experiments. Using the values from the paper by Loriot et al. [24], for typical intensities of filamentation (10 TWcm^{-2} to 100 TWcm^{-2}), we can examine the series as:

$$n_{\text{Ar}}(I = 10\text{TWcm}^{-2}) \approx 1 + 2\times10^{-6} - 0.11\times10^{-6} + 1.6\times10^{-6} - 8.6\times10^{-7} + 5.3\times10^{-8}, \quad (1.6)$$

$$n_{\text{Ar}}(I = 100\text{TWcm}^{-2}) \approx 1 + 2\times10^{-5} - 0.11\times10^{-4} + 1.6\times10^{-3} - 8.6\times10^{-3} + 5.3\times10^{-3}, \quad (1.7)$$

and from the increasing values we see that this perturbative series may fail to converge at intensities relevant to filamentation. This raises the question: is the physics of filamentation accurately described by the perturbative higher order Kerr effect?

1.4 Thesis Outline

In Chapter 2, we present a brief overview of perturbative nonlinear optics, focusing on the areas relevant to our study of the degenerate susceptibilities for comparison with our nonperturbative calculations. We start with a discussion of the principles of perturbation theory, and then from there extract out the response functions and the susceptibilities, being careful to ascribe physical meaning to the different terms where appropriate. Finally, we discuss our direct calculation of the susceptibilities, and how these susceptibilities relate to the indexes of refraction used in the higher order Kerr effect terms.

In Chapter 3, we introduce the numerical methods we use for the remainder of this thesis. We discuss our method for directly solving the time dependent Schrödinger equation, using a field-free basis set for an atom in an intense laser field. These methods allow us to capture the nonpertubative physics inherent in this situation. We are specifically interested in how our method allows for comparisons with perturbative physics by using the same basis set for both perturbative and nonperturbative calculations.

Chapter 4 presents the comparison of the perturbative and nonperturbative calculations for a few model systems. We show that it is unlikely that the higher order perturbative series is responsible for the saturation and defocusing seen in filamentation. We further examine the third and fifth harmonic perturbative series, in response to Kolesik et al. [33], examining where the *ab-initio* calculation diverges from the perturbative calculation.

Chapter 5 discusses results from our time dependent susceptibility calculations. We are interested in examining the susceptibility of an atom interacting with a laser field, as a function of time within that laser field. This is applicable to filamentation studies, and high harmonic generation phase matching. We examine the susceptibility of helium at the intensity regime where we previously found the divergence between the *ab-initio* calculations and the perturbative series calculations, with a focus on the features that arise as we reach the threshold of this divergence.

Finally, we will conclude with a summary of the work performed, and a brief outlook towards future work.

Chapter 2

Theory

The higher order Kerr effect (HOKE) relies on the perturbative expansion of the refractive index in a power series, describing the self-interaction of light at a given frequency. Here, we examine the electric susceptibility as a proxy for the index of refraction in general, and HOKE specifically. The information in this Chapter has been discussed in many books and articles; for a good phenomenological overview, see Boyd [18], and for a strong theoretical grounding, see Butcher and Cotter [36].

2.1 Index of refraction

The index of refraction is a macroscopic quantity relating the phase velocity v of an electric field in a medium to that of light in a vacuum, c:

$$n = \frac{v}{c}, \tag{2.1}$$

For all media, the index of refraction is dependent on the frequency of the electric field of interest. This frequency dependence arises from resonances at high frequency (typically visible light), and vibrations, rotations, ionic polarization, etc. for low frequencies (infrared, microwave and radio-frequency wavelengths).

Changes in the index of refraction that are not parallel to the direction of propagation lead to a modification of the direction of the propagating wave. This is best known as Snell's law for an abrupt change in the index of refraction. At the boundary of the alteration, Snell's law gives:

$$n_\alpha \sin(\theta_\alpha) = n_\beta \sin(\theta_\beta), \tag{2.2}$$

where n_α (n_β) is the index of refraction in the first (second) medium, and θ_α (θ_β) is the angle of the direction of propagation with respect to the normal of the interface between the two media. The ray within the medium with the larger index will have the smaller angle. In a regime with a continuously varying index of refraction this makes rays of light bend towards regions with a high index of refraction, a property that is useful in gradient index lenses and is also responsible for the self-focusing in filamentation.

For large electric field strengths, the index of refraction is no longer independent of the field strength. The optical Kerr effect is due to an intensity dependent index of refraction. In the literature, the Kerr effect is frequently limited to the first nonlinear term of the perturbation series in intensity, however the recently discussed [24] higher order Kerr effect refers to the expansion to all higher order perturbative terms:

$$n(\omega) = n_0(\omega) + n_2(\omega)I(\omega) + n_4(\omega)I^2(\omega) + n_6(\omega)I^3(\omega) + \ldots, \tag{2.3}$$

where n is the total index of refraction, n_0 is the linear index of refraction, $n_2(\omega)$ is the first order term of the Kerr effect (typically referred to as the Kerr effect in the literature), n_4 and above are the higher order Kerr effect, and I is the intensity.

The nonlinear index, for a positive coefficient of the dominant term, will lead to self-focusing (where Snell's law directs the local light rays towards the axis of propagation), while for a negative coefficient of the dominant term, de-focusing (where Snell's law directs the local light rays away from the axis of propagation) of the beam will occur. Thus, a negative n_4 and n_8 such as those extracted by Loriot et al. [24] (along with a positive n_2) and discussed in Section 1.3, would lead to a saturation of the index of refraction, as the terms with negative coefficients reach the same value as the terms with positive coefficients at a certain field strength. As the strength of the negative terms rises faster with intensity, this would eventually lead to an intensity regime with a negative slope for the index of refraction as a function of intensity and ultimately to a defocusing of the beam.

The index of refraction is related to the single atom susceptibility through the relation:

$$n^2(\omega) = 1 + N\chi(\omega), \tag{2.4}$$

where χ is the single atom susceptibility of the material and is parameterized by frequency ω. N is the number density of atoms in the material, and n is the total index of refraction for the material at frequency ω. As shown below, the single atom susceptibility is related to the dipole moment and hence the time-dependent wavefunction of the system. It is therefore a quantity that is theoretically accessible from first principles. On the other hand the index of refraction is a macroscopic quantity that describes the interaction of light with an ensemble of atoms. Note that for the remainder of this thesis, we are concerned with the single atom susceptibility – where the number density of the material has been divided out. This is in contrast to some nonlinear optics textbooks, which are concerned with the macroscopic susceptibility.

Transitioning between the terms of the nonlinear index of refraction and the terms of the nonlinear susceptibility is not particularly difficult. We can expand the total susceptibility and total index of refraction in Equation (2.4) into their respective perturbative power series:

$$(n_0+n_2\left|E\right|^2+n_4\left|E\right|^4+n_6\left|E\right|^6+\dots)^2 = 1+N\chi^{(1)}+3N\chi^{(3)}\left|E\right|^2+10N\chi^{(5)}\left|E\right|^4+35N\chi^{(7)}\left|E\right|^6+\dots, \tag{2.5}$$

where the prefactors stand for the degeneracy that we will discuss later in this Chapter. Note, for the rest of this thesis, that the superscript in parentheticals ((n)) denotes the nth order term in the perturbation series of a certain frequency. The electric field is related to the intensity via:

$$\left|E\right|^2 = \frac{I}{2n_0\epsilon_0 c}, \tag{2.6}$$

where n_0 is the linear part of the index of refraction, and ϵ_0 is the electrical permittivity of vacuum. The power series can be formulated in either powers of $|E|^2$ or powers of I, Equation (2.3) is given in terms of I. Collecting terms with the same dependence on $|E|^2$ gives us the first few terms of the index of refraction in terms of these susceptibilities:

$$n_0 = \sqrt{1 + N\chi^{(1)}}, \tag{2.7a}$$

$$n_2 = \frac{3N\chi^{(3)}}{4n_0}, \tag{2.7b}$$

$$n_4 = \frac{10N\chi^{(5)} - 4n_2^2}{8n_0}, \tag{2.7c}$$

$$n_6 = \frac{35N\chi^{(7)} - 16n_2 n_4}{12n_0}. \tag{2.7d}$$

We are primarily interested in the role of the higher order terms, in particular how the terms of the series in Equation (2.3) behave as the intensity increases. Our analysis shows that the susceptibility series and the index of refraction series are closely related, allowing us to use the expansion for the susceptibility as an appropriate proxy for the behavior of the index of refraction. We also note that any calculation of the perturbative index of refraction terms must be done through the susceptibilities, which makes the latter a more natural quantity for a theoretical analysis.

2.2 General properties of the electrical susceptibility

The electrical susceptibilities are used to describe the frequency dependent response – in the form of the dipole moment – of an atom (or other form of matter) to a driving electric field. In the simplest case, for a linear system, the susceptibility is the frequency dependent factor of proportionality between the electric field strength and the dipole moment:

$$\mathbf{p}(\omega) = \langle \hat{\mu} \rangle = \chi(\omega)\mathbf{E}(\omega) \tag{2.8}$$

with the driven dipole moment having an amplitude of $2\,|\chi(\omega)|\,|E(\omega)|$, and a phase angle of $\arg(\chi(\omega)) + \arg(E(\omega))$.

More generally, for a susceptibility that is not confined to be linear, and an electric field $\mathbf{E}(t)$, with Fourier components $E_j(\omega)$, that is not confined to be a continuous wave, a total susceptibility is related to the polarization by:

$$P_i(\omega) = Np_i(\omega) = N\chi_{ij}(\omega; \mathbf{E}(t))E_j(\omega), \tag{2.9}$$

where Einstein summation notation is used, and $\chi_{ij}(\omega; E(t))$ is the total single atom susceptibility tensor acting on the jth component of the electric field, giving rise to the ith component of the dipole moment and polarization. We have denoted P_i as the macroscopic polarization component in the ith direction, and p_i as the dipole moment of a single atom in the ith direction. The implicit dependence of the susceptibility on the total time dependent form of the electric field is present in the total non-perturbative susceptibility, but becomes an explicit dependence on the frequency dependent components of the electric field in the perturbative susceptibility terms. For simplicity, we consider here only with the interaction of the electric field in one, say the z, direction and the polarization induced in the same direction, which removes the tensor indices in the above equation.

The total susceptibility $\chi(\omega; \mathbf{E}(t))$ in Equation (2.9) can be expanded in a perturbative series about the small quantity $E(\omega)$ as:

$$\begin{gathered}\chi(\omega; \mathbf{E}(t))E(\omega_1) = \chi^{(1)}(\omega; \omega_1)E(\omega_1) + \chi^{(2)}(\omega; \omega_1, \omega_2)E(\omega_1)E(\omega_2) + \\ \chi^{(3)}(\omega; \omega_1, \omega_2, \omega_3)E(\omega_1)E(\omega_2)E(\omega_3) + \ldots,\end{gathered} \tag{2.10}$$

where each susceptibility term $\chi^{(n)}$ is parameterized in terms of the frequency ω of the dipole moment it drives and the electric field frequencies ω_j that contribute to that term, where $\omega = \sum_j \omega_j$.

Using Equation (2.10), and Equation (2.9), we can write down the perturbative terms for the expectation value of the dipole moment for some frequency ω as a sum of the contributions due to electric field components at different frequencies:

$$\langle \hat{\mu}^{(n)}(\omega) \rangle = \sum_{\substack{\omega_1 \ldots \omega_n \\ \omega = \omega_1 + \cdots + \omega_n}} \chi^{(n)}(\omega = \sum_{i=1}^{n} \omega_i; \omega_1, \ldots, \omega_n) E(\omega_1) \cdots E(\omega_n), \tag{2.11}$$

where $\hat{\mu}^{(n)}$ is the nth order term in the perturbative expansion of the dipole moment. This gives us a way to obtain the susceptibility terms, given the Fourier decomposition of the perturbative dipole moment terms, by collecting terms.

The *perturbative* expansion of the dipole moment, via the expansion of the susceptibilities, is not always desired. Alternatively, the total susceptibility can be found from *ab-initio* calculations for a given dipole moment and a given electric field as a function of time. By rearranging

Equation (2.9) we get

$$\chi(\omega; E(t)) = \frac{p(\omega)}{E(\omega)} = \frac{\mathcal{F}\left[\langle p(t)\rangle\right](\omega)}{\mathcal{F}\left[E(t)\right](\omega)}, \tag{2.12}$$

where we make explicit that this susceptibility depends on the *time-dependent* electric field, and $\mathcal{F}$ denotes the Fourier transform of its argument, allowing us to convert from an arbitrary time dependent dipole moment to the frequency dependent susceptibility. This is how we extract out the susceptibility from our *ab-initio* calculations.

2.3 Perturbation Theory

2.3.1 Brief review of perturbation theory

We derive the perturbative susceptibilities via the Fourier transform of the time dependent terms of the perturbative dipole moment, i.e. the susceptibility is extracted from Equation (2.11). The perturbative dipole moment terms are found using the time-dependent interaction with the electric field ($H_I(t)$) as a small perturbation to the field-free Hamiltonian H_0. For the expansion we write the corresponding Schrödinger equation as:

$$(H_0 + \lambda H_I(t))\Psi = -i\partial_t \Psi, \tag{2.13}$$

where Ψ represents the wavefunction, λ is a parameter that will be used to denote the orders in the perturbation series, and will be set to 1 at the end of the calculation. If Ψ is expanded into a power series in λ:

$$\Psi = \psi^{(0)} + \lambda\psi^{(1)} + \lambda^2\psi^{(2)} + \dots , \tag{2.14}$$

where $\psi^{(n)}$ is the nth order term in the expansion of the wavefunction Ψ, an application of Equation (2.14) along with Equation (2.13) allows for the collection of terms in powers of λ and the derivation of the recurrence relation (after setting λ to 1) :

$$H_0\psi^{(0)} = -i\partial_t\psi^{(0)} \tag{2.15}$$

$$H_0\psi^{(n)} + H_I\psi^{(n-1)} = -i\partial_t\psi^{(n)}. \tag{2.16}$$

By decomposing the perturbative terms of the wavefunction in terms of the eigenstates ϕ_m of H_0, where $\omega_m = \hbar E_m$ is the frequency associated with that eigenstate:

$$\psi^{(n)} = \sum_m c_m^{(n)}(t)\phi_m e^{-i\omega_m t} \tag{2.17}$$

we obtain a series of recurrent differential equations:

$$\dot{c}_m^{(0)}(t) = 0 \tag{2.18a}$$

$$\dot{c}_m^{(n)}(t) = (i\hbar)^{-1} \sum_k c_k^{(n-1)}(t) \left\langle\phi_m\right| H_I(t) \left|\phi_k\right\rangle e^{i\omega_{mk}t} \qquad \text{for } n \geq 0, \tag{2.18b}$$

which can be recast into integral form as:

$$c_m^{(n)}(t) = (i\hbar)^{-1} \int_{-\infty}^{t} d\tau \sum_k \left\langle\phi_m\right| H_I(\tau) \left|\phi_k\right\rangle c_k^{(n-1)}(\tau) e^{i\omega_{mk}\tau} \tag{2.19}$$

with $c_m^{(0)}$ is the time independent coefficient that defines the initial conditions of the problem.

2.3.2 Dipole moment and single atom response functions

Up until now, the form of the time-dependent perturbation $H_I(t)$ has not been made explicit. We are concerned with the interaction of an atom with an oscillating electric field in this thesis, so we proceed to write the time-dependent dipole moment of the system as the response of the field-free system to an electric field.

For simplicity, we make three assumptions here, which we will discuss in more depth in Section 3.1, as they are of significant importance when solving the *ab-initio* time-dependent Schrödinger equation. First, we choose linear polarization along the $\hat{z}$ direction for the electric field interaction. This reduces the complexity of the following equations, without losing any relevant meaning towards our discussion, and matches the scenarios considered in the *ab-initio* calculations. Second, we assume a single active electron potential, which are used in the *ab-initio* calculations, for obtaining the basis functions (see Section 3.1.1 for more information on the single active electron models). Finally, we use the length gauge for the interaction with the electric field. This simplifies the relationship between the dipole moment and the interaction Hamiltonian, and again matches the *ab-initio* calculations performed in this thesis. The interaction Hamiltonian is thus given by:

$$H_I = -\mu \cdot \mathbf{E}(t) = -\mu E(t) \tag{2.20}$$

and the perturbative expansion of the time dependent dipole moment yields:

$$\begin{aligned}\langle\hat{\mu}\rangle =& \langle\Psi(t)|\,\hat{\mu}\,|\Psi(t)\rangle \qquad (2.21)\\ =& \overbrace{\langle\psi^{(0)}|\,\hat{\mu}\,|\psi^{(0)}\rangle}^{\langle\hat{\mu}^{(0)}\rangle} + \\ & \overbrace{\langle\psi^{(1)}|\,\hat{\mu}\,|\psi^{(0)}\rangle + \langle\psi^{(0)}|\,\hat{\mu}\,|\psi^{(1)}\rangle}^{\langle\hat{\mu}^{(1)}\rangle} + \\ & \overbrace{\langle\psi^{(2)}|\,\hat{\mu}\,|\psi^{(0)}\rangle + \langle\psi^{(1)}|\,\hat{\mu}\,|\psi^{(1)}\rangle + \langle\psi^{(0)}|\,\hat{\mu}\,|\psi^{(2)}\rangle}^{\langle\hat{\mu}^{(2)}\rangle} + \dots\end{aligned}$$

The zeroth order term $\langle\hat{\mu}^{(0)}\rangle$ is the permanent electric dipole moment, which is zero for all centrosymmetric systems including the atomic systems we are studying. The first order correction $\langle\hat{\mu}^{(1)}\rangle$ is the non-zero linear response of the system to the applied electric field. Application of the recurrent relations in Equation (2.19), and the assumption that the system we are studying is prepared in the eigenstate $|g\rangle$, i.e. $\psi^{(0)} = c_g^{(0)}\phi_g e^{-i\omega_g t}$ with $c_g^{(0)} = 1$ and $c_{m\neq g}^{(0)} = 0$, gives the linear term of the dipole moment:

$$\langle\mu^{(1)}(t)\rangle = \int_{-\infty}^{t} d\tau\, \overbrace{\tfrac{1}{i\hbar}\sum_{m\neq g}\hat{\mu}_{gm}\hat{\mu}_{mg}e^{-i\omega_{mg}(t-\tau)}}^{R^{(1)(t-\tau)}}\, E(\tau) + c.c., \tag{2.22}$$

where $\hat{\mu}_{ij} = \langle\phi_i|\,\hat{\mu}\,|\phi_j\rangle$ is the matrix element of the dipole moment operator corresponding to the states denoted by the labels i and j, and $\omega_{ij} = \omega_i - \omega_j$ is the energy difference between these states. Equation (2.22) is the time-dependent convolution of the electric-field response of the atom with the electric field itself. The integration limits ensure that $R^{(1)}(t-\tau)$ is never evaluated for negative arguments and hence causality is guaranteed. Further, the response is constrained to be a function of the difference in time between the current time t and the time τ of the interaction with the electric field, so that the polarization is invariant with respect to a global time offset. The response is a weighted sum of the phase factors of the various eigenstates of the system.

Using

$$E(t) = \sum_{\omega_j=-\infty}^{\infty} E(\omega_j)e^{-i\omega_j t}, \tag{2.23}$$

we can evaluate the integrals by substituting Equation (2.23) in Equation (2.22):

$$\langle \mu^{(1)}(t)\rangle = \sum_{\omega_1} \overbrace{\sum_{m\neq g} \frac{|\hat{\mu}_{gm}|^2}{\omega_{mg}-\omega_1}}^{\chi^{(1)}(\omega_1)} E_0 e^{-i\omega_1 t}. \tag{2.24}$$

The term is proportional to $E(t)$, as is expected for linear polarization. Note, there is a simple pole at $\omega_0 = \omega_{mg}$, related to resonance behavior, when the driving field has the same frequency as the atomic transition. However, Equation (2.24) neglects the lifetimes of the atomic states. When taken into account, the lifetime of a state will broaden the transition and remove the singularity. This effect is frequently approximated by replacing a real ω_{mg} by $\tilde{\omega}_{mg} = \omega_{mg} + i\Gamma_{mg}$, where Γ_{mg} represents the spontaneous decay of the population of the state back to the ground state. This shifts the pole into the complex plane, and therefore removes the singularity. Here, we are only concerned with transitions far from resonance so we do not have to consider this case. Further details on this transformation can be found in [18, 23, 36].

Examining the second order contribution to the polarization, via application of the recurrence relation in Equation (2.19), one can start to see some patterns and the corresponding physical meaning of these terms. Keeping the initial condition the same one gets

$$\langle \mu^{(2)}(t)\rangle = \Big[\langle \psi^{(2)}(t)|\,\hat{\mu}\,|\psi^{(0)}(t)\rangle + c.c.\Big] + \langle \psi^{(1)}(t)|\,\hat{\mu}\,|\psi^{(1)}(t)\rangle \tag{2.25a}$$

$$\begin{aligned} &= (i\hbar)^{-2} \sum_{\substack{m\neq g\\ l\neq g}} \hat{\mu}_{gl}\hat{\mu}_{lm}\hat{\mu}_{mg} \left[\left(\int_{-\infty}^{t} d\tau \int_{-\infty}^{\tau} d\tau' e^{-i\omega_{lg}(\tau'-t)} e^{-i\omega_{ml}(\tau-t)} E^*(\tau)E^*(\tau') + c.c.\right)\right.\\ &\qquad \left. - \int_{-\infty}^{t} E^*(\tau)e^{-i\omega_{lg}(\tau-t)}\, d\tau \int_{-\infty}^{t} e^{i\omega_{mg}(\tau'-t)} E(\tau')\, d\tau'\right]. \end{aligned} \tag{2.25b}$$

Note that the response is symmetric with respect to an interchange of the time variables. In particular, in the case of an electric field of linear polarization, as considered here, such an interchange cannot change the physics of the situation. This property is known as the intrisic permutation symmetry.

The $\langle\mu^{(2)}\rangle$ term consists of an odd number of dipole transition matrix elements. Therefore, the term is zero for centrosymmetric systems because the dipole selection rules for atoms require l to change by ± 1. Thus, an even number of dipole transitions is necessary to result in a non-zero term. Nonetheless, an examination of the form of this dipole term provides us with an understanding for the higher order responses.

The first integral in Equation (2.25b) can be related to two photon sum and difference processes such as second harmonic generation and sum frequency generation. Physically, the integration over τ' establishes a phase difference between the populations in the l state and the g state that evolves with time. The second interaction with the field, which is represented by the integration over τ, modifies this phase difference as the field again interacts with the states. This transition is enhanced if there is an intermediate state m that is close to a frequency of the laser field. Note that this is a property of the second order perturbative wavefunction, which means that this behavior – the sum of two photons – shows up as well in third order and higher order dipole moment terms as an intermediate process. The second integral represents two different states being excited in single-photon processes.

We can evaluate the integrals by substituting Equation (2.23) in Equation (2.25b):

$$\begin{aligned}\langle\mu^{(2)}(t)\rangle = \sum_{\omega_1\omega_2}\sum_{lm}\Bigg(&\frac{\hat{\mu}_{gl}\hat{\mu}_{lm}\hat{\mu}_{mg}}{(\omega_{lg}-\omega_1-\omega_2)(\omega_{mg}-\omega_1)}E(\omega_1)e^{-i\omega_1 t}E(\omega_2)e^{-i\omega_2 t}\\ &-\frac{\hat{\mu}_{gl}\hat{\mu}_{lm}\hat{\mu}_{mg}}{(\omega_{lg}+\omega_2)(\omega_{mg}-\omega_1)}E(\omega_1)e^{-i\omega_1 t}E^*(\omega_2)e^{i\omega_2 t}\\ &+\frac{\hat{\mu}_{gl}\hat{\mu}_{lm}\hat{\mu}_{mg}}{(\omega_{lg}+\omega_2)(\omega_{mg}+\omega_2+\omega_1)}E^*(\omega_1)e^{i\omega_1 t}E^*(\omega_2)e^{i\omega_2 t}\Bigg)\,.\end{aligned} \tag{2.26}$$

The two photon sum process is shown in the first and last terms. The complex exponentials describe a wave with frequency $\omega_1+\omega_2$, while the coefficient is singular for states with frequency $\omega_1+\omega_2$, denoting a maximal transition amplitude. This behavior is enhanced if either ω_1 or ω_2 is resonant with an intermediate state. As mentioned before, due to the lack of modeling of the lifetime of the state, electric field components at on-resonant frequencies will produce unphysical dipole moment terms. The second term describes the difference frequency contribution, where the polarization is at the difference frequency of the two electric field terms. Together, for a two color electric field, the dipole moment will have terms proportional to four different frequency components:

$$-\omega_1+\omega_2 \qquad \omega_1-\omega_2 \qquad \omega_1+\omega_2 \qquad -\omega_1-\omega_2, \tag{2.27}$$

leading to real polarizations with two frequencies: $\omega_1+\omega_2$ and $\omega_1-\omega_2$. When $\omega_1=\omega_2$ a DC contribution and a second harmonic contribution are produced.

Real electric fields have real Fourier coefficients $E(\omega_j)$ such that $E(\omega_j)=E^*(-\omega_j)$. This permits positive and negative frequencies to be swapped without changing the total sum. This freedom allows the electric field and exponential time dependence of Equation (2.26) to be extracted from the sum over the dipole terms:

$$\begin{aligned}\langle\mu^{(2)}(t)\rangle = \sum_{\omega_1\omega_2}\mathcal{P}_I\Bigg[\sum_{lm}&\frac{\hat{\mu}_{gl}\hat{\mu}_{lm}\hat{\mu}_{mg}}{(\omega_{lg}-\omega_1-\omega_2)(\omega_{mg}-\omega_1)}\\ &+\frac{\hat{\mu}_{gl}\hat{\mu}_{lm}\hat{\mu}_{mg}}{(\omega_{lg}+\omega_2)(\omega_{mg}-\omega_1)}\\ &+\frac{\hat{\mu}_{gl}\hat{\mu}_{lm}\hat{\mu}_{mg}}{(\omega_{lg}+\omega_2)(\omega_{mg}+\omega_2+\omega_1)}\Bigg]E(\omega_1)E(\omega_2)e^{-i(\omega_1+\omega_2)t},\end{aligned} \tag{2.28}$$

where the part in square brackets is the susceptibility $\chi^{(2)}(\omega_3=\omega_1+\omega_2)$, which can be seen in Equation (2.11). Note that due to intrinsic permutation symmetry, the order of the electric field terms $E(\omega_1)E(\omega_2)$ does not matter. The symmetry requires that we average over interchange of ω_1 and ω_2, which is represented by the operator $\mathcal{P}_I$. This susceptibility tensor is thus an 2nd order symmetric tensor with a term for every ω_1 and ω_2.

A comparison between the first and second order terms of the dipole polarization shows how the pattern of the third and higher order perturbative terms evolves. The nth term in the perturbative series will have $n+1$ terms in the sum:

$$\langle\mu^{(n)}(t)\rangle=\sum_{m=0}^{n}\langle\psi^{(m)}|\,\hat{\mu}\,|\psi^{(n-m)}\rangle\,. \tag{2.29}$$

The perturbative wavefunction of nth order will contribute an n photon process to the series, along with all intermediate state processes (processes involving $1\ldots n-1$ photons):

$$|\psi^{(n)}\rangle=(i\hbar)^{-n}\sum_{j_n\neq j_0}\cdots\sum_{j_1\neq j_0}\prod_{m=1}^{n}\frac{\mu_{j_m j_{m-1}}E(\omega_m)e^{-i\omega_m t}}{\omega_{j_m j_0}-\sum_{i=m}^{n}\omega_i}\,|\psi_{j_0}\rangle\,, \tag{2.30}$$

where j_m denotes a field-free eigenstate with j_0 denoting the ground (or initial) state.

The nth order perturbative susceptibility term can be found via the same method used for $\chi^{(2)}$ above. This includes an interchange of ω_i with $-\omega_i$ where appropriate to consolidate the electric field terms, and then an extraction of the specific susceptibilities desired.

2.4 Summary

Here we have given an overview of perturbation theory as it applies to the dipole moment and the susceptibility. Since we are interested in adding to the ongoing discussion of the higher order Kerr effect, which was presented as a function of the index of refraction, we discussed the use and relevance of the perturbative susceptibility as a more theoretically accessible quantity.

For the discussion of the relevance of the perturbative approach we derived the first few terms of the dipole moment under a set of certain assumptions – such as a single active electron potential, linear polarization, etc – that we will use throughout this thesis. Each term was discussed with respect to its physical significance. Finally, we discussed the method that we will use in our calculation and analysis of the susceptibilities. Results of this analysis will be presented in Chapter 4.

Chapter 3

Numerical Methods

Solving the time dependent Schrödinger equation (TDSE) for atoms in strong electric fields is challenging, since strong-field ionization and other effects are complex highly nonlinear processes. An electron interacting with a powerful enough laser can simultaneously cause a number of related phenomena including: over the barrier ionization, bound-bound excitation, high harmonic generation, above threshold ionization, dispersion of the ionized electron wavepacket and others. These phenomena interact in unexpected ways, leading to incredibly rich and complex physics. This is part of the excitement of working in this field.

These complex interactions are also what makes it difficult to perform calculations. The wavefunction of an electron interacting with a strong electric field is spread out over a much greater volume than a typical atom in the ground state. This volume must be represented in any calculation that aims to accurately model this interaction.

Furthermore, the Schrödinger equation of an atom in a time dependent strong electric field does not have an exact analytical solution, and the large number of coupled dimensions – three for each electron – combined with the large interaction volume, requires far too much information for a complete computational solution using current computers. Due to the difficulty of the problem, any realistic solution is a balance between three competing factors:

- Numerical and physical accuracy of the method. When dealing with differential equations without known analytical solutions, we can use computers to find a numerical approximation to the exact solution to that differential equation. How closely these approximations are to the exact solution is the numerical accuracy of the method. More accurate methods can be more difficult to calculate, either requiring much more memory or computational power. How accurate the numerical results are must be balanced against the accuracy of the physical model with which one is trying to solve the problem. The accuracy required by the physics that we want to study determines the physical model that we use and the numerical accuracy we require.

- Information extracted from the method, such as physical observables, or quantum mechanical properties we wish to examine. Certain observables are easier to calculate in some methods than in others.
- Time to calculate.

These limitations have become significantly less severe as computational power and algorithmic advances have developed over the last few decades. These advances have allowed theorists to continually push the boundaries of accuracy, and allowed us to examine larger systems or more subtle observables.

In our case, we examine the perturbative and the *ab-initio* solutions to the time dependent Schrödinger equation for an atom in a time dependent electric field. In order to study the limits of the perturbative approach by comparing the respective results to those of ab-initio solutions, we aim to perform both calculations within the same theoretical framework. To this end, we have chosen the representation of the wavefunction in terms of the field-free basis states. Since we are specifically interested in establishing the limits of the perturbative HOKE expansion, this determines the susceptibility as the observable we need to evaluate. The susceptibility is determined via the dipole moment (see section 2.2), which can be well calculated using the basis states. In this Chapter we will present the numerical basis state method used to perform the perturbative and ab-initio calculations of the atomic susceptibilities for the comparison.

3.1 Overview of the method

The Schrödinger equation for a single atom in an oscillating electric field within the dipole approximation and using the length gauge can be written as (in atomic units):

$$\left[\sum_{i=1}^{N}\left(\frac{\mathbf{p}_i^2}{2}-\frac{1}{r_i}+\mathbf{r}_i\cdot\mathbf{E}(t)\right)+\sum_{i\neq j}\frac{1}{|\mathbf{r}_i-\mathbf{r}_j|}\right]\Psi(\mathbf{r}_1,\ldots,\mathbf{r}_N,t)=-i\partial_t\Psi(\mathbf{r}_1,\ldots,\mathbf{r}_N,t), \qquad (3.1)$$

where $\mathbf{p}_i = -i\nabla_i$ is the usual momentum operator for electron i, with position coordinate $\mathbf{r}_i$, interacting with a time dependent electric field vector $\mathbf{E}(t)$ and $\Psi(\mathbf{r}_1,\ldots,\mathbf{r}_N,t)$ is the wavefunction.

The solution of the general Schrödinger equation for atoms with more than two electrons is too computationally intensive for strong-field calculations, and must be reduced before it can be solved in a reasonable amount of time. We make a number of approximations to the multi-electron Schrödinger equation in order to restrict the calculation time and to make efficient the calculations that we are interested in performing.

The approximation with the largest effect on computation time is the single active electron approximation. For hydrogenic systems, this is an excellent approximation: the outer electron is more weakly bound and will thus react to the external electric field more freely than the inner electrons. A good example is Lithium, with two electrons in the inner s-orbital, and a single electron in the outer s-orbital. The outer s-orbital electron exhibits a much weaker (approximately 11 eV less tightly bound) binding energy than the inner electrons. However, even for atoms with more than one electron in the valence shell, such as the noble gas atoms, the single active electron model has been proven reasonably accurate in the past in the case of studies in strong fields. For example, published comparisons between theoretical and experimental studies of the multiphoton ionization of xeon and ATI spectra of argon have shown good agreement using single active electron models [37, 38]. This will be covered in more depth in subsection 3.1.1.

Next, we consider only spherically symmetric potentials in order to work within the separable spherical coordinate system. Spherically symmetric potentials include those atoms with a complete outer electron shell such as noble gases – which are popular for experimental studies of strong field processes – and atoms with an outer s orbital shell, such as alkali atoms and helium. Using spherically symmetric potentials allows us to separate the angular part of the field-free Hamiltonian – with the well known spherical harmonics as solutions – from the radial part. This requirement does limit us from being able to model atoms with incomplete valence p-orbitals or those with higher orbital angular momentum due to the symmetry breaking the corresponding potentials exhibit under the influence of an external electric field. Such potentials have coupled terms between their radial and angular parts, which significantly increases the complexity of the field-free Hamiltonian.

We select a linear polarization direction for the interacting electric field (denoting it $\hat{z}$). This reduces the quantum numbers (and thus the dimensionality) that change during the interaction of the atom with the field via the dipole selection rules to the principal quantum number n and the orbital angular momentum quantum number l. The angular momentum quantum number in the z direction (denoted by m) is fixed by the choice of the initial state (typically we set $m = 0$).

Finally, since we will represent the radial part of the wavefunction on a grid, we need to restrict its size. To this end, we use an infinite spherical well with radius $R_{\text{ max}}$, beyond which the potential is infinite. In practice, we denote this by adding a $BC(r)$ term in the Hamiltonian which fixes the value of the wavefunction at R_{max} to zero, enforcing the boundary condition.

These approximations give us the following form of the TDSE:

$$\left[\frac{p^2}{2} + \widetilde{V}(r) + zE(t)\right]\Psi(r,\theta,t) = i\partial_t\Psi(r,\theta,t), \tag{3.2}$$

where now $\widetilde{V}(r) = V(r) + BC(r)$ is the spherically symmetric single active electron potential plus boundary conditions, $zE(t)$ is the electric field interaction term that is now limited to a linear polarization with $z = r\cos\theta$, and $\Psi(r,\theta,t)$ is the wavefunction parameterized in the three independent coordinates.

3.1.1 Single active electron models

The single active electron (SAE) approximation consists of two parts: the wavefunction of the single propagated (active) electron, and the potential in which it is propagated. Because the SAE approximation assumes that all electrons other than the *active* electron are frozen in their ground

Target	Z_c	a_1	c_1	a_2	c_2	a_3	c_3
He	1.0	1.231	0.662	-1.325	1.236	-0.231	0.480

Table 3.1: The parameters from [43] for the helium atom.

state configuration, the potential in which the active electron is propagated includes contributions from both the bare nuclear charge as well as the frozen electrons.

A SAE potential can be determined by finding the full multi-electron ground state for the atom using a method such as Hartree-Fock [39], or density functional theory [40, 41], and then removing the active electron. The resulting multi-electron wavefunction describes the inactive electrons. The complete potential in which the active electron is propagated results from the electrostatic repulsion of the inactive electrons together with the electrostatic attraction of the core nucleus.

For spherically symmetric potentials, potential energy surfaces found in this way are typically [42, 43] fit to a series of radial Yukawa potentials:

$$V(r) = -\frac{Z_{\text{bare}}}{r} + \sum_n \frac{a_n e^{-c_n r}}{r}, \tag{3.3}$$

where Z_{bare} is the asymptotic bare charge that the electron will see, and a_n and c_n are fits to the calculated potential. In this thesis we have performed calculations for the helium atom using the single active electron potential from Tong and Lin [43], shown in Table 3.1.

3.1.2 Separation of variables

We want to consider a model system that can be used for *ab-initio* time propagation as well as time independent perturbative calculations. This requires the separation of the time dependent Hamiltonian into a time independent Hamiltonian plus the time dependent field interaction, $zE(t)$. The time independent part of the Hamiltonian is then diagonalized, giving us a time independent basis set that we can use for the perturbative calculations, and that we can use as the elements in which we propagate the total time dependent Hamiltonian.

We find the basis state functions of the Schrödinger equation for the time independent Hamiltonian given by:

$$H_0\Psi(\mathbf{r},t) = \left[\frac{-\nabla^2}{2} + \widetilde{V}(r)\right]\Psi(\mathbf{r},t) = -\partial_t\Psi(\mathbf{r},t), \tag{3.4}$$

where $\widetilde{V}(r)$ is the spherically symmetric potential plus boundary conditions. In the spherical coordinate system, this Schrödinger equation is separable, allowing us to write down the solution as a product of functions of different coordinates [44]:

$$\Phi(\mathbf{r},t) = R(r)Y(\hat{r})\Xi(t), \tag{3.5}$$

where $R(r)$ is a function dependent only on the radial distance between the electron coordinate and the nuclear coordinate, $Y(\hat{r})$ depends on the angular coordinate, and $\Xi(t)$ specifies on the time component of the wavefunction. This separation of variables is only possible because our total potential $\widetilde{V}(r)$ depends only on the radial coordinate.

From this, we get three separate equations relating the three components:

$$E = -i\frac{\partial_t\Xi(t)}{\Xi(t)} \tag{3.6}$$

$$l(l+1) = \frac{1}{R(r)}r^2\nabla_r^2 R(r) - 2r^2\left[\widetilde{V}(r) - E\right] \tag{3.7}$$

$$l(l+1) = -\frac{1}{Y(\hat{r})}r^2\nabla_{\hat{r}}^2 Y(\hat{r}) \tag{3.8}$$

where E is the energy eigenvalue, l is the total angular momentum quantum number, ∇_r^2 is the radial part of the Laplacian and $\nabla_{\hat{r}}^2$ is the angular part. This reduces the field-free problem to three eigenvalue problems, two of which have well known solutions. The solution to Equation (3.6) is the exponential time dependence of a state:

$$\Xi(t) = e^{-iEt}, \tag{3.9}$$

while the solution to Equation (3.8) is given by the spherical harmonics:

$$Y_{l,m}(\hat{r}) = Ne^{im\phi}P_{l,m}(\cos\theta), \tag{3.10}$$

where N is a normalization factor, l and m are the total angular momentum quantum number and projected angular momentum quantum number respectively, and $P_{l,m}$ are the associated Legendre polynomials. The radial equation (Equation (3.7)) is now defined in terms of the spherically symmetric potential and boundary conditions.

3.2 Numerical basis state method

The time independent calculation of the eigenstates is simplified by using the spherical harmonics (as discussed in Section 3.1.2). This reduces the calculation to merely finding the radial part of the eigensystem from Equation (3.7):

$$\left[-\frac{\partial_{rr}}{2} + \widetilde{V}(r) + \frac{l(l+1)}{2r^2}\right] R_{n,l}(r) = E_{n,l} R_{n,l}(r). \tag{3.11}$$

The rest of this section is related to the solution of this eigenvalue equation. We start with a general discussion of representations of differential equations in section 3.2.1. In section 3.2.2 we give a brief overview of our numerical method for finding the eigenstates. This leads us into section 3.2.3, where we discuss the free parameters that are useful for the basis. Section 3.2.4 provides details of the algorithm that we use to solve the eigensystem, along with a comparison with analytic results (section 3.2.4.4).

3.2.1 Representations of differential equations

Much work has gone into finding different strategies for solving the time-independent Schrödinger equation [45–47]. Like all problems in applied math, different methods have different strengths and weaknesses. Here we will discuss some of the more common techniques for solving the time independent Schrödinger equation. The general form of the Schrödinger equation for our model is written as:

$$\underbrace{\left[\frac{\mathbf{p}^2}{2m} + \widetilde{V}(r)\right]}_{H_0} \Psi(\mathbf{r}) = E\Psi(\mathbf{r}), \tag{3.12}$$

The first decision that must be made when solving any differential equation is the numerical representation of the solution, and consequently, the differential operator. The wavefunction of an electron is represented as a complex valued function defined over the three dimensional real-valued spatial vector. However, when trying to solve it numerically on machines with finite memory and computational power, we must make choices in order to describe such a function. These choices determine the form of our solution. We are primarily interested in this section with the representation of the eigenfunctions of the time independent Hamiltonian, and will focus our discussion on methods to solve such a system. We will discuss the propagation of the wavefunction in time in section 3.3.

There are many choices one can make on how to represent the wavefunction and the Hamiltonian. These methods generally fall into two different categories: approximations via the discretization of space and approximations via the truncation of series. Below we will give a brief overview of these general methods. In order to simplify our analysis, we restrict ourselves to the eigensystem consisting of the 1-D (radial) time independent Hamiltonian, and the corresponding 1-D radial part of the wavefunction. This matches the problem we are looking to solve.

3.2.1.1 Discretization of space

One way to solve a time-independent differential equation is to discretize the variables [48]. In the case of the Schrödinger equation, this means discretizing the space in which an electron (or a center of mass) is represented. For example, for a Cartesian coordinate system, one defines a grid of points on which the solution is defined, while between these points the solution is inferred. Typically, an evenly spaced grid is used for simplicity, however this is by no means a requirement. For an evenly spaced grid, the distance between adjacent points – the grid spacing – we denote by Δx, and the nth point on the grid is given as x_n. The total number of points is represented by $n_{\max}$.

Derivatives on such a discrete grid are called finite differences, and thus the methods that solve differential equations on a finite grid are called finite difference methods. Finite difference methods are perhaps the simplest of the various methods to solve the Schrödinger equation. In position space, the momentum operator is represented by a derivative $\mathbf{p} = -i\nabla$, and thus the kinetic energy term is proportional to the second derivative. The first derivative of a function $f(x)$

between two adjacent points of a grid is then approximated by:

$$\partial_x f(x) = \frac{f(x+\Delta x) - f(x)}{\Delta x} + O(\Delta x^2). \tag{3.13}$$

Equation (3.13) is referred to as the forward difference, because it approximates the derivative at x using the value of the function at $x + \Delta x$ and x. The backward difference is easily inferred from the forward difference.

Combining the forward difference and backward difference, one gets the central difference for a second order derivative:

$$\partial_{xx} f(x) = \frac{f(x-\Delta x) - 2f(x) + f(x+\Delta x)}{\Delta x^2} + O(\Delta x^2). \tag{3.14}$$

Using this, the time independent Schrödinger equation in one dimension can be written as:

$$\begin{aligned} H\Psi(\mathbf{x}) &= E\Psi(\mathbf{x}) \qquad (3.15) \\ -\frac{1}{2}\frac{\Psi(x_{n-1}) - 2\Psi(x_n) + \Psi(x_{n+1})}{\Delta x^2} + V(x_n)\Psi(x_n) &= E\Psi(x_n). \qquad (3.16) \end{aligned}$$

The boundary conditions are set by fixing the values of $\Psi(x_0)$ and $\Psi(x_{\max})$.

The Hamiltonian H_0 in Equation (3.16) above can be represented as a matrix:

$$H_0 = \begin{bmatrix} \frac{1}{m\Delta x^2} + V(x_1) & -\frac{1}{2m\Delta x^2} & 0 & \cdots & 0 & \\ -\frac{1}{2m\Delta x^2} & \frac{1}{m\Delta x^2} + V(x_2) & -\frac{1}{2m\Delta x^2} & 0 & \cdots & 0 \\ 0 & -\frac{1}{2m\Delta x^2} & \frac{1}{m\Delta x^2} + V(x_3) & -\frac{1}{2m\Delta x^2} & 0 & \cdots \\ \vdots & \ddots & \ddots & \ddots & \ddots & \ddots \end{bmatrix}, \tag{3.17}$$

where the boundary conditions have been fixed via neglecting to add the respective points to the matrix, which is equivalent to setting them to zero. Equation (3.16) can be rewritten as a matrix equation:

$$H_o\mathbf{\Psi} = E\mathbf{\Psi} \tag{3.18}$$

where the wavefunction is now represented as an n dimensional vector. This formulation allows one to use matrix eigenfunction solvers.

The finite difference method in its simplest form is very easy to implement and reason about. For low dimensional calculations, it is compact in its representation, and with a small enough grid, it usually has acceptable errors. Unfortunately, the finite difference method is difficult to adapt to non-uniform grids [48, 49], and with a large number of dimensions, its requirement for a small grid-spacing quickly becomes computationally unfeasible. Finite difference methods are frequently used as well to solve the time-dependent Schrödinger equation, using a finite difference to discretize the time component as well as the space components.

3.2.1.2 Finite series representations

Another method to represent the wavefunction and Hamiltonian is as an abbreviated series. Basic calculus allows one to approximate any well behaved arbitrary function as some finite number of terms in a power series expansion such that the desired accuracy is achieved. More generally, one can represent any well behaved arbitrary function $f(x)$, in this case the wavefunction, as a truncated series in any complete basis S with basis elements $s_n(x)$ (for simplicity, we have restricted ourselves to a discussion in one dimension):

$$f(x) = \sum_n c_n s_n(x), \tag{3.19}$$

where c_n is a coefficient that represents the weight of the individual functions $s_n(x)$ within the sum. This allows one to potentially represent $f(x)$ very accurately in a small amount of memory, given one chooses an appropriate basis set S, such that the number of basis states needed for convergence is small.

This scheme can be expanded to time dependent problems by defining a time dependent coefficient to each basis element:

$$f(x,t) = \sum_n c_n(t) s_n(x). \tag{3.20}$$

A linear operator $\hat{O}$ can be represented within S as a matrix with weighted transitions between basis elements s_n and $s_{n'}$ in some domain $\mathcal{R}$:

$$\hat{O}_{n',n} = \int_{\mathcal{R}} s^{\dagger}_{n'}(x) O(x) s_n(x)\, dx. \tag{3.21}$$

Consequently, the Hamiltonian within the Schrödinger equation can be represented as:

$$\hat{H}_{n',n} = \int_{\mathcal{R}} s^{\dagger}_{n'}(x) H(x) s_n(x)\, dx, \tag{3.22}$$

for a basis set S which consists of orthonormal elements s_n. When S is not orthonormal, then $s^{\dagger}_n$ is no longer the complex conjugate of s_n, and must be constructed out of the overlap matrix (for more information, see [50, 51]).

From a computational perspective, a low memory footprint of the operator is important. There are two properties of an operator that can lead to a low memory footprint: the total number of states needed to accurately represent the wavefunction and the sparseness of the operators acting on such a wavefunction. If one knows, *a priori*, that certain elements will be zero within the matrix, then such elements do not need to be represented, and storage can be reduced.

There is an upfront cost to using a finite series representation. The Hamiltonian must be found within this representation using Equation (3.22) before one can do any further calculations – such as propagation – in this basis. Typically, the Hamiltonian in this form can be saved and used for multiple further calculations. When using the field-free basis, the Hamiltonian must be recalculated for every combination of atomic species and grid that one wishes to use.

A few basis sets are particularly common for *ab-initio* solutions of the time dependent Schrödinger equation in problems in atomic, molecular and optical physics. Each basis set has benefits and drawbacks. In general, the sparsity of the Hamiltonian within the representation – the number of non-zero matrix elements compared to the size of the matrix – and the number of elements of the basis set S necessary to approximate the wavefunction determine the memory and computation required for a calculation.

A common expansion used is the Fourier series [52], where an arbitrary complex function is decomposed as a sum of complex exponentials over the interval of convergence $[x_0, x_0 + P]$:

$$f(x) = \sum_{n=-\infty}^{\infty} c_n e^{i\frac{2\pi n}{P}x}. \tag{3.23}$$

By truncating the series to a finite number of exponentials, the sum represents an approximation of the function. For an atomic, field-free potential, the Fourier representation of the Hamiltonian is very dense: the matrix element between any two frequencies is nonzero, for a typical atomic potential proportional to $-1/x$. Furthermore, the representation of the ground state of a hydrogen atom requires a large number of frequency components to reach convergence to sufficient accuracy. On the other hand, for a free electron without any potential ($H = \mathbf{p}^2/2$), the Hamiltonian is diagonal in the Fourier representation. The Fourier basis functions are eigenfunctions of the kinetic energy term of the Hamiltonian, allowing for an efficient description of the free electron problem within this basis set.

We have already used the spherical harmonics representation in section 3.1.2. For spherically symmetric problems, the angular parts of the wavefunction are easily represented in terms of spherical harmonics. For atoms interacting with an electric field, the dipole transition rules ($l' = l \pm 1$ for the total angular momentum quantum number l and $m - 1 < m' < m + 1$ for the magnetic quantum number m if necessary) give a very sparse matrix representation of the dipole transition operator for single active electron potentials. Since the spherical harmonics are eigenstates of the angular part of the single active electron field-free Hamiltonian, the matrix representing this part of the field-free Hamiltonian is diagonal.

Another widely used method to represent the radial part of a wavefunction are B-Splines [53, 54]. B-Splines are a family of piece wise polynomials defined via the recurrence relation:

$$B_{i,1}(x) = \begin{cases} 1 & \text{if} \quad t_i \leq x < t_{i+1} \\ 0 & \quad\text{otherwise} \end{cases} \tag{3.24}$$

$$B_{i,n}(x) = \frac{x - t_i}{t_{i+n-1} - t_i} B_{i,n-1}(x) + \frac{t_{i+n} - x}{t_{i+n} - t_{i+1}} B_{i+1,n-1}(x), \tag{3.25}$$

where $B_{i,n}(x)$ is the B-Spline of order n defined between the “knot”s t_i and t_{i+k}. These knots can be at arbitrary points within the space that is being used, and multiple knots at the same point can be used to fulfill boundary conditions and allow discontinuities to be represented. This behavior can be seen in Figure 3.1, where each set of lines represents a basis function of order 3 that is centered at different knot points. The locations of the knots are shown at the bottom axis. Notice that at multiple knots (at the far right and far left) a B-Spline may have discontinuous derivatives.

This is useful for representing Neumann boundary conditions and discontinuous potentials.

For a B-Spline basis the accuracy improves as the density of the knots increases, similar to the increased accuracy when decreasing grid point spacing in finite difference schemes. B-Splines are functions with limited support – they are only non-zero within a small number of knots – leading to a sparse representation of the radial part of the Hamiltonian. B-Splines of nth rank are nth order polynomials, which have a well defined nth derivative when defined over n knots with unique locations. Thus, the transition elements of the Hamiltonian can be obtained analytically for an analytical potential. Unfortunately, B-Splines do not form an orthonormal basis, which means that an overlap matrix must be calculated in order to solve the time-independent Schrodinger equation, as mentioned above.

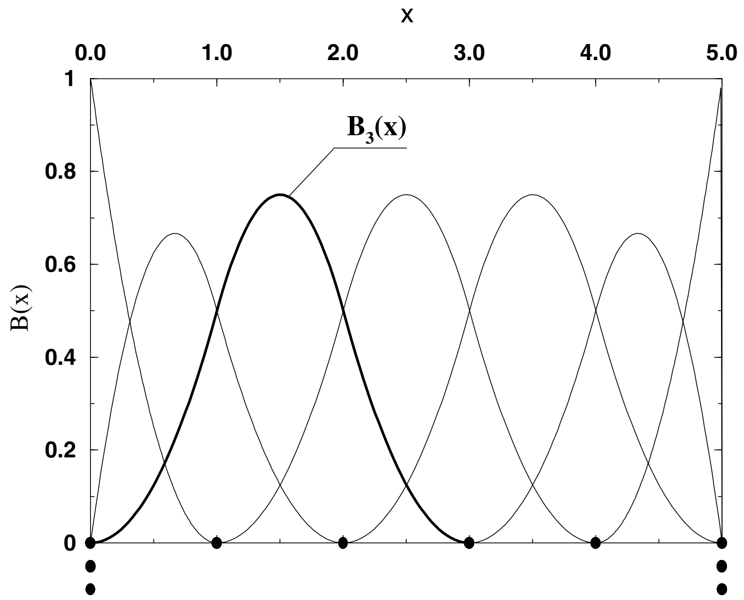

Figure 3.1: All B-Splines of order $n = 3$ for the knot sequence shown by full circles on the bottom axis. Note that multiple knots can be used in order to induce discontinuities in the basis functions. Reproduced from [53].

For strong-field problems, the B-Spline basis is a popular choice. B-Splines, due to their analytically calculable matrix elements, are efficient in both memory and computation. The B-Spline basis functions are used as is (as shown in Equation (3.20)), or as a basis to represent the field-free eigenstates of the system.

TDSE calculations of the ATI spectra of hydrogen [55] was one of the first successful application of B-Splines to the strong-field regime. Since then, B Splines have been used to examine high harmonic generation, fully two dimensional multi-photon ionization of helium, and examinations of single ionization in H^-. For more information on the applications of B-Splines to atomic physics calculations, see [53, 56].

Slater type orbitals are another popular basis set for radial calculations in atomic and molecular physics [47, 57]. They are typically of the form:

$$S_{n,\zeta}(r) = r^{n-1} e^{-\zeta r}, \tag{3.26}$$

where n and ζ are parameters of the basis function. Typically, n is associated with the principal quantum number, while ζ is a tunable parameter which describes the radial extent of the orbit. Slater orbitals were originally investigated due to their similarity to the hydrogenic wavefunctions. The Slater orbitals form a complete basis for a fixed ζ. However, slow convergence can occur for features much farther from the origin than ζr. In order to combat this, it is common for multiple values of ζ to be used in a single calculation, expanding the size of the basis.

Slater type orbitals are typically used in variational calculations of atomic states [57, 58]. This allows basis sizes to be minimized while still maintaining accuracy for single (or few) state calculations. Unfortunately, this variational process produces a new set of basis functions for each new state, which makes calculations of large numbers of states difficult. As the number of nodes in a wavefunction goes up, the number of basis states required also increases. The combination of these two behaviors – the individualized basis states for each state, and the increasing number of basis states necessary for highly oscillatory states – means that Slater type orbitals have not seen much use in strong-field calculations.

Gaussians are another common basis set used in solutions of the atomic and molecular Schrödinger equation [59]. There are a number of different schemes for using Gaussian functions as a basis for finding atomic orbitals [47]. A common one is analogous to the Slater type orbitals:

$$G_{l,\alpha}(x) = r^{l} e^{-\alpha x^2}, \tag{3.27}$$

where α is a parameter defining the width, and l defines the order of the basis element. For a fixed α, the set of Gaussians of different order l forms a complete basis. Unfortunately, a basis set with fixed α is exceedingly slow to converge for most realistic atomic orbitals, and thus multiple basis sets with different α's are used to speed convergence.

Because of this, calculations using Gaussian basis sets are usually made up of composite basis elements, where a linear combination of pure Gaussian basis elements create a set of new basis elements. A common choice is using linear combinations of Gaussians to generate Slater type orbitals. Because Gaussians are simpler to analytically integrate than Slater type orbitals, this makes calculations with Slater type orbitals easier to manage, at the expense of accuracy, as a finite number of Gaussians cannot represent a Slater orbital exactly.

Slater-type orbitals and Gaussian-type orbitals are commonly used in computational chemistry. They can generate very quick, accurate electronic structure calculations of multi-centered molecules due to their natural similarity to real atomic orbitals. Unfortunately, both suffer from difficulty in accurately representing the continuum wavefunctions. This inability to describe the continuum efficiently has decreased their usefulness in strong-field calculations, though some hybrid calculations have been able to utilize these wavefunctions for bound state representations, combining them with more flexible methods for continuum state calculations [60].

3.2.2 Numerical basis state method

We find the field-free basis numerically by solving the eigensystem given by Equation (3.12). The spectra of any unrestricted atom is infinite in the number of bound states as well as the number of continuum states. Of course, this cannot be represented in finite memory, nor calculated with finite computational power. In order to overcome this, we restrict the atomic spectra by confining the atom within an infinite spherical well potential, which discretizes the continuum part of the atomic basis states, and reduces the number of bound states to a finite number. We artificially restrict the number of continuum states by restricting the maximum energy state that we need to represent in our wavefunction.

In practice, the range of the infinite spherical potential is denoted by $R_{\max}$, and a Dirichlet boundary condition is enforced at the boundary, i.e. $\Phi(R_{\max}) = 0$. The value of $R_{\max}$ sets the density of states for the continuum and highly excited bound states. We typically use values of $500 - 1000$ a.u. for our calculations (see section 3.2.3 for more information on how this affects our basis set.)

As noted above, we use the spherical harmonics as angular eigenfunctions, while the radial eigensystem is given by Equation (3.11). We use a finite difference method to find the individual eigenfunctions represented as values on a radial grid. In order to maintain accuracy around the singularity in Equation (3.11), a higher density of points is needed near the singularity, while far fewer are required far from the singularity. Unfortunately, finite difference calculations with nonlinear grid spacing are often plagued by numerical errors. Transforming Equation (3.11) into a logarithmic variable (denoted by x) gives us the required accuracy at small values of r and increases the spacing at higher values of r, while allowing us to maintain an evenly spaced grid. Such a nonlinear grid is accomplished by transforming Equation (3.11) using $x = \log(r)$, and we find the transformed wavefunction $\eta_{n,l}(x) = R_{n,l}(r(x))\sqrt{r(x)}$:

$$\left[-\frac{\partial_{xx}}{2} + \frac{(l+\frac{1}{2})^2}{2} + r(x)^2\left(E_{n,l} - V(r(x))\right)\right]\eta_{n,l}(x) = 0. \tag{3.28}$$

Here, the x coordinate is evenly spaced, while the r coordinate is logarithmically spaced. We have removed the explicit notation of our boundary conditions from the potential, these will be enforced by the numerical method rather than as a term in the potential. This necessitates the need to set a minimum radial distance (denoted $R_{\min}$). In test calculations we have found that $R_{\min} = 10^{-6}$ a.u. leads to accurate representations of the ground state wavefunctions. We constrain this second order differential equation to have a unique solution by fixing the boundary conditions $R_{n,l}(R_{\min}) = R_{n,l}(R_{\max}) = 0$, and ensuring the resulting function $R_{n,l}(r)$ is normalized.

3.2.3 Properties of the basis

There are a number of free parameters that we must decide on when calculating our basis. Here we list the parameters, what impact they have on the calculations, and typical values that we have used in our calculations.

- $R_{\max}$: the largest r value in the grid, defined by the boundary conditions. This determines the spatial extent of the wavefunction and the density of the continuum states. Figure 3.2 shows the energy vs. n of the state for different $R_{\max}$. The quadratic dependence of the energy as a function of n is fairly clear, along with the increased density of states (decreased quadratic coefficient) as $R_{\max}$ increases for fixed n. Unlike typical grid based methods, we do not have an absorber at $R_{\max}$, so we require a very large grid, to avoid reflection problems. The strength of the electric field we can represent is limited by this hard boundary: any part of the wavefunction that reaches the boundary of our grid will be reflected off. Test calculations have shown that a good lower bound on the extent of the grid with respect to electric-field strength E and frequency ω is:

  $$R_{\max} \gtrsim N \frac{\pi}{\omega} \sqrt{20 U_P}, \tag{3.29}$$

  where N is the number of periods of the laser field, ω is the frequency of the laser field and U_p is the ponderomotive potential $E^2/4\omega^2$. An electron that is ionized near the center of the pulse and excited to $10U_p$ (the maximum classical rescattering energy possible in a single cycle [61, 62]) will have just enough momentum to drift to the edge of our box by the end of the pulse. For a 10^{14} W/cm^2 and 800 nm laser, this corresponds to approximately 130 a.u. per 2 cycles of the laser field. We typically use 1000 atomic units as our maximum radius.

- n_{points}: The number of points on the grid. Due to the logarithmic spacing of our grid points, the density is lowest at $R_{\max}$. This restricts the maximum n state that we can represent: higher n states have higher frequencies, and the Nyquist frequency requires that

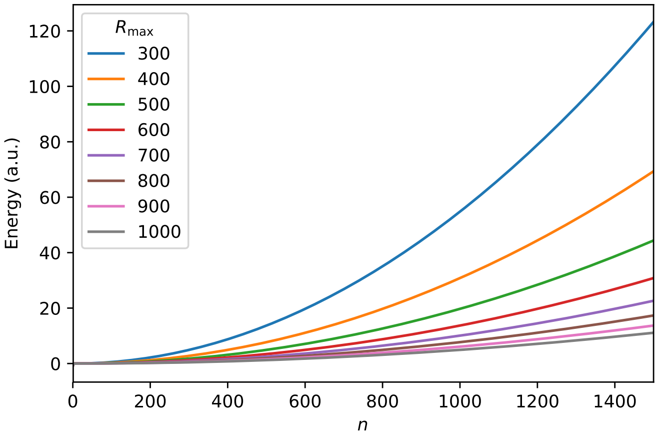

Figure 3.2: Energy as a function of n for different $R_{\max}$ from 300 to 1000. Note the quadratic dependence of E_n as a function of n that becomes more pronounced for smaller $R_{\max}$.

we have at least two points on our grid per period of the wave. Practically speaking, we have found that significantly more points than that must be used to prevent errors both in calculating the states and in integrating the states to find the dipole transitions. We show the effects of using too few points for the wavefunction in Figure 3.3, where the left panel shows the high r part of the wavefunction when too few points are included, and the right shows the same part of the wavefunction when we include enough points. The number of points is functionally limited by the amount of memory available: we use long doubles (16 bytes) for each point in our calculations, so we require at least $n_{\text{points}} * n_{\max} * 16$ bytes of memory per node. Typically, we use $300,000$ points for $n_{\max} = 2000$ and $R_{\max} = 1000$.

- $n_{\max}$: the maximum principal quantum number state that we can represent, which is an upper bound on the energy represented by a given wavefunction. This parameter is limited by the number of points on the grid and $R_{\max}$. A lower bound on the required $n_{\max}$ for an atom interacting with an electric field E with frequency ω is $10U_p = 10E^2/4\omega^2$. For a 10^{14} W/cm^2 and 800nm laser, this corresponds to approximately 3 a.u. For $n_{\max} = 2000$ and $R_{\max} = 1000$, $E_{n=2000} \approx 19$ a.u. The relationship between $R_{\max}$, n and E is shown above in Figure 3.2.

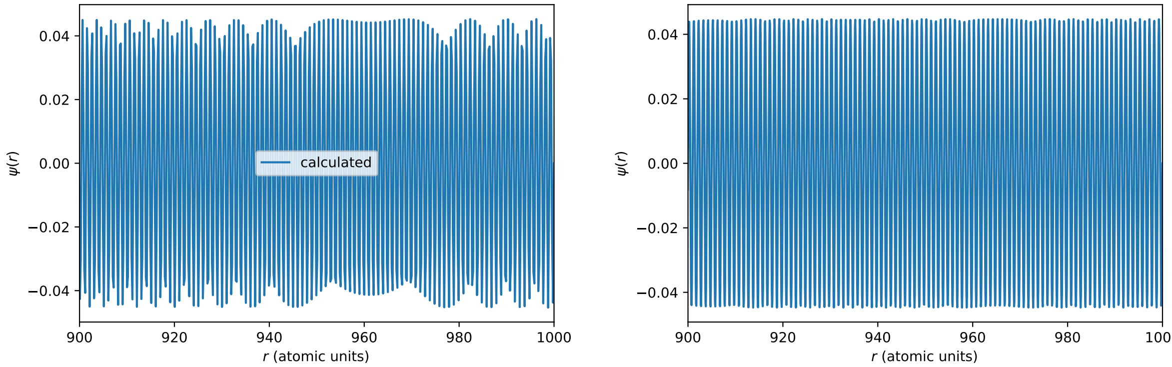

Figure 3.3: A demonstration of aliasing shown for state $n = 2000$, $l = 0$ with $R_{\max} = 1000$, with $100,000$ points on the left as an example of too few points, and $300,000$ points on the right as an example of barely enough. For clarity, only the last 100 a.u. of the wavefunction has been shown. Note the oscillating amplitude for the plot with too few points. This is an example of a state that does not have enough points for an accurate integration when finding the dipole moment.

- $l_{\max}$: the maximum angular quantum number we can represent. Due to the fact that we put our potential inside an infinite spherical well potential, we do not have the accidental degeneracy of the l states [63], and our highest l states have more energy than the corresponding low l states with the same principal quantum number. Typically, we set $l_{\max}$ to 70.

3.2.3.1 Representation in the field-free basis set

We are interested in representing the solution of the Schrödinger equation in the field-free energy basis. Using the radial eigenfunctions and spherical harmonics, any wavefunction can be written as:

$$\Psi(r,t) = \sum_{n,l} c_{n,l}(t) R_{n,l}(r) Y_{l,m}(\hat{r}), \tag{3.30}$$

where $Y_{l,m}(\hat{r})$ are the well known spherical harmonics found in e.g. [64], and m is constant for any given calculation (typically $m = 0$). $R_{n,l}(r)$ are the radial wavefunctions that we found in the previous sections, and $c_{n,l}(t)$ are the time dependent complex coefficients. In the field free basis, we represent the wavefunction $\Psi(t)$ as a vector composed of the complex coefficients $c_{n,l}(t)$. Thus, a wavefunction denoting the ground state of hydrogen is merely $|c_{1,0}(t)| = 1$ and $c_{n\neq 1,l} = 0$. We represent this vector as $\mathbf{C}(t)$.

The time dependent Schrödinger equation for an atom interacting with a oscillating electric field pointing in the z direction can be written down as:

$$\left[\overbrace{-\frac{\mathbf{p}^2}{2} + V(r)}^{H_0} + \overbrace{zE(t)}^{H'(t)}\right]\Psi(r,t) = i\partial_t\Psi(r,t). \tag{3.31}$$

The field-free Hamiltonian H_0 is diagonal in its own basis, and thus the projection of this term into the field-free basis is trivial. The time dependent part of the Hamiltonian $H'(t)$ can be found within the field free basis as:

$$\hat{z}_{n,l,n',l'} = \langle\phi_{n,l}|\, r\cos\theta\, |\phi_{n',l'}\rangle = \int_0^{R_{\max}} R_{n,l} r R_{n',l'} dr \int Y_{l,m}\cos(\theta) Y_{l',m} d\hat{r}, \tag{3.32}$$

where $\hat{z}$ is the dipole moment operator in the field-free basis, with matrix elements given by the integrals in Equation (3.32). In practice, the spherical harmonic integrals are found from the Clebsch-Gordon coefficients using a library function [65] for more efficient calculation. Combining this information, the time dependent Schrödinger equation is given by:

$$\hat{H}(t)\mathbf{C}(t) = \left[\hat{H}_0 + E(t)\hat{z}\right]\mathbf{C}(t) = i\partial_t\mathbf{C}(t), \tag{3.33}$$

where we have defined the time dependent Hamiltonian in the field free basis as $\hat{H}(t)$.

3.2.4 Implementation of numerical basis state method

3.2.4.1 Numerov Method

We would like to solve Equation (3.28) numerically on an evenly spaced grid, with respect to x. However in this form, it is no longer an eigensystem of the form:

$$\hat{A}v(x) = \lambda v(x), \tag{3.34}$$

where $\hat{A}$ is a matrix, and λ and $v(x)$ are the eigenvalue and eigenvector respectively. Instead, Equation (3.28) is known as a generalized eigenvalue problem, which are equations of the form:

$$\hat{A}v(x) = \lambda\hat{B}v(x), \tag{3.35}$$

where $\hat{B}$ is also a matrix. Unfortunately, in our case, $\hat{B} = r^2$ is a matrix that is very poorly conditioned, with an approximate condition number of $\kappa = R_{\text{max}}^2/R_{\text{min}}^2$. Typical values of κ for our problems are 10^{18}, since the loss of precision in basic arithmetic methods is typically the log of the condition number, $\log_{10}(\kappa) = 18$. Finite-difference matrix based eigensolvers become unrealistic to apply to this formulation of the problem.

Instead, we use the Numerov method, which is an explicit, fourth order accurate, linear multistep method for solving linear second order differential equations. The Numerov method can be applied to problems of the form:

$$\partial_{xx} y(x) = f(x) y(x), \tag{3.36}$$

where $y(x)$ is the solution to the second order differential equation to be found, and $f(x)$ is the driving function. Equation (3.28) can be written in this form with:

$$f(x; E_{n,l}) = \frac{(l+\frac{1}{2})^2}{2} + r(x)^2 \left(E_{n,l} - V\left(r(x)\right)\right), \tag{3.37}$$

where it is important to note the dependence of $f(x)$ on the energy of the state $E_{n,l}$.

The Numerov method is part of a family of methods known as "shooting" methods. These methods use a backward difference to find the next value of the solution $y(x)$ from the previous two values already found. In the case of the Numerov method the next value of the solution is given by:

$$y(x_{n+1}) = \frac{y(x_n)\left(1 - \frac{5h^2}{12} f(x_n)\right) - y(x_{n-1})\left(1 + \frac{h^2}{12} f(x_{n-1})\right)}{\left(1 + \frac{5h^2}{12} f(x_{n+1})\right)}, \tag{3.38}$$

where x_n is the nth point in the continuously spaced grid between $X_{\text{min}} = \log(R_{\text{min}})$ and $X_{\text{max}} = \log(R_{\text{max}})$.

3.2.4.2 Algorithm

It is important to note that the Numerov method is not an eigenvalue solver but a differential equation solver. It attempts to find a function $y(x)$, given a function $f(x; E_{n,l})$ and two starting points. However, for an energy that is not an eigenvalue, $y(x)$ will eventually diverge. We must use this divergent behavior – and the other properties of the eigenfunctions such as continuous second derivatives for continuous potentials and adherence to the boundary conditions – to determine an algorithm that will reliably give us accurate eigenvalues and eigenfunctions.

The algorithm that we use is fundamentally a binary search. We first establish an upper bound and a lower bound to the energy of the eigenstate that we are interested in finding. We then calculate the wavefunction for the energy in the middle of this region and determine if that energy is greater or smaller than the energy of the eigenstate that we are interested in. If it is greater, we use it as a new upper bound on the energy, and look for an energy halfway between this new upper bound and the previously established lower bound. If it is lower, we similarly restrict the search space. In this way, we converge to the correct energy to whatever accuracy we desire, within the discretization error of the Numerov method.

The ability to do this binary search relies on the ability to accurately determine whether the guess for the energy of the state is high in energy or low in energy in comparison to the true energy of the state. There are two different techniques available to determine if the state is high or low in energy. However, they suffer from robustness issues depending on the energy, and how far the energy is from the correct energy for the state that we are trying to find:

- The number of nodes (zeroes) of the wavefunction. We know that solutions to the spherical time independent Schrödinger equation with quantum numbers n and l have $n - l - 1$ nodes. However, for tightly bound states, where the wavefunction approaches zero before our external boundary condition must be enforced, there is a wide range of energies that will have the correct number of nodes. For energies below the ground state of the atom we are examining, the Numerov method can also exhibit behavior where it generates spurious nodes.

- Enforcing the boundary conditions by propagating from both ends, and then determining the derivative of the wavefunction where the two propagations meet. For an eigenfunction, these two wavefunctions should meet exactly, and have a matched first and second derivative where they meet. However for an energy that is too small, the forward derivative will have a smaller second derivative than the backward propagation. For an energy that is too large, the opposite occurs.

- When the solver is very close to the correct energy, the difference in the second derivative can get smaller than machine precision, while there might be a difference between the upper bound and lower bound of the energy that is significantly larger. This necessitates the use of the first derivative to finish the calculation. For an energy that is too small, the forward first derivative will be larger than the backward first derivative.

While none of these techniques can find a state on their own, we can combine them in order to design a more robust algorithm for determining the correct eigenstate, with the correct eigenenergy. After we calculate the wavefunctions, we normalize them, and store them for later orthogonalization.

This processes is independent for each value of l that we wish to use, allowing for a simple parallelization in calculating the eigenstates for each l independently. This results in each processor working on a single l value, and solving for each n in sequence. Parallelization of the individual n eigenstates is not worth the effort due to the sequential nature of the orthogonalization that must be performed after finding each n.

3.2.4.3 Orthogonalization

Solving for basis states using the Numerov method is not exact. Small numerical inaccuracies and instabilities prevent the wavefunctions determined this way from being pure eigenstates. Furthermore, since we are not using an eigenstate solver that has an orthogonalization step, the orthogonalization must be enforced explicitly. This is important, since the dipole transition operator within the field-free Hamiltonian needs to be found from orthogonal states in order to avoid errors in the calculation.

The states that are found by our eigensolver are a mixture of the true orthogonal eigenstates

$$\widetilde{\phi}_{n,l}(r) = a_{n,l}\phi_{n,l} + \sum_{n' \neq n,l} \langle \widetilde{\phi}_{n,l} | \phi_{n',l} \rangle \, \phi_{n',l}(r). \tag{3.39}$$

Here, $\widetilde{\phi}$ represents a state from the eigensolver that still needs to be orthogonalized, ϕ represents a pure state, and $a_{n,l}$ is the fraction of $\widetilde{\phi}$ that is a pure state. For the states found by our eigensolver, $a_{n,l}$ will be close to 1.

We remove the unwanted contributions from each state using the modified Gram-Schmidt orthogonalization routine [66]. The modified Gram-Schmidt orthogonalization routine just subtracts the projection of the completed states from each new state after it is calculated. In this manner, only the components of the previously calculated pure states are left:

Algorithm 1 The Modified Gram-Schmidt algorithm

```
1: for all $n \leftarrow n_{\min} \ldots n_{\max}$ do
2:     $\mathbf{v}_n \leftarrow \widetilde{\phi}_{n,l}$
3:     for all $i \leftarrow 1 \ldots n-1$ do
4:         $\mathbf{v}_n = \mathbf{v}_n - (\mathbf{v}_i \cdot \mathbf{v}_n)\mathbf{v}_i$
5:     $\mathbf{v}_n = \mathbf{v}_n / |\mathbf{v}_n|$
```

Algorithm 1 is only concerned with a growing subset of the basis states in our basis set – the outer loop (line 1) is done concurrently with the Numerov eigensolve. Because each state is only orthogonalized against the previous states that have been calculated, we can orthogonalize a state in parallel while finding the next state via the Numerov method. This significantly reduces the calculation time.

Note that the orthogonality condition only needs to be enforced for the *radial* eigenfunctions with the same l value. States that have different l values have their orthogonality ensured by the angular part of the wavefunction.

3.2.4.4 Comparisons with previous results and literature data

Any numerical method should be compared against known results. Thankfully, the hydrogen atom is analytically solvable, and gives us a good benchmark to compare against.

The analytic solutions of the radial states of the hydrogen atom can be written down in terms of Kummer's function:

$$R_{n,l}(\rho) = N\left(-\frac{i}{\rho}\right)^{l} e^{-\rho/2} M(l+1-n, 2l+2, \rho), \tag{3.40}$$

$$\rho = \frac{2Zr}{n}, \tag{3.41}$$

where N is a normalization constant, Z is the nuclear charge, n is the principal quantum number for bound states, and $n = -iZ/k$ for continuum states with momentum k.

For the bound states, this reduces to:

$$R_{n,l}(r) = Ne^{-r/n}\left(\frac{2r}{n}\right)^{l+1} L^{2l+1}_{n-l-1}\left(\frac{2r}{n}\right), \tag{3.42}$$

where L is one of the associated Laguerre polynomials, and each state has energy $E_n = 1/(2n^2)$. The continuum states are given in terms of the Coulomb wave function ($F_l(\eta, \rho)$):

$$R_{n,l}(r) = NF_l\left(\frac{-1}{k}, kr\right), \tag{3.43}$$

which we find using a library function [67, 68]. The momentum is calculated from the dispersion relation $k = \sqrt{2E}$.

A comparison between our calculations and the results of Equations (3.42) and (3.43) has been performed. In Figure 3.4, the bound states are plotted along with the relative error between the analytic and calculated wavefunctions, while in Figure 3.5, the same has been done for the continuum. The boundary conditions change the character of the bound states with principal quantum number above roughly $n = 16$, as the exponential decay can no longer get small enough before encountering the infinite potential at the edge.

For the bound states, we can also compare the calculated energies to the analytically known energies. In Figure 3.6, the relative error is shown for the first five l eigenvalues and the first 18 n eigenvalues. The calculated eigenvalues diverge from the real eigenvalues drastically when n is greater than 16, as the boundary conditions influence the wavefunction and its energy.

We have adapted this method from a previous work by Chen et al. [69], but we improved upon the accuracy of the bound states found in [69] significantly. Table 3.2 gives a comparison

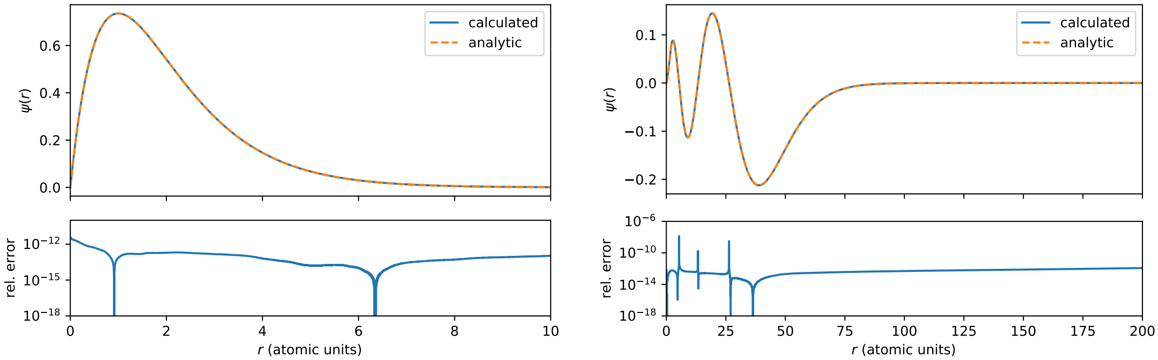

Figure 3.4: A comparison between the analytic and the calculated bound states for the ground state ($n = 1, l = 0$) on the left, and $n = 5$,$l = 1$ on the right. The relative error of $|\Psi_{\text{calc}} - \Psi_{\text{anal}}|/\Psi_{\text{anal}}$ is included underneath each plot. These were calculated with $R_{\text{max}} = 1000$, $300,000$ points per grid, and $R_{\text{min}} = 10^{-6}$. The plots only show a portion of the r range of the wavefunctions so details can be seen.

between this work and the previous work. We note that we have reached an improvement in the relative error between the analytic result and our calculated energies on the order of 10^{-3} to 10^{-4} better.

3.3 Time dependent calculations

The *ab-initio* calculation of the susceptibilities requires an *ab-initio* calculation of the time dependent wavefunction. Thus, we must propagate Equation (3.33) in time, which usually takes the vast majority of the calculation time. There are two important parts of the numerical solution of the time-dependent calculations: the propagation itself, which is done using the Crank-Nicholson method for the work presented in this thesis (see section 3.3.1) and the implementation of an absorbing boundary condition, which in this work is related to the absorption of part of the wavefunction representing high energy states.

3.3.1 Propagation calculations

Equation (3.33) can be approximated as:

$$\mathbf{C}(t + \Delta t) \approx e^{-i\hat{H}(t)\Delta t}\mathbf{C}(t) \approx \frac{1 - i\frac{\Delta t}{2}\hat{H}(t)}{1 + i\frac{\Delta t}{2}\hat{H}(t + \Delta t)}\mathbf{C}(t), \tag{3.44}$$

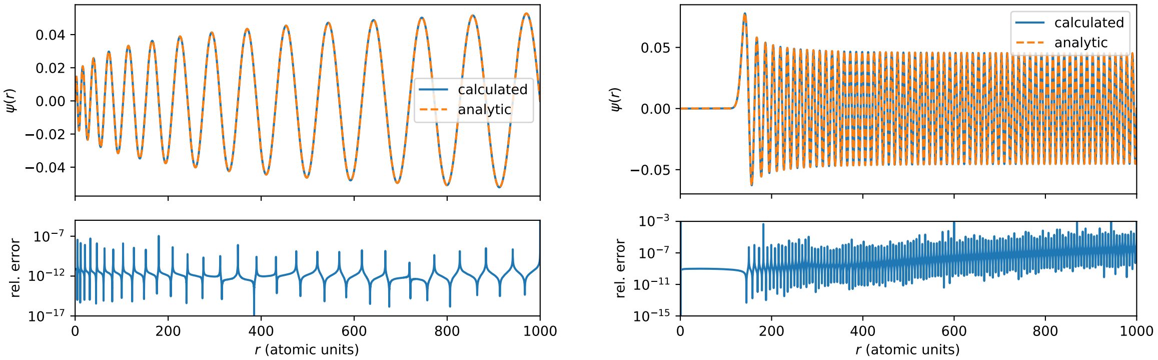

Figure 3.5: A comparison between the analytic and the calculated continuum states for the state $n = 30$,$l = 1$ on the left, and $n = 200$,$l = 70$ on the right. The relative error of $|\Psi_{\text{calc}} - \Psi_{\text{anal}}|/\Psi_{\text{anal}}$ is included underneath each plot. These were calculated with $R_{\max} = 1000$, $300,000$ points per grid, and $R_{\min} = 10^{-6}$. The momentum was found from the calculated energy of the state, rather than the quantum number. This compounds the error in the wavefunction, and results in a large error near the boundaries as the analytic wavefunction is not constrained to be zero due to the boundary conditions.

for a small timestep Δt. The second step uses the Cayley unitary transformation [70] in order to preserve the normalization of the wavefunction. The representation of the time propagation operator via the exponential function leads to the following condition: the exponent $\hat{H}(t)\Delta t$ has to be much less than 2π, in order to guarantee that we do not get aliasing effects from the propagation of the wavefunction. We satisfy this condition when $E_{n_{\max}}\Delta t < 1$. This typically results in time steps that are approximately 0.05 a.u.

This approach is known as the Crank-Nicholson method which is a unitary, energy conserving, and unconditionally stable method for propagating first order in time differential equations to second order accuracy [71]. For our system, we rewrite Equation (3.44) as:

$$\left(1 + i\tfrac{\Delta t}{2}\hat{H}(t+\Delta t)\right)\mathbf{C}(t+\Delta t) = \left(1 - i\tfrac{\Delta t}{2}\hat{H}(t)\right)\mathbf{C}(t). \tag{3.45}$$

This is an equation of the form $A\mathbf{x} = \mathbf{b}$, with $A = \left(1 + i\frac{\Delta t}{2}H(t+\Delta t)\right)$, $\mathbf{b} = \left(1 - i\frac{\Delta t}{2}H(t)\right)\mathbf{C}(t)$ and $x = \mathbf{C}(t+\Delta t)$.

The algorithms just described can be formulated in terms of repeated solutions of linear matrix equations. Due to the ubiquity of this method, a number of well designed software packages

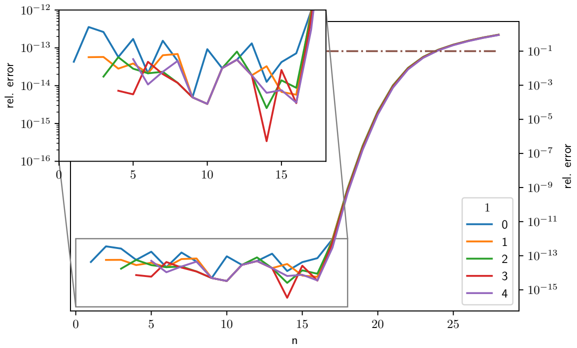

Figure 3.6: The relative error in the calculated energy eigenvalues compared to the analytical energy $E_n = 1/(2n^2)$ for $l < 5$. The right figure is a zoomed in version of the left, to better show the errors at low n. The $n > 16$ states start to be influenced by the bounding box, while $n > 23$ states have errors larger than 10%, shown by the dot-dashed brown line.

are available to help in the solution. We solve this linear system using PETSc: the Portable Extensible Toolkit for Scientific computation [72–74].

3.3.2 Absorbing boundary

Strong field ionization processes can generate very high energy electrons upon the absorption of a large number of photons. Since we need to restrict our calculation to a finite number of basis states, we can only represent states up to some maximum energy. Consequently, we need to suppress the population of even higher energy states. We solve this problem with an absorbing boundary implemented for states with either high energy (high n states) or high angular momentum (high l states). The absorbing boundary is represented by a masking function which is multiplied to the wavefunction at every time step. The masking function used in this work is a $\cos^{1/8}$ function given by:

$$a(n,l) = \cos^{1/8}\left(\frac{n-(n_{\mathrm{max}}-n_{\mathrm{abs}})}{n_{\mathrm{abs}}}\frac{\pi}{2}\right)\cos^{1/8}\left(\frac{l-(l_{\mathrm{max}}-l_{\mathrm{abs}})}{l_{\mathrm{abs}}}\frac{\pi}{(2)}\right) \tag{3.46}$$

The specific function used in the present work was found to sufficiently reduce the wavefunction inside the absorbing region and, hence, prevent reflections back to states with lower energy and/or angular momentum. In test calculations we have found that in this specific set of problems the $\cos^{1/8}$ absorber leads to a more efficient suppression of the wavefunction than other techniques

		Prev. Result		This Work	
n	E_n	$l=0$	$l=1$	$l=0$	$l=1$
1	-0.5	2.0×10^{-8}		4.3×10^{-14}	
2	-0.125	2.0×10^{-8}	0.0×10^{-10}	2.6×10^{-13}	4.6×10^{-14}
5	-0.02	8.0×10^{-9}	5.0×10^{-9}	2.1×10^{-14}	3.9×10^{-14}
10	-0.005	2.3×10^{-9}	1.9×10^{-9}	9.2×10^{-14}	3.3×10^{-15}

Table 3.2: The relative error between the analytic and calculated energies of a few different bound states from [69] and this work. We achieve significantly better (3 or 4 orders of magnitude) accuracy using our logarithmic grid.

such as complex absorbing potentials or other potentials of the form $\cos^{1/n}$. In Figure 3.7, the final wavefunctions of a 10 cycle sine-squared pulse with carrier frequency 800 nm and intensity 10^{14} W/cm^2 with and without an absorber.

3.4 Summary

In summary, the numerical basis state method is a capable process for doing *ab-initio* calculations of the time dependent Schrödinger equation. The field-free basis states that underlie both the numerical basis state method and the perturbative calculations that will be used in subsequent chapters are found using a Numerov based eigensolving algorithm, while the propagation used in the *ab-initio* is performed using the Crank-Nicolson method.

This will allow us to compare between the perturbative and non-perturbative calculations of the susceptibility, as seen in Chapter 4. Furthermore, we will use this method on its own in order to find the time dependent susceptibility in Chapter 5.

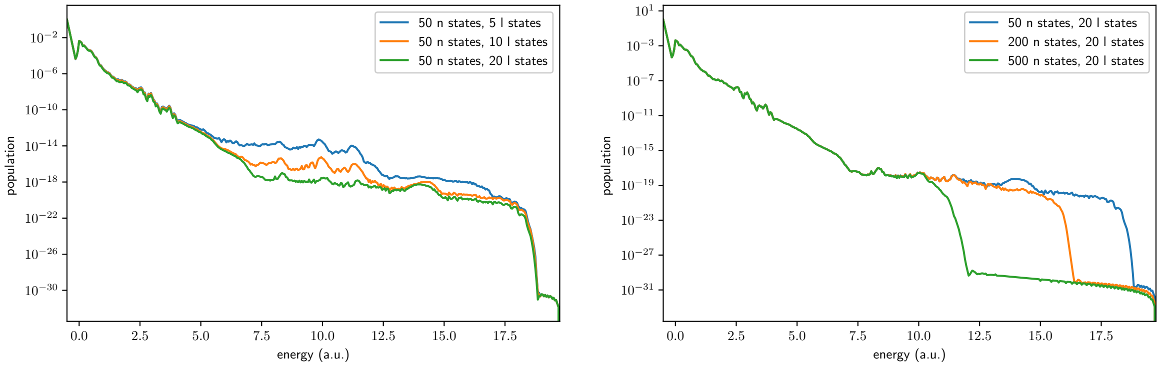

Figure 3.7: The final wavefunctions from two different calculations using a 10 cycle sine-squared pulse with carrier frequency 800 nm and intensity 10^{14} W/cm^2. Panel on the left shows three different sizes of l absorbers for an n absorber of size 50. Good convergence is achieved, with $l = 20$ giving good accuracy at lower energy levels. Panel on the right shows three different sizes of n absorbers with an l absorber of size 20. All absorbers are identical for lower energies, however the n absorber of size 50 shows some reflection at high energies.

Chapter 4

Calculations of *ab-initio* and perturbative susceptibilities

In this Chapter we apply the numerical basis state method to calculate the nonlinear perturbative susceptibilities, and compare them to *ab-initio* calculations of the susceptibilities. Through this comparison, we show that the perturbative susceptibilities we calculate fail to show converging behavior at intensities above a certain threshold. We further find that in the same intensity regime the results of perturbative calculations and the *ab-initio* calculations diverge. We examine a few different systems in order to confirm this behavior, and discuss the effect that the ionization energy has on divergence as a function of intensity using hydrogen, helium, as well as different model atoms.

We also examine the process of low-order harmonic generation by examining the third and fifth harmonics in hydrogen. By analyzing the perturbative series as a function of intensity, and the *ab-initio* calculations as well, we determine the breakdown of the perturbative approximation for low order harmonic generation.

4.1 Introduction

The nonlinear response of an atom to a strong external field, e.g. an intense laser, can give rise to a number of interesting phenomena. Low order harmonic generation, where the atom emits odd harmonics of the fundamental frequency, is generated by absorbing n photons at frequency ω and emitting a photon with frequency $n\omega$. If $n\omega$ is large enough to ionize the atom, multiphoton ionization is observed. These processes are perturbative at low intensities: the efficiency of $n\omega$

generation is proportional to E^n, where E is the electric field strength.

The response of the polarization to the electric field is given by:

$$P(\omega) = \chi(\omega)E(\omega), \tag{4.1}$$

where χ is the electric susceptibility of the material. For a perturbative process, this can be expanded in powers of the electric field as:

$$P(\omega) = \chi^{(1)}(\omega)E(\omega)+\chi^{(2)}(\omega;\omega_1,\omega_2)E(\omega_1)E(\omega_2)+\chi^{(3)}(\omega;\omega_1,\omega_2,\omega_3)E(\omega_1)E(\omega_2)E(\omega_3)+\dots \tag{4.2}$$

where $\omega = \sum_i \omega_i$. Typically, this series is truncated after the first nonzero nonlinear term $\chi^{(3)}$ ($\chi^{(2)}$ is zero for centrosymmetric media), and the term where $\omega = \omega_1 = \omega_2 = -\omega_3$ can be used to describe the physics of self-focusing.

We can see the three step process of filamentation (discussed in Chapter 1) demonstrated in the ab-initio calculations of the susceptibility of noble gases done in 2002 by Nurhuda et al. [75]. In Figure 4.1 we show the susceptibility as a function of intensity. The linear increase in the susceptibility at low intensity is self-focusing, the saturation is associated with the ionization, and the downturn is associated with plasma induced defocusing. This saturation and eventual downturn requires negative higher order contributions in the susceptibility, though Nurhuda explained the saturation and downturn as the influence of the ionized electron.

The ionization based model described in Chapter 1 was believed to be well understood [15]. However, in 2009, Loriot et al. challenged this model by extracting out higher order terms of the index of refraction [24] (see Section 2.1 for how the index of refraction is related to the susceptibility) by using a cross polarization measurement that is insensitive to the plasma contribution. The extracted terms, part of the perturbative series for the index of refraction:

$$n = n_0 + n_2 I + n_4 I^2 + n_6 I^3 + n_8 I^4 + n_{10} I^5 + \dots, \tag{4.3}$$

shown in Table 1.1 have a positive n_2, a negative n_4, a positive n_6 and a negative n_8. This challenged the idea that the saturation and downturn of the susceptibility was caused by ionization alone, and led to the Béjot et al. paper where they examined filamentation *without* ionization [25].

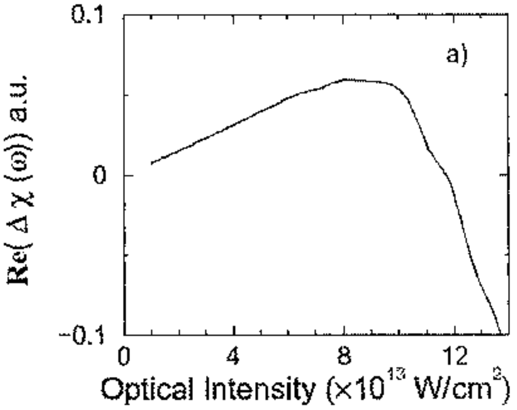

Figure 4.1: Susceptibility of the neon atom as a function of intensity. Note the linear increase as a function of intensity for low intensities, the saturation, and the eventual decrease of the suceptibility. From [75].

This possibility subsequently ignited a significant controversy in the field of filamentation, and there have been a number of papers that have attempted to either confirm or disprove the applicability of the higher order Kerr effect (HOKE) contribution to the filamentation process. It raised two related questions: Are the higher order Kerr terms an accurate way to describe the physics of filamentation? Did Loriot et al. actually extract out the *perturbative* Kerr terms? We will discuss a few of the more notable theoretical considerations of the higher order Kerr terms.

Köhler et al. used an *ab-initio* method to determine the higher order susceptibilities of the hydrogen atom [29]. They attempted to extract the susceptibilities in two different ways: by examining the nth harmonic yield as a proxy for $\chi^{(n)}$ (the harmonic susceptibilities), which can be done as a function of intensity; and by finding the individual perturbative degenerate susceptibilities from the susceptibility vs. intensity curve. For a perturbative process, the susceptibility terms should be constant with intensity by definition. However, this is not what was found. In Figure 4.2, the nonlinear susceptibilities of hydrogen are reproduced from [29]. Notice that for longer pulses, the susceptibilities are all constant, or nearly so at low intensities. This is the behavior that is expected for perturbative susceptibilities. However, as the intensity increases, the susceptibilities that are extracted are no longer independent of the intensity, implying a fundamentally non-perturbative process.

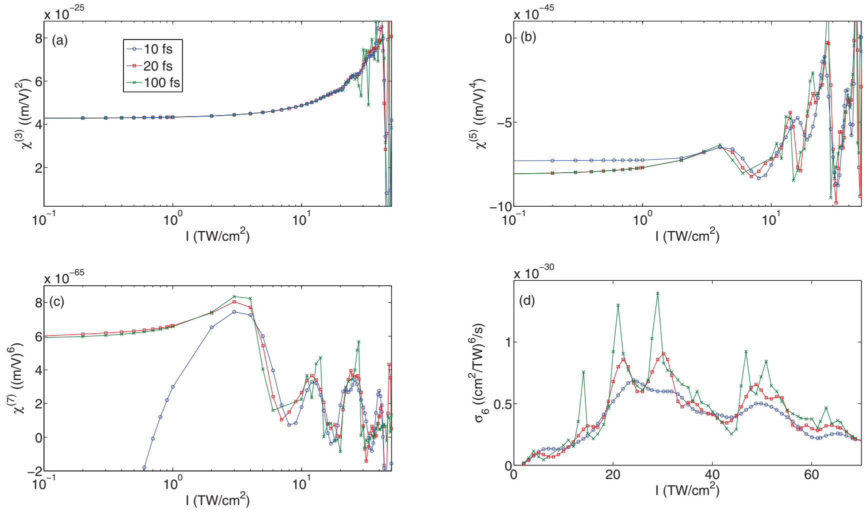

Figure 4.2: The nonlinear harmonic susceptibilities of the hydrogen atom as a function of intensity. From [29].

Bree et al. attempted to calculate the nonlinear indices in a different way [31, 32]. They first calculated the n photon ionization cross-section using a modification to the strong-field approximation, and used this as a proxy for the nth order perturbative absorption. Using the nonlinear Kramers-Kronig relationship, they found the approximate nonlinear coefficients of the index of refraction. This index of refraction qualitatively showed the same saturation and downturn of the susceptibility present in the Loriot et al. paper, however, theoretical questions about the use of a ionization cross section to find an ionization independent index of refraction lay doubts as to the validity of this result.

These theoretical and experimental studies hinted at, but failed to reach, a consensus on the applicability of the higher order susceptibility terms to the physics of high intensity pulses. We intend to determine the boundary of applicability for the perturbative susceptibility with our work, by making a comparison between perturbative and *ab-initio* calculations within the same theoretical framework.

The remainder of this Chapter is spent discussing the results of the comparison between the calculated perturbative susceptibility and the calculated *ab-initio* susceptibility (section 4.2) and an examination of the perturbative and *ab-initio* low order harmonics (section 4.4).

4.2 Electric Susceptibility

We first examine the electrical susceptibility. We would like to discuss the higher order Kerr effect, however, the index of refraction is fundamentally a macroscopic phenomena. We discussed in section 2.1 the relationship between the index of refraction and the electrical susceptibility[1]

Any discussion of the validity or accuracy of the perturbation series requires a benchmark to compare it to. Thus, our discussion of an intensity limit for the higher order perturbation terms requires a comparison between the perturbative series and *ab-initio* calculations. Furthermore, in order to reduce the relevance of various numerical approximations, we use the same basis states to calculate both the *ab-initio* and perturbative calculations.

We have discussed the calculation of the basis states necessary for both the perturbative series calculation and the *ab-initio* calculation in subsection 3.2.4. We have also previously discussed the *ab-initio* propagation in the field-free basis in subsection 3.3.1.

4.2.1 *Ab-initio* calculations

From Equation (2.12), we find the susceptibility by first determining the expectation value of the dipole moment as a function of time for an electric field polarized in the z direction:

$$\langle p(t)\rangle = -e\,\langle \Psi(t)|\,\hat{z}\,|\Psi(t)\rangle\,, \tag{4.4}$$

where $|\Psi(t)\rangle$ is the computed *ab-initio* wavefunction as a function of time, and $\hat{z}$ is the dipole moment operator given by:

$$\hat{z} = \sum_{n,l,n',l'} \langle \phi_{n,l}|\,z\,|\phi_{n',l'}\rangle\,, \tag{4.5}$$

where $|\phi_{n,l}\rangle$ is the field free energy state with principal quantum number n and angular quantum number l.

---

[1] Part of the results presented in this section are published in A. Spott et al., *Ab-initio and perturbative calculations of the electric susceptibility of atomic hydrogen*, Physical Review A **90**, 013426 (2014).

The electric field is represented as a sin squared envelope:

$$E(t) = E_0 \sin^2\left(\frac{\pi t}{T_0}\right) \sin(\omega t) \tag{4.6}$$

where E_0 is the maximum field strength, T_0 is the duration of the pulse, and ω is the central field frequency. The susceptibility is then calculated using the relation:

$$\chi(\omega) = \frac{\mathcal{F}\left[\langle\Psi(t)|\, z\, |\Psi(t)\rangle\right]}{E(\omega)} \tag{4.7}$$

Ab-initio calculations are typically done with a $n_{\max}$ of 2000, and a $l_{\max}$ of 70, which takes approximately 8 hours on 20 nodes of the Janus supercomputer. Each node has 12 cores.

4.2.2 Perturbative calculation

For the perturbative calculations, we use the eigenstates of the field-free energy basis to calculate the Nth coefficient of the perturbative power series expansion of the ground state wavefunction in the external field, as given in Chapter 2:

$$\begin{aligned} &|\psi^{(N)}(\omega_1, \ldots, \omega_N)\rangle = \\ &\sum_{j_N \neq j_0} \cdots \sum_{j_1 \neq j_0} \left[\prod_{i=1}^{N} \frac{\langle\psi_{j_i}|\, \hat{\mu} E(\omega_i) e^{-i\omega_i t}\, |\psi_{j_{i-1}}\rangle}{\omega_{j_i} - \omega_{j_0} - \sum\limits_{k=1}^{i} \omega_k}\right] |\psi_{j_N}\rangle \end{aligned} \tag{4.8}$$

where ω_{j_0} is the ground state energy, ω_k and ω_i are the participating frequencies of the electric field, j_i denotes the state in the numerical basis set, and $\hat{\mu}$ is given by Equation (4.5). The lifetimes of the excited states are neglected since all calculations performed in this study are far from resonance. The Nth-order term in the expansion of the single atom polarization in an overall $n\omega$ process can then be written:

$$\left\langle \mathbf{P}^{(N)}(n\omega) \right\rangle = \mathcal{P} \sum_{j'=0}^{N} \langle\psi^{(j')}|\, \hat{\mu}\, |\psi^{(N-j')}\rangle\,, \tag{4.9}$$

where $n = 1, 3, 5, \ldots$, $\sum_j \omega_j = n\omega$ and $\omega_j = \pm\omega$. $\mathcal{P}$ refers to the average of all permutations of the frequencies. The symmetry of the electric field with respect to positive and negative frequency components (due to the fact that the electric field is a real quantity) allows us to rewrite Equation (4.9) as:

$$\left\langle \mathbf{P}^{(N)}(n\omega) \right\rangle = \epsilon_0 \chi_{n\omega}^{(N)} \prod_{i=1}^{N} \mathbf{E}(\omega_i) \tag{4.10}$$

with $\chi_{n\omega}^{(N)}$ is the Nth-order term of the susceptibility at frequency $n\omega$ due to contributing electric field frequencies ω_i. This allows us to calculate the susceptibility for any given harmonic n, frequency ω and order N. For this section, we are concerned with situations with $n = 1$, specifically the degenerate N wave mixing term for a perturbative susceptibility of order N.

4.2.3 Results of perturbative series and *ab-initio* calculations for electric susceptibilities

Here, we first present the results of our calculations for the perturbative coefficients in the power series expansion of the electric susceptibility showing the convergence of the results with respect to the box size of the numerical grid R_0 and the basis size. We then proceed by analyzing criteria for the breakdown of the series expansion at high field strengths and identify a regime for a critical field strength. Finally, we compare the results of the perturbative calculations with those of the *ab-initio* calculations, and determine the regions of correspondence and divergence of these two methods.

4.2.3.1 Perturbative higher-order nonlinear susceptibilities

In Figure 4.3(a) we present the results of our perturbative calculations for the susceptibility coefficients of the power series for the hydrogen atom, Equation (4.2), up to $\chi^{(11)}$ as a function of the frequency of a uniform external electric field. Over the frequency regime shown the coefficients are almost constant, but the higher-order coefficients tend to increase at the largest frequencies considered in the present calculations. The increase indicates that one approaches the regime of resonant transitions. When we examine the same figure for the helium atom, Figure 4.3(b), we note that the resonant transition regime is at a higher frequency, as expected due to the larger energy gap between the ground state and first excited state in helium. Since the life times of the excited states are neglected in the present perturbative calculations, we have restricted ourselves

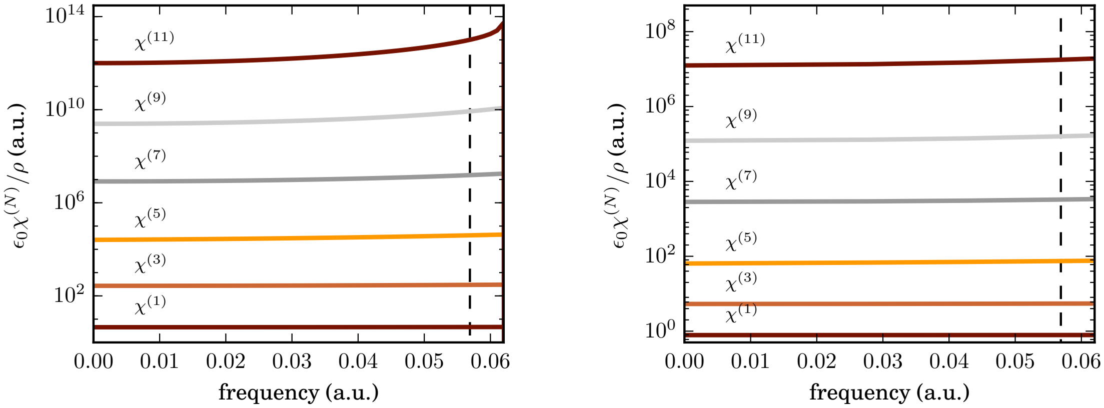

(a) (b)

Figure 4.3: a) Results of calculations for the different terms in the power series expansion for the hydrogen atom, Equation (4.2), as a function of frequency ω of a uniform electric field. b) Same for the helium atom. Note the difference in the magnitude of the susceptibilities for hydrogen and helium. The dashed line denotes 800 nm, the wavelength used for the majority of our calculations.

to calculations up to $\chi^{(11)}$ and the frequency regime below 0.06 a.u. (corresponding to wavelengths of approx. 800 nm and longer), in order to avoid the effects of the lifetimes on our calculations. We may note here already that based on the perturbative results in Figure 4.3(a) and Figure 4.3(b) it is unlikely that a negative slope in the nonlinear susceptibility, such as one seen in Loriot et al. [24], or the negative slope that Nurhuda shows in [75] can be explained via the power series expansion in the present theory, since the first five coefficients of the series are found to be positive over the frequency regime studied.

The strength of the higher order terms for the helium atom increase at a slower rate compared to hydrogen. As we increase the order, the values of the susceptibility terms for helium are much smaller than for hydrogen. For example, $\chi^{(11)}$ is approximately 10^7 a.u. for helium, while it is approximately 10^{13} a.u. for hydrogen. This can be explained by the larger energy difference between the first excited state and the ground state for helium compared to hydrogen, which leads to a weaker coupling between the states in helium.

The convergence of the results presented in Figure 4.3(a) was tested well with respect to the

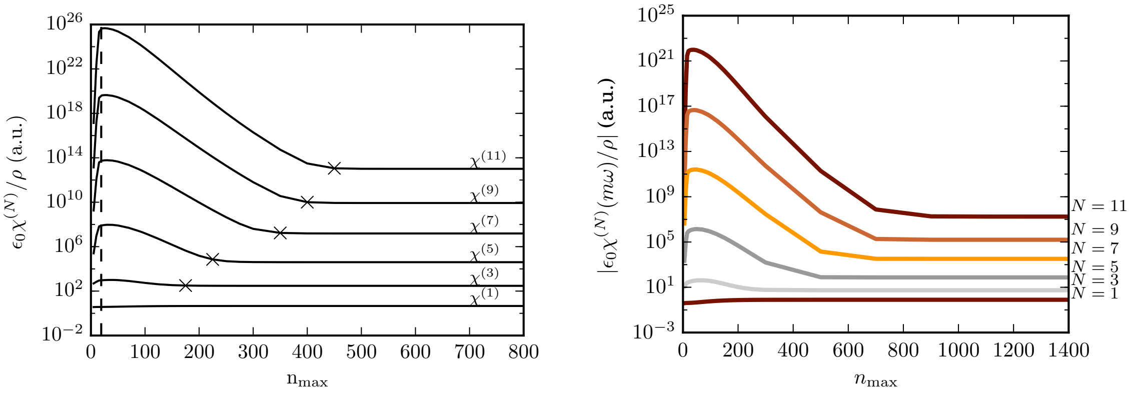

(a) (b)

Figure 4.4: a) Perturbative susceptibility coefficients $\chi^{(N)}$ in the power series expansion, Equation (4.2), as a function of the maximum principal quantum number n_{max} in the basis set for the hydrogen atom. The radial box size was $R_0 = 500$. The dashed line denotes the transition from bound to continuum sets in the present basis set, while the crosses indicate convergence of the results within 1% of the respective result at $n_{max} = 800$. b) Same as (a), but for helium.

size of the radial box R_0 and the basis size. For the present set of calculations in hydrogen we have found that a box size of $R_0 = 500$ was sufficient to reduce the error to be within 0.5%. For helium, a box size of $R_0 = 500$ was used as well. The size of the numerical basis in the present calculation is determined by the maximum angular momentum ($l_{max} = (N+1)/2$, where N is the order of the coefficient calculated), and the maximum principal quantum number (n_{max}) chosen. For a grid size of $R_0 = 500$, we varied the principal quantum number up to $n_{max} = 1400$ (corresponding to an energy of approximately 38.5 atomic units) for our perturbative calculations.

In Figure 4.4(a) we show results for $\chi^{(N)}$ as a function of n_{max} for $R_0 = 500$ at $\omega = 0.056$. One can clearly see that the results for each of the coefficients converge to a finite value for large n_{max}. The cross on each line indicates that the result is within 1% of the corresponding value at $n_{max} = 800$. As one would expect, each higher order term requires additional states to be included in the calculation in order to reach convergence. Furthermore, the dashed line at $n_{max} = 19$ indicates the separation of bound from continuum states in our basis set. For each of the nonlinear coefficients ($\chi^{(N)}$ with $N \geq 3$) we observe that the contributions from the bound states to the coefficients are positive while those from the continuum states are negative. Thus, in order to reach convergence obviously both bound and continuum states have to be included.

4.2.3.2 Breakdown of the perturbative power series expansion

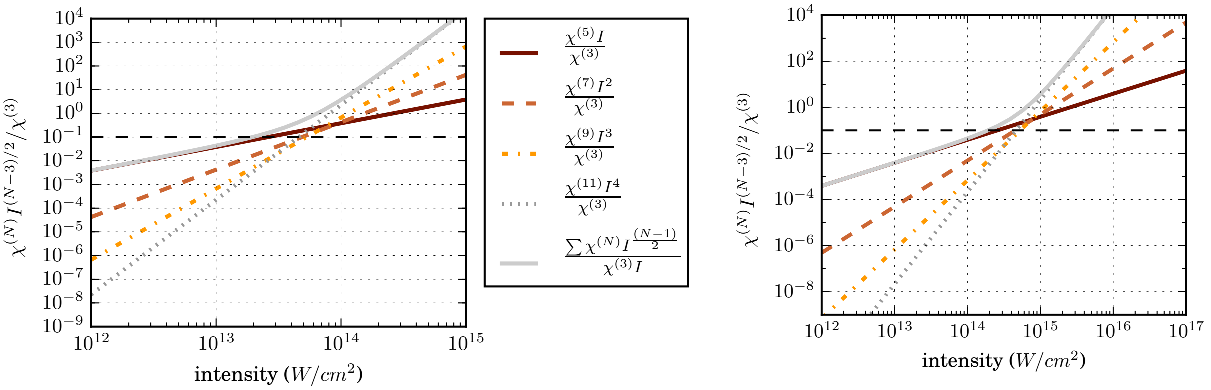

(a)

(b)

Figure 4.5: a) The perturbative nonlinear susceptibility terms $\chi^{(N)}I^{(N-1)/2}$ scaled by $\chi^{(3)}I$ as a function of the intensity of a uniform electric field at 800 nm for the hydrogen atom. b) The same for helium

In order to be applicable, the power series expansion, Equation (4.2), must converge. Since we cannot determine all the terms in the expansion, we estimate a region of applicability by investigating the relative contributions from the low order nonlinear terms in the expansion. To this end, we have determined the ratios of the higher order nonlinear terms ($N \geq 5$) to the lowest order nonlinear term, i.e. $\chi^{(N)}I^{(N-1)/2}/(\chi^{(3)}I)$ as a function of the intensity $I = |E|^2$. The results for hydrogen are shown in Figure 4.5(a) along with the sum of all higher-order terms calculated with respect to the third-order term (solid line). For low intensities ($\approx 10^{12}$ W/cm^2), each higher-order nonlinear term is much smaller than the lowest-order nonlinear term in the expansion. We therefore can expect that the power series does converge in this intensity regime. On the other hand, at high intensities ($\approx 10^{14} - 10^{15}$ W/cm^2) the trend is reversed, higher-order terms are larger in magnitude than the lowest-order term, indicating that the series may diverge. For helium, this

	N=5	N=7	N=9	N=11
$X_H = 0.01$	2.6	0.91	0.63	0.29
$X_H = 0.1$	26	9.1	6.3	2.9
$X_{He} = 0.01$	26	8.0	7.2	3.2
$X_{He} = 0.1$	260	80	73	32

Table 4.1: Intensities (in 10^{12} W/cm^2) at which the ratio $X_H = \chi^{(N)}I/\chi^{(N-2)}$ equals either 0.01 or 0.1 for hydrogen. X_{He} corresponds to the same for helium.

trend does not reverse until approximately $10^{15} - 10^{16}$ Wcm^{-2}, an order of magnitude higher than for hydrogen. This can be explained by the slow increase of the successive coefficients for hydrogen mentioned earlier.

In order to further narrow down the intensity regime at which the convergence of the power series expansion becomes questionable, we note that the ratio of the sum of all higher order terms calculated to the lowest-order nonlinear term exceeds 10% at about 3×10^{13} W/cm^2 for the hydrogen atom. From the results in Table 4.1 we further see that in this intensity regime the ratio of successive terms in the perturbative power series expansion does exceed 10%, which may be considered as another indication for the inapplicability of the series expansion. This behavior is repeated for the helium atom, but at a higher intensity. The ratio of the sum of all higher order terms calculated to the lowest-order nonlinear terms exceeds 10% at about 3×10^{14} W/cm^2 for the helium atom.

4.2.3.3 Comparison of results of perturbative and *ab-initio* calculations

Ab-initio calculations of the susceptibility are performed for laser pulses at a central wavelength of 800 nm having a sin^2-envelope and a total pulse length consisting of a finite number of electric field cycles. In order to compare our results for the power series expansion, which are determined for a uniform electric field, to those of the *ab-initio* calculations, we therefore need to account for the finite length and envelope of the pulse. To this end, we have averaged each term of the power series expansion over the intensity distribution of the pulse.

The comparison of the results of the perturbative calculations and those of the *ab-initio* calculations for a 10-cycle pulse and a 30-cycle pulse for hydrogen (Figure 4.6(a)) shows excellent agreement at low intensities. In this regime of intensities all three results increase linearly with intensity, in agreement with the expectation that the lowest-order nonlinear term is dominant at these intensities. At higher intensities however the results of the two calculations reveal an opposite trend. While the *ab-initio* results show, in good quantitative agreement with earlier predictions [75, 76], and seen in Figure 4.1, a negative slope for the susceptibility as a function of intensity, the sum of the first five terms in the power series expansion has a positive slope, as expected from the positive sign of each term in the power series determined here. The 30 cycle pulse shows a larger deviation from the perturbative calculations as the intensity increases, but starts the deviation at the same general intensity as the 10 cycle pulse. Since the saturation of the susceptibility is related to the ionization of the underlying media, we expect longer pulses to ionize more, and thus deviate more strongly from the first order nonlinear susceptibility.

The peak intensity at which the discrepancy between perturbative and *ab-initio* results equals 1% is given in Table 4.2 for different pulse lengths at 800 nm. The result is slightly larger than our

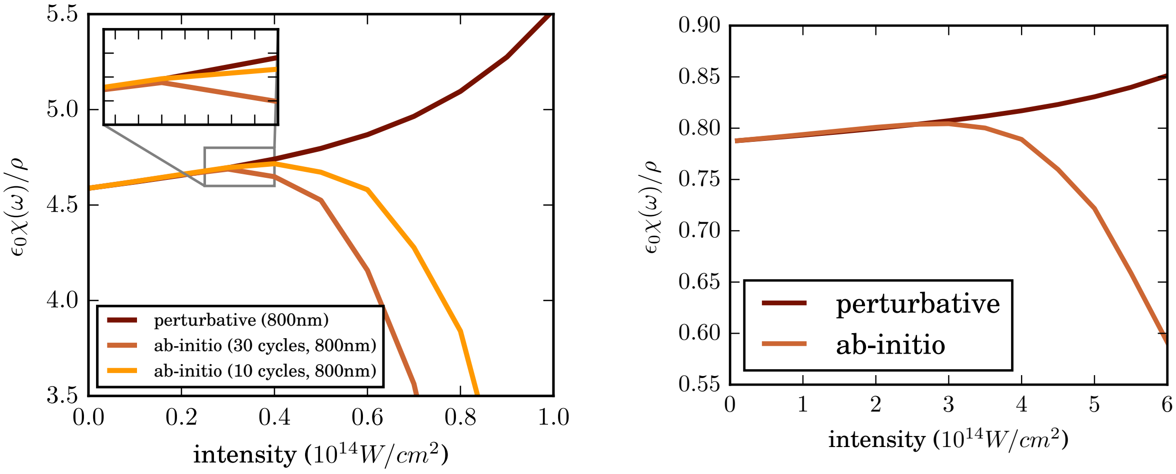

(a) (b)

Figure 4.6: a) Comparison of results of perturbative (black line) and *ab-initio* calculations for the susceptibility of hydrogen as a function of peak intensity of a 10-cycle and 30-cycle laser pulse at 800 nm. b) Comparison of results of perturbative and *ab-initio* calculations for the susceptibility of helium as a function of peak intensity of a 10-cycle laser pulse at 800 nm.

pulse length	4	10	16
peak intensity	4.7	4.2	3.9

Table 4.2: Peak intensities (in 10^{13} W/cm^2) at which the relative error between the results for the *ab-initio* susceptiblity and the perturbative susceptibility equals 1% for laser pulses of different pulse lengths (given in field cycles) at 800 nm for hydrogen.

estimates of the applicability limit of the perturbative series expansion in the previous subsection, since the latter one has been obtained for a uniform field without ionization. However, we can still conclude that the negative slope of the susceptibility is a result of the *nonperturbative* interaction between the hydrogen atom and the intense laser pulse. Thus, an explanation of this feature using higher-order expansion terms (e.g., HOKE) appears to be questionable and not applicable. This also implies that a determination of higher order terms from *ab-initio* results in the intensity regime above $2 - 4 \times 10^{13}$ W/cm^2 is meaningless. This is in agreement with the results of Köhler et al. [29], who were not able to extract consistent HOKE terms from results of *ab-initio* simulations in this intensity regime. Instead, if necessary, the atom-field dynamics has to be treated using a nonperturbative theoretical description of the polarization and susceptibility.

For helium (Figure 4.6(b)), we see the same general trend: good agreement between the results of the perturbative and *ab-initio* calculations at low intensities, and opposite trends at high intensities, however for helium the higher order terms have a visibly smaller effect on the perturbative susceptibility. The third order susceptibility term dominates the perturbative solution until past the divergence between the perturbative and *ab-initio* calculations.

The disagreement between the *ab-initio* and perturbative calculations for hydrogen and helium make clear the expected deviations for different ionization energies. We have further studied this relationship between ionization energy and onset of the breakdown of the perturbative series by using a Coulomb potential with different nucleus charges:

$$V(r) = -\frac{Z_{\text{eff}}}{r}, \tag{4.11}$$

where we may vary Z_{eff}, the nuclear charge, continuously. We show in Figure 4.7 the intensities where a divergence occurred for 1% and 10% relative error as calculated in Table 4.2. We note that

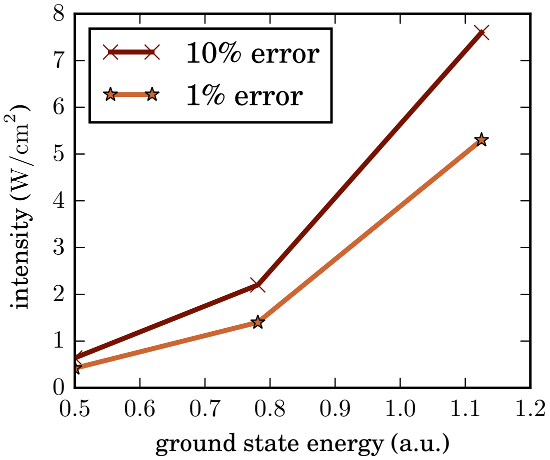

Figure 4.7: The intensity where the relative error between the perturbative and *ab-initio* calculations diverge by 1% and 10%, as a function of the ground state energy of atoms with nuclear charge 1, 1.25, and 1.5. The *ab-initio* calculations were done for a 10 cycle pulse with center frequency corresponding to 800 nm. Convergence was checked in the same manner as for previous results.

the ionization energy correlates with the breakdown of the perturbation theory as expected, given that a higher ionization energy leads to smaller perturbative terms.

4.3 Low-order harmonic generation

The comparison between the perturbative series and the nonperturbative susceptibilities let us identify an intensity regime for the breakdown of the perturbative series for hydrogen and helium. We will now analyze whether or not our conclusions regarding the applicability of perturbation theory can be confirmed by a similar study of low order harmonic generation [2] .

Kolesik et al. proposed a litmus test to determine if the higher order susceptibilities accurately describe the physics of the propagation of high intensity light through a gas [33]. They did two propagation calculations: one with higher order susceptibility terms, and one where they truncated the perturbative series after the first nonlinear susceptibility term. They then examined the third and fifth harmonic yields from both calculations. They found that the ratio of the fifth to third

---

[2] Part of the results presented in this section are published in A. Spott et al., *Transition from perturbative to nonperturbative interaction in low-order-harmonic generation*, Physical Review A **91**, 023402 (2015).

harmonic yields was roughly 0.1 for the model that included the full perturbative series, while it was significantly less than 10^{-3} for the model that truncated the series after the third harmonic term, at the saturation intensity of the susceptibility (roughly 10^{14} Wcm^{-2} for the system they were examining). They proposed that a measurement of this ratio might lead to a clear ruling on the importance of higher order susceptibilities to the propagation of high intensity light.

There have been two experiments that have attempted to discern which model is correct. The first, done by the same group that proposed the test, found that for femtosecond pulses with intensities measured in the 10s of TW/cm^2 and a central wavelength of 2.2 μm the ratio of the yields between the third and fifth harmonics was 2×10^{-4} [35]. This was consistent with models that did not have any higher order (greater than the third order) susceptibility terms, appearing to confirm their hypothesis that the higher order Kerr terms did not play a role in high intensity, short pulse propagation.

However, around the same time, another group performed similar experiments, with roughly the same intensities and pulse duration, but a 1500 nm central wavelength [34]. This experiment found that the ratio of the fifth over the third harmonic was closer to 0.1 at the saturation intensity, giving credence to the higher order susceptibilities being necessary for properly describing the propagation of high intensity laser pulses.

Using our method already developed, we believe that we can contribute to explaining the discrepancy between these two experiments, and further expand our analysis from Section 4.2.3 towards longer wavelengths.

4.4 Perturbative and *ab-initio* calculations of low order harmonics

We calculated the susceptibilities for the low order harmonics using Equations (4.9) and (4.10), this time examining the 3ω and 5ω dipole moment contributions.

In Figure 4.8 we present an example for an *ab-initio* calculation of a low-order harmonic spectrum generated at a driver wavelength of 1600 nm, a peak intensity of 5×10^{13} W/cm^2 and a pulse duration of 10 cycles. The results have been determined for a box size of $R_0 = 1000$ a.u., a

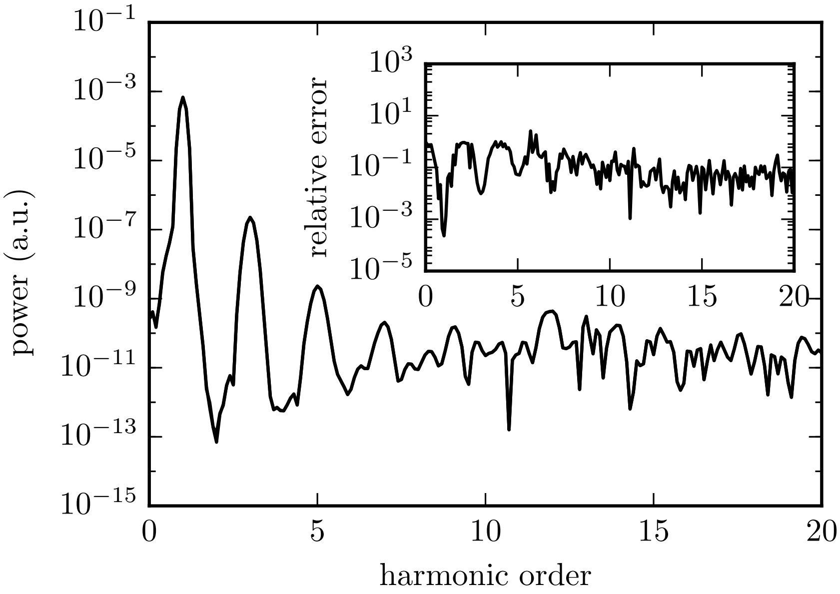

Figure 4.8: Results of *ab-initio* numerical calculations for a low-order harmonic spectrum generated by a driver laser pulse at a central wavelength of 1600 nm, a peak intensity of 5×10^{13} W/cm^2 and a pulse length of 10 cycles. The inset shows the relative error between calculations using radial box sizes of $R_{\text{max}} = 500$ and $R_{\text{max}} = 1000$.

time step of $\Delta t = 0.05$ a.u. and a maximum principal quantum number $n_{max} = 2000$ as well as $l_{max} = 70$. The convergence of the results with respect to the size of the radial box is shown by the relative error between the results for box sizes of $R_0 = 500$ and $R_0 = 1000$. Please note that the minima in the error correspond to the peaks in the harmonics.

As for the *ab-initio* calculations, we performed test calculations to ensure that the results of our calculations for the terms in the perturbation expansion of the susceptibility for low-order harmonic generation are converged with respect to the size of the box R_0 and the size of the basis set n_{max}. We note that the maximum angular momentum is determined by $l_{max} = (N+1)/2$, where N is the order of the coefficient calculated. In general, we have found that a box size of $R_0 = 500$ is sufficient for the present purpose. In Figure 4.9 we show results for $\chi^{(N)}_{n\omega}$ for $n = 1$ (dashed-dotted lines), $n = 3$ (solid lines) and $n = 5$ (dotted lines) as a function of n_{max} for $R_0 = 500$ at a laser wavelength of 1600 nm. In general, we observe that the contributions from the bound states are positive, reflected in the increase of the susceptibilities for low n_{max}, and those from the continuum

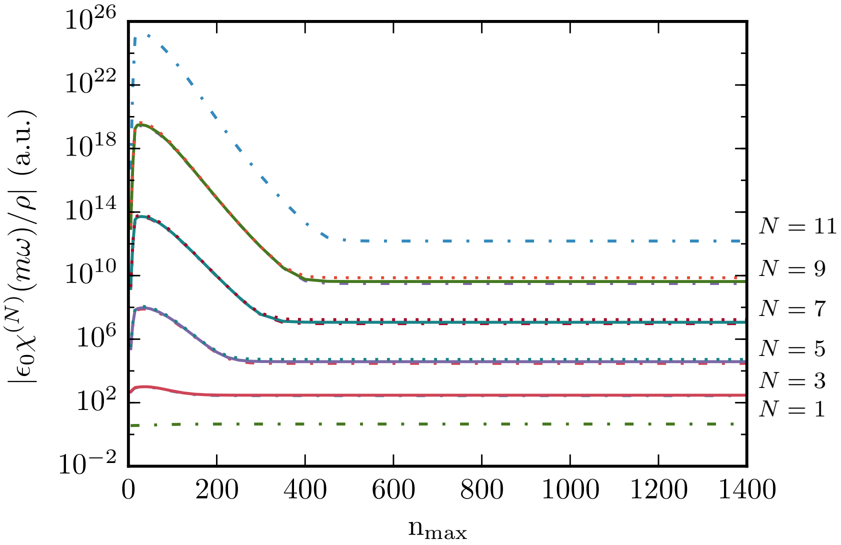

Figure 4.9: Results for perturbative power series coefficients $\chi^{(N)}_{n\omega}$ for $n = 1$ (dashed-dotted lines), $n = 3$ (solid lines) and $n = 5$ (dotted lines) as a function of n_{max}.

states are negative, corresponding to the decrease of the susceptibilities for higher n_{max}.

4.4.1 Intensity dependence of low-order harmonic generation

We have applied both calculation methods to investigate the intensity dependence of low order harmonics and the transition from perturbative to non-perturbative interaction in hydrogen. In Figure 4.10 we present the integrated power of the (a) 1st, (b) 3rd and (c) 5th harmonic as a function of peak laser intensity at a central wavelength of 1600 nm and a pulse length of 10 cycles, as obtained from our *ab-initio* calculations. For these results we have calculated the harmonic spectrum and integrated the signal for the power of the nth harmonic over the energy range $[(n-1)\omega, (n+1)\omega]$. We compare the results of our numerical calculations with the power law I^n, which is expected for a perturbative n-photon process. The predictions from the power law were matched to the numerical results at low intensities. The inset in each of the panels shows the relative error between the *ab-initio* results and the power law predictions with respect to the *ab-initio* results.

The results show that in the intensity regime between 10^{12} Wcm^{-2} and a few times 10^{13} Wcm^{-2} the *ab-initio* results start to deviate from the respective power law. This is an indication of the

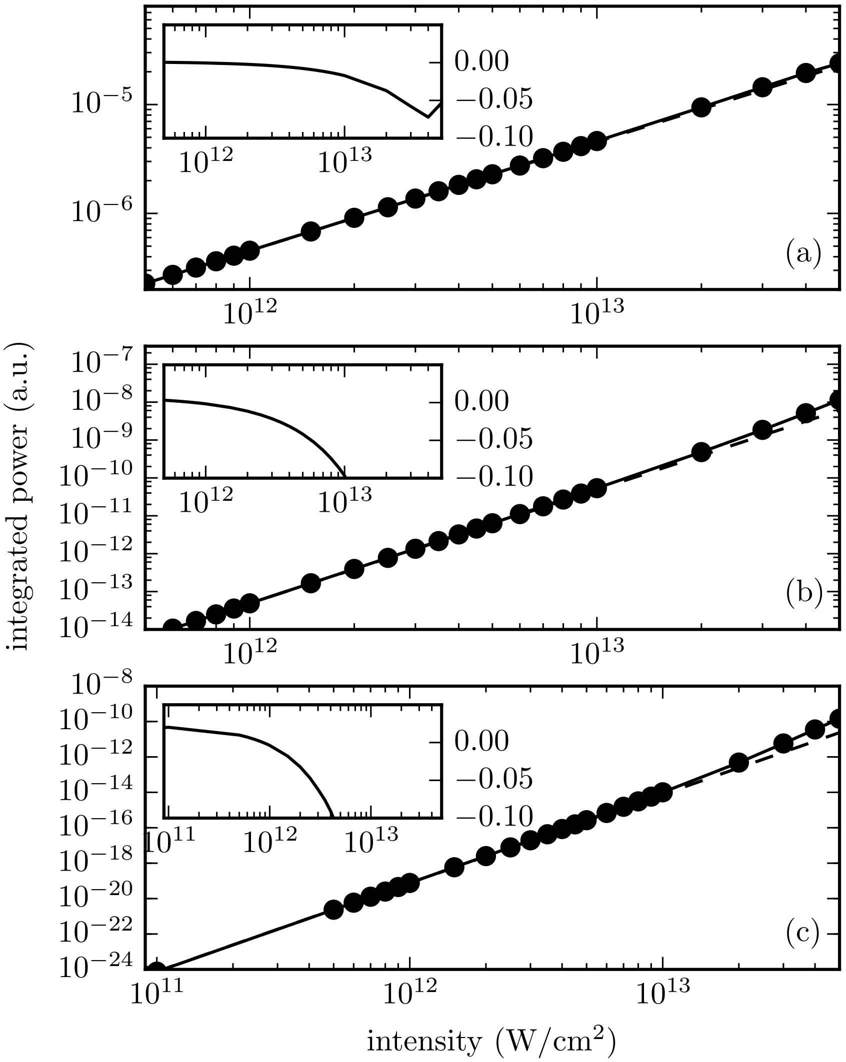

Figure 4.10: Results of *ab-initio* calculations for the integrated harmonic power (solid circles with solid lines) for the (a) 1st, (b) 3rd and (c) 5th harmonic as a function of the peak laser intensity of a laser pulse of 10 cycles at a wavelength of 1600 nm. The numerical results are compared to a perturbative I^n power law fit, which is matched to the *ab-initio* results at the lowest intensity. The insets show the relative error between *ab-initio* results and power law predictions with respect to the *ab-initio* results.

transition from a perturbative to a non-perturbative electron-field interaction. These results are in agreement with previous results that the onset of other non-perturbative phenomena, e.g., above threshold ionization [3] and high-order harmonic generation [77, 78], occurs in the same intensity regime.

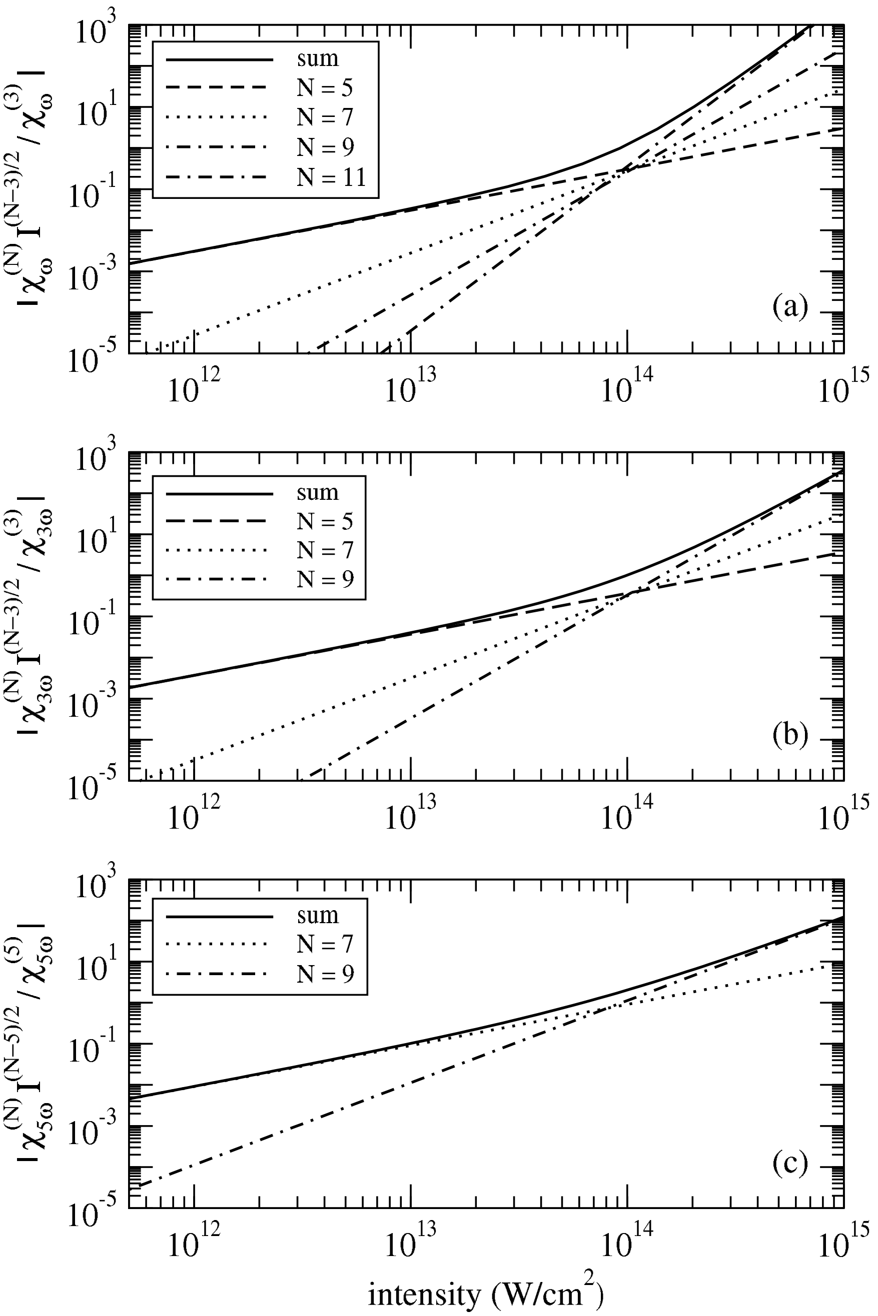

Figure 4.11: Results for the ratio of higher-order terms to the lowest-order nonlinear term in the perturbative series expansion for (a) χ_ω, (b) $\chi_{3\omega}$ and (c) $\chi_{5\omega}$. Also shown is the ratio of the sum of all higher order terms calculated with respect to the lowest-order term (solid lines).

Based on the *ab-initio* results, we expect that the perturbative power series expansion of the susceptibility corresponding to the process of low-order harmonic generation should break down in this intensity range as well. In order to test this expectation, we have calculated the first few terms in the expansion for χ_ω, $\chi_{3\omega}$ and $\chi_{5\omega}$ at 1600 nm. We study the relative contribution of higher-order terms in the expansion by presenting their ratios with respect to the lowest-order nonlinear term in Figure 4.11. Also, shown is the ratio of the sum of all higher-order terms calculated to the lowest-order term. From the results we observe the same behavior, as previously reported for the electrical susceptibility χ_ω at shorter wavelength [79], namely each higher order term is much smaller than the lowest order term, indicating the convergence of the corresponding power series expansion, at the lowest intensities studied. On the other hand, the breakdown of the series at the highest intensities is obvious as well, since the contributions of the higher order terms exceed that of the lowest order term. We further note that in each case the sum of the calculated higher-order terms reaches about 10% of the lowest-order term for intensities in the range of 1×10^{13} to 2×10^{13} W/cm^2. Therefore, this limit can be considered as an indication for the breakdown of a perturbative series expansion in strong-field processes for the hydrogen atom [23].

4.5 Summary

We have performed calculations of the susceptibility of atomic hydrogen and atomic helium using a numerical basis state method, via a perturbative power series expansion as well as the *ab-initio* results for the field induced polarization. The results of our perturbative calculations indicate a breakdown of the series expansion at intensities in the lower range of 10^{13} Wcm^{-2} for hydrogen and 10^{14} Wcm^{-2} for helium. Comparison with the *ab-initio* results shows a discrepancy in the trend in the same intensity regime. We therefore conclude that the negative slope of the susceptibility of atomic hydrogen and helium at higher intensities cannot be explained by the higher-order terms of a perturbative power series expansion. Instead, the feature has to be considered as a signature of the nonperturbative interaction between the atom and the field.

Our results for low-order harmonic generation from both *ab-initio* as well as perturbative calculations show the same onset of a transition from perturbative to non-perturbative interaction between the atom and the field as the results for the electrical susceptibility χ_ω at shorter wavelength. It is therefore not surprising that previous studies on low-order harmonic yields [26, 34, 35, 80, 81] did not help in resolving the question about the significance of higher-order Kerr effects in the filamentation of short higher-power laser pulses in gaseous media. In contrast, we conclude that any deviations from the predictions of the lowest-order perturbation theory for the polarization (and other observables) should be interpreted as a signature for the non-perturbative character of the electron-field interaction. In particular, our results also show that a quantitative analysis of strong-field below-threshold harmonic generation requires a nonperturbative theoretical approach, as e.g. introduced in [82].

While we are not able to prove a general statement about the breakdown of the perturbative susceptibility, combined with the previous results showing ATI peaks in xeon [3], and high harmonic generation [17] at similar wavelengths, we believe that a strong argument has been made for the inapplicability of perturbative descriptions of strong field processes around these intensities, and for these wavelengths.

Chapter 5

Time Dependent Susceptibility

In this Chapter, we introduce a method to calculate the time dependent susceptibility using the short time Fourier transform. First, we analyze various windowing functions for determining the short time Fourier transform and settle on the Dolph-Chebyshev family of windowing functions for our time dependent susceptibility calculations.

We then examine the time dependent susceptibility of helium at intensities near the breakdown of the perturbative susceptibility found in the previous Chapter. Using this method, we examine several features that show up at these intensities and explain them via the dynamics of the field-free bound state and continuum state contributions to the susceptibility. From there, we further study the emergence of the non-perturbative multi-photon ionization evident in the population growth and the susceptibility of helium as we increase the intensity.

5.1 Introduction

High harmonic generation (HHG) is a process for generating extreme ultraviolet (10 $\sim$ 100 eV), soft x-ray (100 $\sim$ 1000 eV) and even hard x-ray ($>$ 1 keV) coherent photons from much longer wavelength driving fields. The success in generating *bright* beams is largely a combination of microscopic and macroscopic phenomena. On the microscopic level, HHG is a process in which an electron in a single atom is driven by the external field and generates radiation of large multiples of the frequency of the driving field, as discussed in section 1.2 previously. On the macroscopic level, a coherent constructive interference of these high harmonic emissions from a large number of atoms needs to be achieved in order to generate a bright laser beam [83–85]. Ensuring that this interference is constructive instead of destructive in the direction of the propagation of the driving field is mainly done by matching the phase velocity of the driving light field with the phase velocity of the generated light. We note that geometric effect as well as other effects, such as group velocity matching [86, 87] can play a role as well, depending on the experimental setup and the wavelength of the driving field.

In general, this phase matching relationship can be written as (e.g. [88]):

$$\Delta k(t) = qk_{\omega}(t) - k_{q\omega}(t) \tag{5.1}$$

where q is the harmonic number, $k_{\omega}(t)$, and $k_{q\omega}(t)$ are the magnitudes of the wavevector of the driving field and the qth harmonic, respectively, and Δk is the phase mismatch between them. In terms of the index of refraction, this can be written as

$$\Delta p(t) = n(\omega; t) - n(q\omega; t) + \Delta g(t) \tag{5.2}$$

where $\Delta p(t)$ is the phase velocity mismatch, $n(\omega; t)$ is the index of refraction of the driving field, $n(q\omega; t)$ is the index of refraction of the qth harmonic, and $\Delta g(t)$ is a geometry induced factor for the beam parameters. In this form, there is an explicit relation between the time dependent index of refraction and the phase velocity mismatch.

Typically, the phase matching is determined by the $n(\omega; t)$ term, since the index of refraction of the higher harmonics ($n(q\omega; t)$, for large q), is well approximated by 1. Thus, the phase velocity mismatch is described in terms of the index of refraction of the fundamental field, which can be split up into two contributions (e.g. [87]):

$$n(\omega; t) \approx n_{\text{atom}}(\omega; t) + n_{\text{ion}}(\omega; t) \tag{5.3}$$

The term $n_{\text{atom}}(\omega; t)$ is the contribution from the neutral atoms or molecules. This term is typically positive, and will approach zero as the neutral atoms are ionized during the pulse, and thus the number density of neutral atoms decreases. The second term $n_{\text{ion}}(\omega; t)$ is the index of refraction due to the ionized electrons. This term is negative, and will increase in magnitude as more atoms are getting ionized. HHG is often observed in low density gas and the nonlinear terms in these calculations are typically ignored, leading to the index of refraction being approximated by:

$$n_i(\omega, t) \approx 1 + \tfrac{1}{2}\chi_i^{(1)}(\omega)\eta_i(t) \tag{5.4}$$

where i represents either the atoms or the ionized electrons, $\chi_i^{(1)}(\omega)$ is the linear susceptibility, and $\eta_i(t)$ is the time dependent density of the atoms or ionized electrons.

Recently, however, two results have challenged this conventional approximation of a linear susceptibility: the generation of extremely high harmonics from very powerful mid-infrared lasers [89], and the generation of bright harmonics in multi-ionized noble gases using powerful UV lasers [90]. In the first case, the generation of x-rays from mid-infrared lasers is improved by filamentation using very high pressure gas. From Chapter 1, we know that filamentation occurs in the regime where nonlinear effects can no longer be neglected and even not described perturbatively. We may therefore expect that a more powerful ab-initio non-perturbative method of determining the time dependent index of refraction might be useful. In the second case, the generation of bright harmonics by powerful UV laser sources requires intensities where multiple ionization occurs, which is likely beyond the saturation point of the nonlinear refractive index as a function of intensity. As we have previously shown in Chapter 4, this intensity regime marks a breakdown in the accuracy of the conventionally used perturbative series for the refractive index.

Examining the nonlinear response near the ionization threshold as a function of time is also another useful test towards further understanding the process of filamentation and the limits of perturbation theory. In investigating this question, Wahlstrand et al. [91–93] developed a technique for observing the time dependent response of a thin gas to a strong pump pulse by measuring the phase delay of a weak supercontinuum probe pulse coincident with the pump pulse. The supercontinuum probe pulse is chirped, in order to read out the phase shift as a function of time and determine a time dependent response.

The experimental results performed by Wahlstrand et al. for neon below and above the onset of ionization are presented in Figure 5.1. It shows both the transverse extent of the pump pulse,

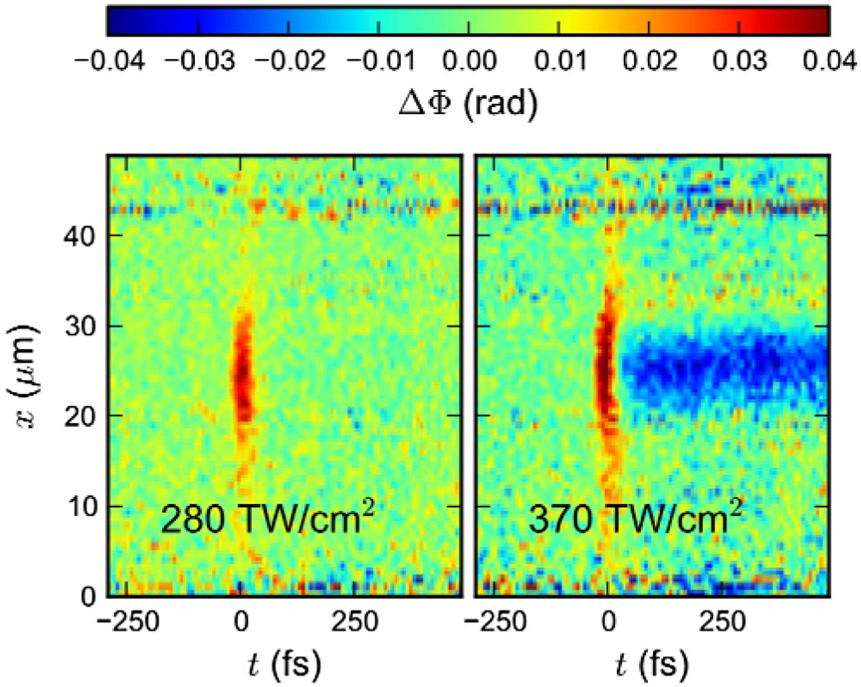

Figure 5.1: The phase shift $\Delta\Phi$ in radians as a function of time and transverse position in a gas of neon. On the left shown are results observed at an intensity below the ionization threshold, while the results on the right are at an intensity above the ionization threshold. Note the negative phase shift from the ionized electrons present on the right, after the probe pulse has ended (From [91]).

and the phase shift as a function of time. The phase shift is directly related to the shift in the index of refraction Δn due to the interaction of the pump pulse with the gas. However, the results must be carefully interpreted, as each time is also associated with a corresponding frequency in the supercontinuum signal, resulting in $\Delta n(\omega(t), t)$, with ω and t coupled.

In order to explain the experimental results, we use the theoretical ab-initio approach developed in the previous Chapters to determine a time dependent susceptibility and analyze it. In the rest of this Chapter, we will first give an overview of the method of calculating the time dependent susceptibility, and then discuss some results for the helium atom at different laser parameters.

5.2 Theoretical Method

A non-perturbative analysis of the time dependent susceptibility requires the calculation of the time dependent dipole moment beyond the conventional approach of perturbation theory. Thus we use our *ab-initio* method described in Chapter 3 to determine the dipole moment. As a brief reminder, we find the time dependent dipole moment as the expectation value of the dipole operator $\hat{\mu}$ with respect to the time dependent wavefunction $|\Psi(t)\rangle$ as:

$$\mu(t) = \langle\Psi(t)|\,\hat{\mu}\,|\Psi(t)\rangle \tag{5.5}$$

where the dipole operator is defined as:

$$\hat{\mu} = -\sum_{n,l,n',l'} |\psi_{n,l}\rangle\,\langle\psi_{n,l}|z|\psi_{n',l'}\rangle\,\langle\psi_{n',l'}|\,, \tag{5.6}$$

and $|\psi_{n,l}\rangle = R_{n,l}(r)Y_l(\hat{r})$ are the eigenstates of the field-free Hamiltonian. The wavefunction $|\Psi(t)\rangle$ is the solution to the time dependent Schrödinger equation with Hamiltonian:

$$H = H_0 + \hat{\mu}E(t)H_0 = \frac{\nabla^2}{2} + V(r). \tag{5.7}$$

Here, we assume that $V(r)$ is a spherically symmetric, single active electron potential, and H_0 is the field-free Hamiltonian.

5.2.1 Time dependent susceptibility

The time independent susceptibility is given by:

$$\chi(\omega) = \frac{\mathcal{F}\left\{\mu(t)\right\}(\omega)}{\mathcal{F}\left\{E(t)\right\}(\omega)} \tag{5.8}$$

where $\mathcal{F}\left\{x(t)\right\}$ is the Fourier transform of $x(t)$. If one multiplies the dipole moment $\mu(t)$ and the electric field $E(t)$ by a windowing function before taking the Fourier Transform, one obtains a time dependent susceptibility:

$$\chi(\omega;\tau) = \frac{\mathcal{F}\left\{\mu(t)w(t-\tau)\right\}(\omega)}{\mathcal{F}\left\{E(t)w(t-\tau)\right\}(\omega)}, \tag{5.9}$$

where the time τ (corresponding to the center of the windowing function) is now a parameter to the susceptibility, and $w(t)$ is a windowing function with limited support, i.e. it is only non-zero over some finite range $[-T/2, T/2]$.

The windowing of the Fourier transform is known as the short time Fourier transform [94]. By limiting the non-zero part of the time domain function one defines a time associated with the Fourier transform. By moving the center of the windowing function, one gets a Fourier transform for each point in time. When one applies this concept to the susceptibility, one obtains the time dependent susceptibility given in Equation (5.9). As the properties of the short time Fourier transform depend strongly on the windowing function that is being used, we will first discuss some of the properties of the windowing function, before presenting the results for the time dependent susceptibility.

5.2.2 Windowing functions

The properties of the windowing function are important to get an accurate time dependent susceptibility. A windowing function that is too wide in frequency will not allow us to separate out the driving frequency behavior from the harmonics (primarily the third and fifth), or the low frequency drift of ionized wavepackets. On the other hand, one that is too wide in time will not give the necessary time resolution and will effectively smooth out the short time behavior.

A windowing function $w(t-t')$ is any function that is non-zero only for some limited width in time, and is symmetric about some center time $t-t' = 0$. The simplest windowing function is known as the boxcar or rectangular window [95]. This function is 1 everywhere within the window size. Applying it to a function $f(t)$ is equivalent to just taking the Fourier transform of the overlapped $w(t-t')f(t)$.

The boxcar window, however, is a very poor window for many applications. The sharp cutoff at the edges of the boxcar window creates large sidelobes when taking the Fourier transform. The Fourier transform of such a square pulse is the sinc function ($= \sin(\omega)/\omega$), which results in a $1/\omega$ falloff of the sidelobes. This can be seen in Figure 5.2, which shows the amplitude of the discrete Fourier transform on a log scale. One can clearly see the sidelobes besides the central peak and

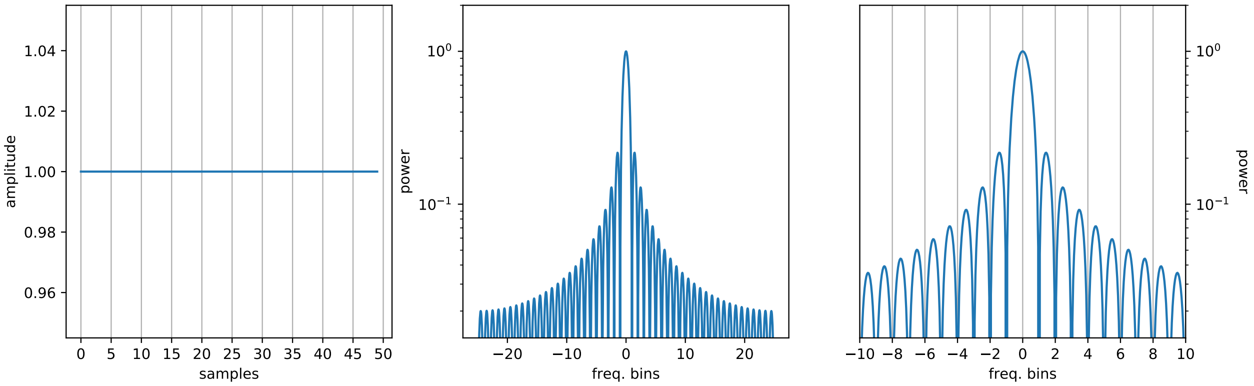

Figure 5.2: The boxcar windowing function (a) in the time domain, (b) the frequency domain (log scale), and (c) a close up view of the frequency domain (log scale) with the harmonic orders denoted for a single cycle window. Note that the attenuation for the first sidelobe is very poor (less than 10db)

their considerable height. The x-axis is presented in units of the discrete Fourier transform (DFT) bins – the smallest frequency difference that is representable by a DFT of the same size as the window.

Since multiplying a function $f(t)$ by a windowing function in the time domain is equivalent to taking the convolution of the windowing function and $\hat{f}(\omega)$ in the Fourier domain, the above example shows that the frequency response of the windowing function is important for understanding the behavior of the window function on the signal. There are a couple of criteria that are important when choosing a windowing function. For our purpose, we wish to optimize with respect to the following features:

(1) Small influence of the contributions from odd harmonics of the driving frequency. The 3rd (and 5th) harmonic should not affect the calculated susceptibility at the driving frequency, thus the sidelobes at these frequencies should be suppressed.

(2) Small interference between the contributions from the driving frequency and the very low frequency part of the dipole moment. During strong-field interactions, an electron wavepacket that is ionized will begin to drift with a velocity that is proportional to the vector potential at the time of ionization. This will show up as a component at a very low

frequency to the susceptibility which should not have an effect on the calculated results at the driving frequency in the calculations.

(3) Small window size in time, in order to examine the processes with good time resolution.

The sidelobe attenuation defines the effect that the higher order harmonics and the DC component of the field will have on the signal. If the sidelobes of the windowing function are not suppressed enough, then there will be some contribution overlapping with the time dependent susceptibility at the frequency of interest. The central peak bandwidth is also important for controlling how much of the signal from other frequencies effects the result at the central frequency. If the bandwidth is too large, then the calculated signal at the primary frequency will include contributions from the DC or even third harmonic components. These properties must be taken into account in order to optimize the result with respect to the first and second points above. The central bandwidth of any windowing function – as well as the sidelobe suppression in many cases – is inversely proportional to the size of the windowing function in time. This means that one must balance a narrow central peak with high sidelobe suppression in order to avoid the influence of unwanted signals from other frequency components, with a large central bandwidth in order to have better time resolution.

There are a few windowing functions that have the required behavior, which will be discussed below. The central peak of a window in the "flattop" family of windowing functions is very flat, giving it its name. Windows in this family are typically cosine windows (windows defined as a sum of scaled cosines), and are optimized such that the derivative in the frequency domain at $\omega = 0$ is zero. This property is valuable when the sampling time and the periodicity of the signal are not well aligned since the frequency of interest will be captured even though it is not well matched with the frequency bins.

A flattop windowing function from [95] that has been simultaneously optimized for large sidelobe attenuation and a flat top is shown in the time and frequency domains in Figure 5.3. This window is called a 5th order window, consisting of five cosine terms, and as such the first sidelobe

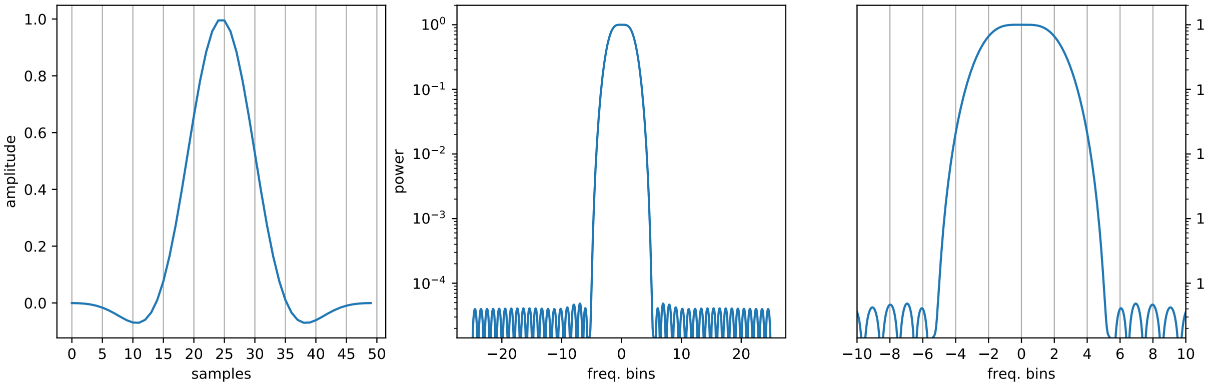

Figure 5.3: Flattop window given in Equation 5.10, in the time domain (a), the frequency domain (b), and with a closeup of the frequency domain (c). Note that the wide central peak covers 5 frequency bins.

will be the 5th frequency bin from the center. This flattop window is given approximately by [95]:

$$w(n) = 0.216 - 0.417\cos\left(\frac{2\pi n}{N-1}\right) + 0.277\cos\left(\frac{4\pi n}{N-1}\right) - 0.084\cos\left(\frac{6\pi n}{N-1}\right) + 0.007\cos\left(\frac{8\pi n}{N-1}\right), \tag{5.10}$$

where N is the total size of the window in samples and n is the number of the current point in samples.

A window which has been optimized for the highest attenuation in the first sidelobe (the sidelobe nearest to the center peak) provides another interesting option. The Hamming window [96] is a second order window with such a property,

$$w_{\text{Hamming}}(n) = 0.54 - 0.46\cos\left(\frac{2\pi n}{N-1}\right), \tag{5.11}$$

while the Blackman-Harris window [96] is a third order window of this kind

$$w_{\text{Blackman-Harris}}(n) = 0.359 - 0.488\cos\left(\frac{2\pi n}{N-1}\right) + 0.141\cos\left(\frac{4\pi n}{N-1}\right) - 0.012\cos\left(\frac{6\pi n}{N-1}\right). \tag{5.12}$$

The first sidelobe of the Hamming window has an attenuation of roughly a factor of 43db, while the Blackhman-Harris window has an attenuation of roughly a factor of 65db.

Finally, the Dolph-Chebyshev window [97], shown in Figure 5.4, is a window that is optimized to have the narrowest central bandwidth for a given constant attenuation in the sidelobes. The

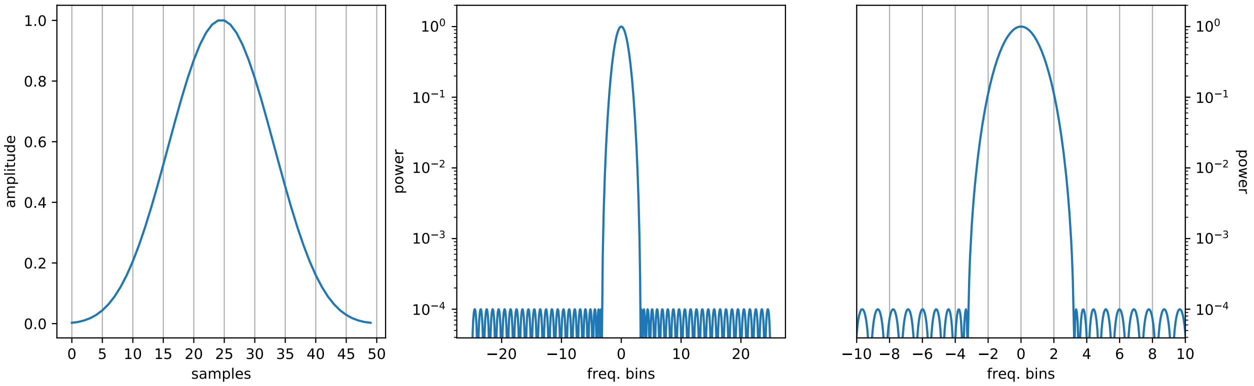

Figure 5.4: The Dolph-Chebyshev window with an attenuation set to 80db in the (a) time, (b) frequency and (c) a closeup of the frequency domain

Dolph-Chebyshev window is defined in the Fourier domain, rather than the time domain:

$$\mathcal{F}\left\{w(n)\right\}(k) = \frac{\cos\left(N\cos^{-1}[\beta\cos\left(\frac{\pi k}{N}\right)]\right)}{\cosh\left[N\cosh^{-1}(\beta)\right]} \tag{5.13}$$

$$\beta = \cosh\left[\frac{1}{N}\cosh^{-1}\left(10^{\frac{A}{20}}\right)\right], \tag{5.14}$$

where A is the attenuation in decibels, and k is the frequency component.

None of these windows have a central lobe that has a full width of less than four frequency bins. This necessitates our window encompassing more than one period of our target frequency, in order to avoid leaking from the DC component. In the rest of this Chapter we use the Dolph-Chebyshev window with a width of three periods of the frequency of interest. Our test calculations have shown that it is a good compromise between attenuation of components that we are not interested in, and a reasonably good time resolution.

5.2.3 Segmentation of time dependent susceptibility

Our use of a basis state method makes any observables accessible for separation in contributions from the eigenstates of the field-free Hamiltonian. Thus, we can split the time dependent susceptibility into contributions arising from bound and continuum states in order to better understand the influence of these states on the total susceptibility. As pointed out before, in our method the wavefunction in the energy basis is a coherent superposition of the field-free energy states:

$$|\Psi(t)\rangle = \sum_{n,l} c_{n,l,E}(t) \, |\phi_{n,l,E}\rangle \, , \tag{5.15}$$

where the eigenstates $|\phi_{n,l,E}\rangle$ are labeled by energy E as well as the principal quantum number n and the angular quantum number l. Thus, by selectively setting $c_{n,l,E}$ to zero for some choice of n, l and E, we can select the wavefunction to find a partial dipole moment.

We examine the wavefunction in two principle regions of the field-free spectrum: the bound states consisting of all states with energy less than zero, and the continuum states consisting of all states with energy greater than zero. This split then gives us three terms in the dipole moment:

$$\begin{aligned} \langle\Psi(t)|\,\hat{\mu}\,|\Psi(t)\rangle &= \overbrace{\langle\Psi(t)|\,P_{\mathrm{b}}^{\dagger}\hat{\mu}P_{\mathrm{b}}\,|\Psi(t)\rangle}^{\text{bound-bound}} + \overbrace{\langle\Psi(t)|\,P_{\mathrm{c}}^{\dagger}\hat{\mu}P_{\mathrm{c}}\,|\Psi(t)\rangle}^{\text{continuum-continuum}} \\ &+ \overbrace{\left[\langle\psi(t)|\,P_{\mathrm{b}}^{\dagger}\hat{\mu}P_{\mathrm{c}}\,|\psi(t)\rangle + \text{c.c.}\right]}^{\text{bound-continuum}} \end{aligned} \tag{5.16}$$

where P_{b} is the projection operator onto the bound states which sets $c_{n,l,E} = 0$ for $E > 0$, and P_{c} is the projection operator onto the continuum states. These three terms – referred to as bound-bound, bound-continuum and continuum-continuum contributions to the susceptibility – will be discussed in the remainder of the Chapter.

5.3 Results

We have used the Short time Fourier transform to calculate the time dependent susceptibility of Helium at five different intensities: 100, 150, 200, 250, and 300 TWcm^{-2}. These calculations were performed for a 10 cycle full width at half max pulse at 800 nm. The results for the middle 16 cycles are shown in Figure 5.5, with a vertical dot-dashed line denoting the center of the electric field of the pulse. We denoted the central cycle of the field by "0." For the low intensities (100, 150 and 200 TWcm^{-2}), the susceptibilities adiabatically follow the envelope of the field intensity. Above 200 TWcm^{-2}, however, the results deviates from this adiabatic behavior. At 250 TWcm^{-2} the peak of the susceptibility shifts towards the beginning of the pulse, and at 300 TWcm^{-2} it has

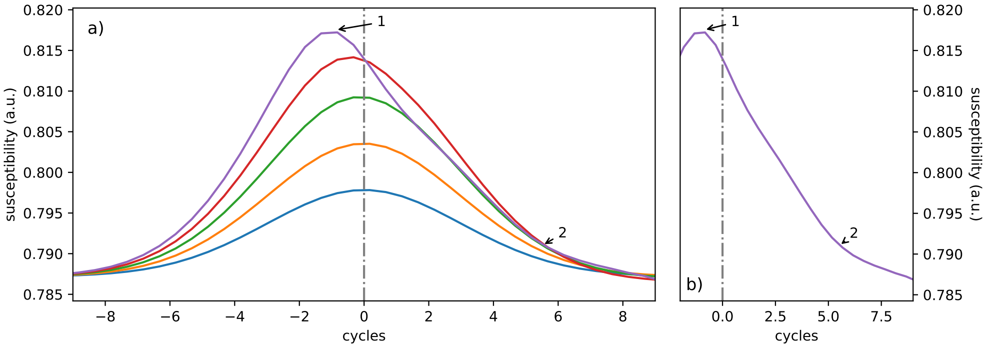

Figure 5.5: (a) The time dependent susceptibility of helium for Gaussian pulses with a wavelength of 800 nm and a full-width at half-maximum of 10 cycles at different intensities (100 TWcm^{-2} (purple), 150 TWcm^{-2} (red), 200 TWcm^{-2} (green), 250 TWcm^{-2} (orange), and 300 TWcm^{-2} (blue)). The center of the driving electric field pulse is denoted with a vertical dot-dashed line, and time is denoted in cycles of the driving field. The arrows point out the shifted peak in the susceptibility (1) and the "kink" (2) at highest intensities. Note that both the 250 TWcm^{-2} pulse and the 300 TWcm^{-2} pulse peak before the driving field. (b) A detailed plot for 300 TWcm^{-2}.

moved by more than a full cycle of the driving field. This behavior is in qualitative agreement with results presented in the supplemental materials of [91]. However, we note that it is even more obvious in the experimental results for krypton and xenon than for helium. After the peak in the susceptibility, the slope in the trailing edge for the 300 TWcm^{-2} pulse also deviates from adiabatic behavior, exhibiting two regions over which the susceptibility follows an approximately linear dependence on time: from -1 cycles to +5 cycles, and from +5 cycles on. This creates a "kink" at +5 cycles where the slope of the susceptibility changes from the strongly negative slope between -1 and +5 cycles to the less negative slope after +5 cycles. In the rest of this section we focus on the origin of these high intensity features – the "kink" and the shift of the peak of the pulse – within the context of our energy basis calculations. In particular, we analyze the field free bound and continuum state contributions to the susceptibility as a function of time.

5.3.1 Bound-bound contributions

The bound-bound contribution to the time dependent susceptibility (see Equation (5.16)) is shown in Figure 5.6(b), accompanied by the excited state population taken at the zeros of the

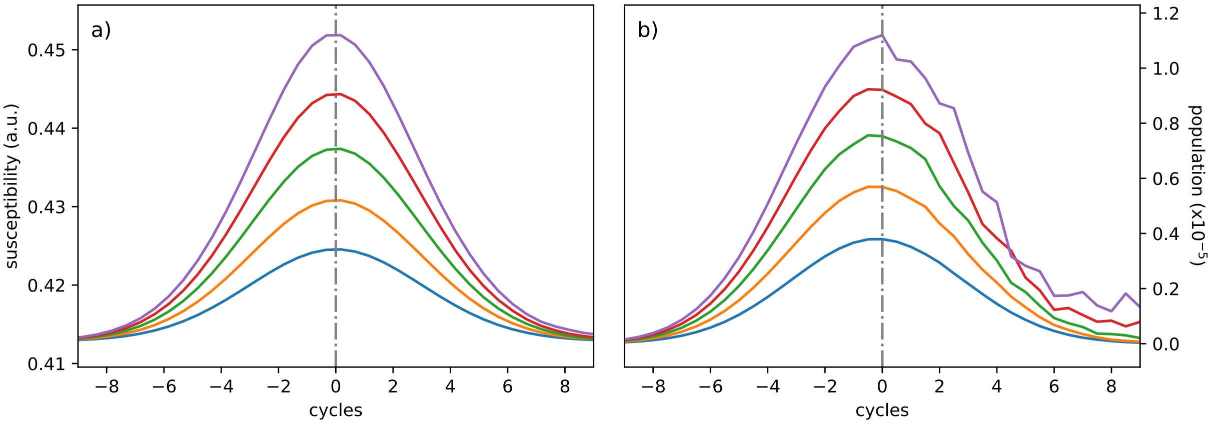

Figure 5.6: a) Bound-bound contribution to the time dependent susceptibility, $(\langle P_{\mathrm{b}}^{\dagger}\hat{\mu}P_{\mathrm{b}}\rangle\,(t))$. It follows the intensity envelope of the field for all intensities over the majority of the pulse. We note a small deviation at the end of the pulse for $300\,\mathrm{TWcm}^{-2}$ where the residual population in the excited states results in a higher value of the susceptibility at the end of the pulse as compared to the beginning of the pulse. (b) Population of the excited states taken at the zeros of the driving field. Note the non-adiabatic contribution to the population for driving fields stronger than $150\,\mathrm{TWcm}^{-2}$, along with the residual population at the end of the pulse for $300\,\mathrm{TWcm}^{-2}$. For both panels: $100\,\mathrm{TWcm}^{-2}$ (purple), $150\,\mathrm{TWcm}^{-2}$ (red), $200\,\mathrm{TWcm}^{-2}$ (green), $250\,\mathrm{TWcm}^{-2}$ (orange), and $300\,\mathrm{TWcm}^{-2}$ (blue) pulses.

driving electric field (Figure 5.6(a)). The excited states are here defined as field free states with energy less than zero, excluding the ground state. For the lowest intensity ($100\,\mathrm{TWcm}^{-2}$ purple curve), the population and the susceptibility adiabatically follow the envelope of the intensity, as expected. For higher intensities, the population does not follow the electric field intensity smoothly. Instead, the population consists of a dominant contribution driven by the perturbative interaction, where the first order and third order terms of the susceptibility dominate, and a much smaller non-perturbative part, due to the population in excited states with larger l which are populated in the trailing part of the pulse via transitions back from the continuum. We will further analyze this non-perturbative behavior in subsection 5.3.4. For the highest intensity considered ($300\,\mathrm{TWcm}^{-2}$), the residual population in the high l states results in a bound-bound contribution to the susceptibility at the end of the pulse that is slightly larger than at the beginning of the pulse.

The susceptibility from the bound states is the largest contribution to the total susceptibility.

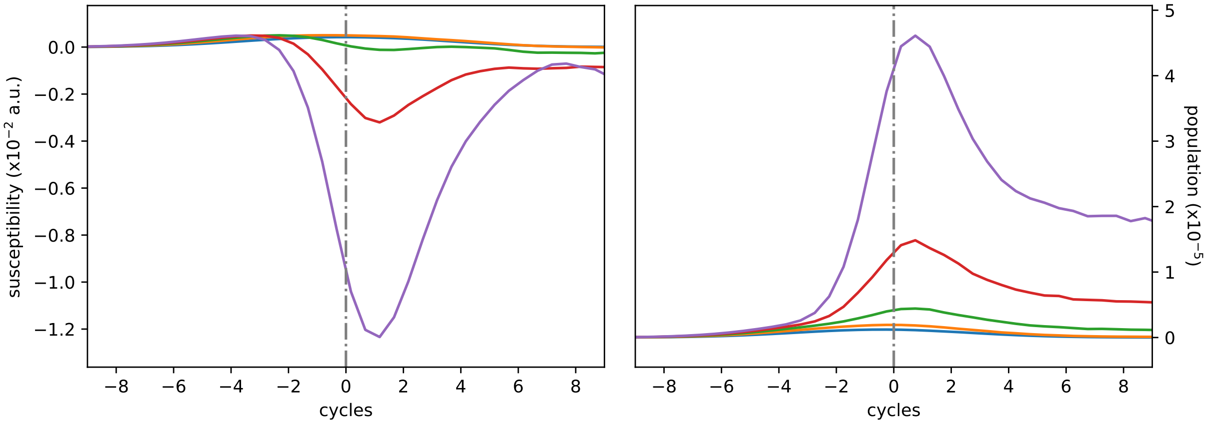

Figure 5.7: (a) Continuum-continuum contribution to the time dependent susceptibility $(\langle P_{\mathrm{c}}^{\dagger} \hat{\mu} P_{\mathrm{c}} \rangle (t))$. This contribution to the susceptibility is negative at high intensities (200 TWcm^{-2} and above). (b) The population of the continuum states taken at the zeroes of the driving field. Note the exponential growth for 300 TWcm^{-2}, which starts slightly before the center of the pulse and peaks slightly after. This is followed by a decline to a residual population at the end of the pulse. For both panels: 100 TWcm^{-2} (purple), 150 TWcm^{-2} (red), 200 TWcm^{-2} (green), 250 TWcm^{-2} (orange), and 300 TWcm^{-2} (blue) pulses.

It is therefore the reason that the overall shape of the susceptibility follows (almost adiabatically) the envelope of the intensity. Indeed at low intensities, this contribution to the susceptibility almost entirely defines the shape of the total susceptibility. For the deviations from field-following behavior, specifically the features we pointed out earlier at higher intensities, we will now analyze the other contributions in Equation (5.16).

5.3.2 Continuum state contributions

The continuum-continuum contribution to the time dependent susceptibility is shown in Figure 5.7(a), accompanied by the population in the continuum states (with energy greater than zero) taken at the zeros of the driving electric field (Figure 5.7(b)). At the lowest intensities, the shape of the susceptibility as a function of time is again adiabatic, and positive, though small. At these intensities, there is no residual population in the continuum at the end of the pulse and the population in the continuum is mainly transient and likely via perturbative interactions. This agrees with our observation that the population in the continuum states exponentially decreases with increasing energy. We show this in Figure 5.8, where the population is shown as a function of the energy at the zero of the field at cycle +1. We also note that the population in these states exhibits the same qualitative behavior as that in the excited states just below the threshold; namely an exponential decrease in the population with increasing energy, and a positive contribution to the susceptibility, as expected from perturbation theory [79]

In contrast, at the highest intensities (250 and 300 $\mathrm{TWcm^{-2}}$), the continuum is strongly (non-perturbatively) populated between -2 and +1 cycles before relaxing back to a residual continuum population at the end of the pulse. The exponential growth in population over a few cycles is a clear indication of the deviation from the perturbative regime and correspondingly leads to similar characteristic changes in the susceptibility as a function of time. Figure 5.8 shows that the population is almost equally distributed among the low energy continuum states, another strong indication of a deviation from a perturbative interaction between the field and helium atom. We note that this result agrees with our previous results in Chapter 4, where we have observed the transition

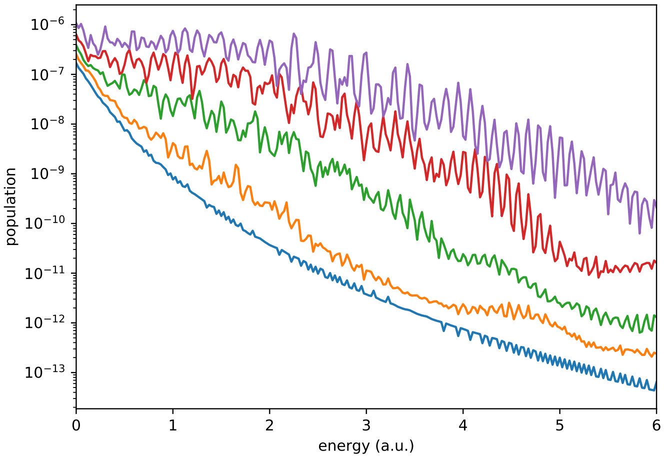

Figure 5.8: The population in the continuum states as a function of energy at cycle 1 for 100 $\mathrm{TWcm^{-2}}$ (purple), 150 $\mathrm{TWcm^{-2}}$ (red), 200 $\mathrm{TWcm^{-2}}$ (green), 250 $\mathrm{TWcm^{-2}}$ (orange), and 300 $\mathrm{TWcm^{-2}}$ (blue) pulses. Note the exponential decrease in population for the 100 $\mathrm{TWcm^{-2}}$ pulse, while at the higher intensity pulses the distribution extends to higher energies.

from the perturbative to the non-perturbative regime at similar intensities. The population in the continuum from the multiphoton transitions to the continuum causes a negative contribution to the susceptibility, in contrast to the signatures seen at low intensities. We also note that the dip in the continuum-continuum contribution to the susceptibility at +7 cycles (Figure 5.7(a)) is matched by the peak in the continuum population at +7 cycles in (Figure 5.7(b)).

These features in the contribution from the continuum states at the highest intensities can explain the signatures we pointed out in the total susceptibility (Figure 5.5). The strong growth in the continuum population (and corresponding negative contribution from the continuum contributions to the susceptibility) shows up in the total susceptibility as a shift in the peak of the susceptibility towards earlier times in the pulse. The peak in the population at around +1 cycles (and the corresponding minimum in the susceptibility) results in the linear regime between -1 and +5 cycles until the "kink" in the total susceptibility when the trapped population in the bound states contributes significantly enough to the total susceptibility to cancel out part of the negative contribution from the continuum states at approximately +5 cycles.

5.3.3 Cross term contributions

The contributions to the susceptibility from the cross terms ($\langle\Psi(t)|\, P_b^\dagger \hat{\mu} P_c \,|\Psi(t)\rangle + c.c.$) are shown in Figure 5.9. Overall, the variation in this contribution is small and, hence, it is not important for our understanding of the dynamic features in the total susceptibility. We observe a low field-contribution (at the beginning and end of the pulse), a field envelope following negative contribution, and small deviations at higher intensities. While the overall offset is due to the first order linear term to the susceptibility, the field envelope following negative contributions result from the third order term. The negative shape is likely due to a phase difference between the third order perturbative population in the continuum and the ground state with which it is interacting (i.e. the $\langle\psi^{(3)}(t)|\, \hat{\mu} \,|\psi^{(0)}(t)\rangle$ term in the dipole moment). The deviations of this shape at higher intensities are likely due to non-perturbative effects.

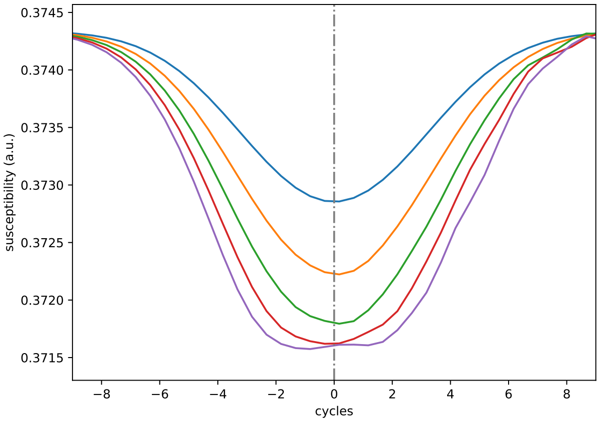

Figure 5.9: Cross-term contributions to the susceptibility: (100 TWcm^{-2} (purple), 150 TWcm^{-2} (red), 200 TWcm^{-2} (green), 250 TWcm^{-2} (orange), and 300 TWcm^{-2} (blue) pulses.) Note the large offset but subsequent small dip in the susceptibility. The dynamic variation here is much less for high intensities than for the bound states or the continuum states.

5.3.4 Populations and susceptibilities for high and low angular momentum

As mentioned previously, we attribute part of the (nonadiabatic) signatures in the total susceptibility at high intensities as due to the transition to a nonperturbative interaction of the field with the target atom. In particular, the population of the continuum states clearly shows features of the nonperturbative interaction, e.g. the exponential growth in continuum state population over a short interaction time.

While it is difficult to separate perturbative and nonperturbative effects in our ab-initio calculations, we noted another interesting signature of the transition between the corresponding regimes. This is the population of excited bound states with angular momentum quantum number larger than 1. To show this characteristic feature we present in Figure 5.10 the population in the excited bound states, recorded at the zeroes of the field, as a function of interaction: (a) for all states with $l = 1$ and (b) for all states with $l > 1$. At all intensities considered, we note that the population in the p states (Figure 5.10(a)) mainly adiabatically follows the field envelope, while the population in the higher l states appears in the trailing part of the pulse. Moreover, the latter population is predominantly observed at higher intensities. This effect reminds of various previous

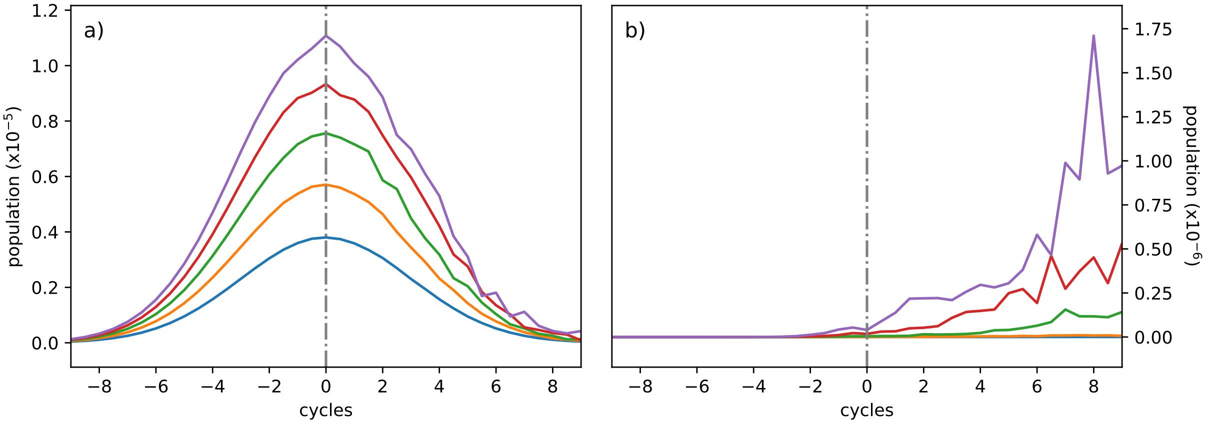

Figure 5.10: Excited state population, for (a) $l \leq 1$ and (b) $l > 1$. The lines represent results of calculations for 100 TWcm^{-2} (purple), 150 TWcm^{-2} (red), 200 TWcm^{-2} (green), 250 TWcm^{-2} (orange), and 300 TWcm^{-2} (blue) pulses.

studies [69, 98, 99] in which the trapping of population in excited states via transition from the continuum in the trailing part of the pulse has been observed and analyzed. Here, our results show that this excited population has significant contributions from states with $l \geq 2$.

Indeed, a similar and with respect to the susceptibility even more significant effect is found for the continuum states. In Figures 5.11 (population) and 5.12 (susceptibility) we present the distributions for states with small (panels (a): $l \leq 1$) and large (panels (b): $l \geq 2$) angular quantum numbers. As noticed before for the excited states, it is the population in the states with larger angular momentum quantum numbers which exhibit the nonadiabatic and nonperturbative characteristic features both in the population and in the contribution to the susceptibility. Interestingly, in the case of the continuum the contributions from the higher l states are by far the dominant ones at high intensities, giving rise to the signatures observed in the previous results (see Figure 5.7 for the continuum-continuum contributions and Figure 5.5 for the total susceptibility).

The continuum population at the zeros of the field exhibits classic non-perturbative behavior at 3×10^{14} W/cm^2: the growth in population is well described by an exponential curve. This non-perturbative ionization corresponds with both the onset of a negative contribution to the

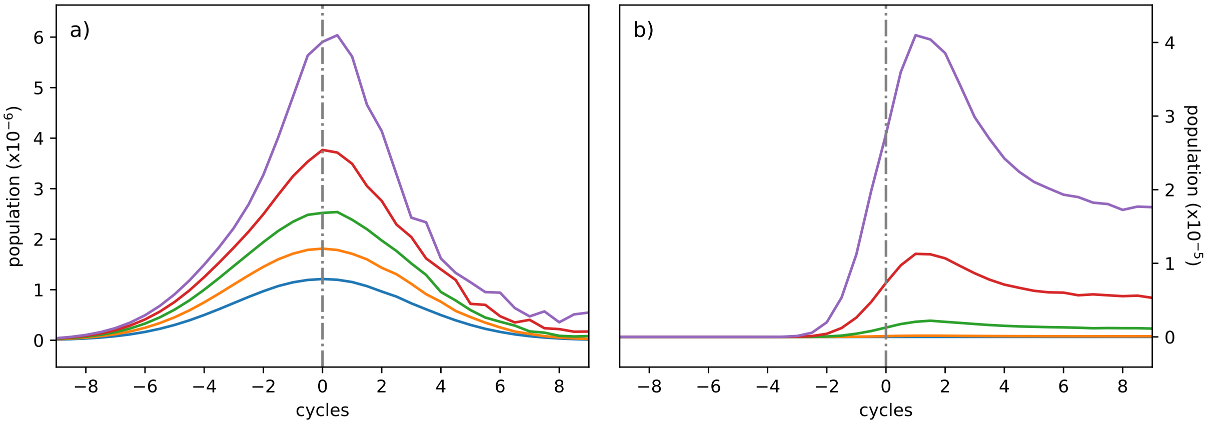

Figure 5.11: Continuum population, for (a) $l \leq 1$ and (b) $l > 1$ on the right. The lines represent results of calculations for $100\,\mathrm{TWcm}^{-2}$ (purple), $150\,\mathrm{TWcm}^{-2}$ (red), $200\,\mathrm{TWcm}^{-2}$ (green), $250\,\mathrm{TWcm}^{-2}$ (orange), and $300\,\mathrm{TWcm}^{-2}$ (blue) pulses. Note the difference in the time dependence on the left, and on the right

susceptibility and the breakdown in the susceptibility as shown in the previous Chapter, where at 3×10^{14} W/cm^2 the ab-initio susceptibility separates from the perturbative susceptibility.

5.4 Conclusion

In this Chapter, we have extended our analysis of the nonlinear susceptibility towards its time dependence during the interaction of helium atom with a laser pulse. In our study, we focus on the intensity regime between 1×10^{14} and 3×10^{14} W/cm^2, in which we have previously identified the transition from perturbative to nonperturbative light-matter interaction. In agreement with recent experimental data, our theoretical results show several deviations from the adiabatic dependence of the susceptibility on the field envelope that would be expected for a perturbative interaction. In particular, we observe a shift of the maximum in the susceptibility towards times before the center of the pulse and a change in the slope of the results in the trailing part. We identify that both characteristic features are due to the onset of nonperturbative multiphoton ionization, the strong population of the continuum and the transition of the population back from the continuum into excited states. Moreover, our analysis shows that states with a higher angular quantum number ($l \geq 1$) are significantly populated at higher intensities, which provides a signature for the nonperturbative interaction leading to the deviations from the typical adiabatic shape of the susceptibility as a function of time.

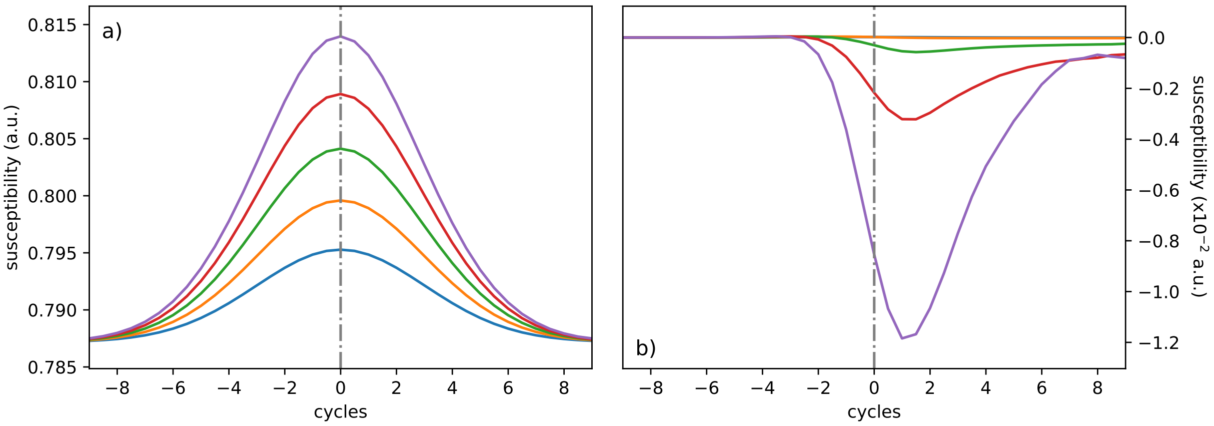

Figure 5.12: The total susceptibility, split up into $l \leq 1$ on the left and $l > 1$ on the right. From top to bottom, the lines represent 100TWcm^{-2} (purple), 150TWcm^{-2} (red), 200TWcm^{-2} (green), 250TWcm^{-2} (orange), and 300TWcm^{-2} (blue) pulses. The features we previously associated with the continuum are completely absent in the $l \leq 1$ susceptibility, instead they show up in the higher l states.

Chapter 6

Conclusions

In this thesis, we have examined the response of matter to a strong light pulse, via an analysis of the electrical susceptibility of atoms at intensities in the transition regime between the perturbative and non-perturbative atom-field interaction. In Chapter 1 we discussed the introduction of the higher order Kerr effect as a mechanism to explain the physics of filamentation. Filamentation is a phenomenon that occurs when propagating intense, short laser pulses in media. When the power of the pulse is large enough, the beam will undergo self-focusing where the higher intensity parts of the beam will induce a higher index of refraction than the lower intensity parts. This self-focusing will continue until ionization occurs, at which point the ionized electrons will defocus the beam until the intensity has decreased enough to let self-focusing dominate again. The ionization and defocusing of this process involve what have traditionally been understood as non-perturbative processes – e.g. above threshold ionization, high harmonic generation and multiphoton ionization. The process of filamentation has been long understood in terms of this focus, defocus cycle until Loriot et al. [24] extracted out the terms of the index of refraction power series and found both negative and positive terms. This led to a series of articles that discussed the implications of such a series, including the possibility of ionization-free defocusing as a model of filamentation. This discussion provides the motivation of this thesis, as it raised a more fundamental question regarding the applicability of the perturbative series to a process that occurs simultaneously with well known non-perturbative physics.

Examining the perturbative series description and non-perturbative version of the susceptibility side-by-side requires a detailed understanding of the perturbative series. In Chapter 2 we gave brief review of perturbation theory, a discussion of the first few perturbative dipole moment terms and their corresponding susceptibilities, and some remarks about the relationship between the susceptibility and the index of refraction. we discussed the relationship between the terms of the perturbative index of refraction and the perturbative susceptibility, describing the nonlinear dependence of the index of refraction on the density of the media, while the susceptibility's linear dependence on the density makes for a more appropriate quantity for single atom calculations. The first few dipole moment terms describe linear polarization, sum and difference frequency generation, along with the non-resonant physics that we are interested in. Finally, we discussed how to find the susceptibilities from the dipole moment before describing the general form of the susceptibilities for an arbitrary order in the perturbation series.

The perturbative susceptibilities require the field-free basis states for calculation, the methods of obtaining this basis comprised the bulk of Chapter 3. This Chapter is where we outlined our method for finding the field-free energy basis states that we use for our *ab-initio* calculations along with our perturbative susceptibility calculations. The field-free basis was observed within a number of approximations to ease the numerical difficulties of solving the time dependent Schödinger equation in its most general form. We applied a single-active electron approximation as well as restricting ourselves to spherically symmetric potentials, in order to restrict ourselves to spherically separable problems in which we only need one dimension to solve numerically. From here, we used the Numerov method to find the radial eigenstates, relying on the spherical harmonics for our angular states. The dimensionality of our problem was further reduced by limiting ourselves to linear polarization of the external field. For the *ab-initio* method, we used a Crank-Nicholson method for time propagation. This allowed us to find both the perturbative susceptibilities – using the field-free basis and the general form of the susceptibilities in Chapter 2, and non-perturbative *ab-initio* susceptibilities from the dipole moment using the same theoretical framework.

In Chapter 4, we made a comparison of the perturbative susceptibilities and the non-perturbative *ab-initio* susceptibilities found using the *ab-initio* method. The perturbative series was shown to be positive for all terms calculated for helium and hydrogen (up to the 11th order perturbative correction or the sixth non-zero term in the series), which immediately countered the behavior seen in the higher order Kerr terms that Loriot et al. [24] found. We performed a comparison between the perturbative series and the susceptibilities found using the non-perturbative *ab-initio* method for a number of different intensities, and showed a clear threshold intensity for helium and hydrogen where the perturbative and the non-perturbative susceptibilities diverge. At this intensity, we can clearly state that the perturbative series no longer describes the physics of the system. We next extended this comparison to the third and fifth harmonics generated in hydrogen at longer wavelengths, where we found that the *ab-initio* calculation appeared to diverge from the perturbative prediction at lower intensities for higher harmonics.

Finally, we discussed the time dependent susceptibility in Chapter 5. Here, we used the short time Fourier transform to model the time dependent susceptibility. We examined the susceptibility of helium around the intensity that led to the divergence between the perturbative and non-perturbative susceptibilities in the previous Chapter. Our analysis focused on the features of the susceptibility that drive this deviation. We split the susceptibility into continuum-continuum, bound-bound and bound-continuum contributions using the field-free eigenstates to make the distinction. We showed that multiphoton ionization and the resultant ionized electrons in the continuum have the largest non-perturbative effect and cause the continuum-continuum susceptibility to be negative. The bound-bound contribution is shown to be dominated by perturbative behavior. This distinction was made more explicit by a separation into low ($l < 2$) and high ($l \geq 2$) angular momentum states. This separation showed that the perturbative behavior is confined to the low angular momentum states, even when the continuum is taken into account, while the susceptibility from the high angular momentum states is primarily non-perturbative. The population of the continuum, split along these same lines, supported this idea.

Bibliography

[1] T. H. Maiman. Stimulated Optical Radiation in Ruby. Nature, 187(4736):493–494, 1960.

[2] P. A. Franken, A. E. Hill, C. W. Peters, and G. Weinreich. Generation of optical harmonics. Physical Review Letters, 7(4):118–119, 1961.

[3] P. Agostini, F. Fabre, G. Mainfray, G. Petite, and N. K. Rahman. Free-free transitions following six-photon ionization of xenon atoms. Physical Review Letters, 42(17):1127–1130, 1979.

[4] M. Hercher. Laser-induced damage in transparent media. Journal of the Optical Society of America, 54(563), 1964.

[5] G. Steinberg. Filamentary Tracks Formed in Transparent Optical Glass by Laser Beam Self-Focusing. I. Experimental Investigation*. Physical Review A, 4(3):1182–1194, 1971.

[6] E. L. Kerr. Filamentary Tracks Formed in Transparent Optical Glass by Laser Beam Self-Focusing. II. Theoretical Analysis*. Physical Review A, 4(3):1195–1218, 1971.

[7] C. G. Morgan. Laser-induced breakdown of gases. Reports on Progress in Physics, 38(5):621–665, 1975.

[8] A. Braun, G. Korn, X. Liu, D. Du, J. Squier, and G. Mourou. Self-channeling of high-peak-power femtosecond laser pulses in air. Optics Letters, 20(1):73–75, 1995.

[9] E. T. Nibbering, P. F. Curley, G. Grillon, B. S. Prade, M. A. Franco, F. Salin, and A. Mysyrowicz. Conical emission from self-guided femtosecond pulses in air. Optics Letters, 21(1):62–65, 1996.

[10] B. La Fontaine, F. Vidal, Z. Jiang, C. Y. Chien, D. Comtois, A. Desparois, T. W. Johnston, J.-C. Kieffer, H. Pépin, H. P. Mercure, H. Pepin, and H. P. Mercure. Filamentation of ultrashort pulse laser beams resulting from their propagation over long distances in air. Physics of Plasmas, 6(5):1615, 1999.

[11] G. Méchain, A. Couairon, Y.-B. André, C. D'Amico, M. Franco, B. Prade, S. Tzortzakis, A. Mysyrowicz, and R. Sauerbrey. Long-range self-channeling of infrared laser pulses in air: a new propagation regime without ionization. Applied Physics B, 79(3):379–382, 2004.

[12] J. E. Rothenberg. Space-time focusing: breakdown of the slowly varying envelope approximation in the self-focusing of femtosecond pulses. Optics Letters, 17(19):1340, 1992.

[13] C. P. Hauri, W. Kornelis, F. W. Helbing, A. Heinrich, A. Couairon, A. Mysyrowicz, J. Biegert, and U. Keller. Generation of intense, carrier-envelope phase-locked few-cycle laser pulses through filamentation. Applied Physics B: Lasers and Optics, 79(6):673–677, 2004.

[14] S. Tzortzakis, G. Méchain, G. Patalano, Y.-B. André, B. Prade, M. Franco, A. Mysyrowicz, J.-M. Munier, M. Gheudin, G. Beaudin, and P. Encrenaz. Coherent subterahertz radiation from femtosecond infrared filaments in air. Optics Letters, 27(21):1944–1946, 2002.

[15] A. Couairon and A. Mysyrowicz. Femtosecond filamentation in transparent media. Physics Reports, 441(2-4):47–189, 2007.

[16] A. Becker, N. Aközbek, K. Vijayalakshmi, E. Oral, C.M. Bowden, and S.L. Chin. Intensity clamping and re-focusing of intense femtosecond laser pulses in nitrogen molecular gas. Applied Physics B, 73(3):287–290, 2001.

[17] M. Ferray, A. L'Huillier, X. F. Li, L. A. Lompre, G. Mainfray, and C. Manus. Multiple-harmonic conversion of 1064 nm radiation in rare gases. Journal of Physics B: Atomic, Molecular and Optical Physics, 21(3):L31–L35, 1999.

[18] R. W. Boyd. Nonlinear Optics, Third Edition. Academic Press, 3rd edition, 2008.

[19] J. H. Marburger. Self-focusing: Theory. Progress in Quantum Electronics, 4:35–110, 1975.

[20] Á Börzsönyi, Z. Heiner, A. P. Kovács, M. P. Kalashnikov, and K. Osvay. Measurement of pressure dependent nonlinear refractive index of inert gases. Optics Express, 18(25):25847–25854, 2010.

[21] H. Lange, A. Chiron, J.-F. Ripoche, A. Mysyrowicz, P. Breger, and P. Agostini. High-Order Harmonic Generation and Quasiphase Matching in Xenon Using Self-Guided Femtosecond Pulses. Physical Review Letters, 81(8):1611–1613, 1998.

[22] P. B. Corkum. Plasma perspective on strong field multiphoton ionization. Physical Review Letters, 71(13):1994–1997, 1993.

[23] F. H. M. Faisal. Theory of Multiphoton Processes. Springer Science+Business Media, LLC, New York, New York, USA, 1987.

[24] V. Loriot, E. Hertz, O. Faucher, and B. Lavorel. Measurement of high order Kerr refractive index of major air components. Optics Express, 17(16):13429–13434, 2009.

[25] P. Béjot, J. Kasparian, S. Henin, V. Loriot, T. Vieillard, E. Hertz, O. Faucher, B. Lavorel, and J. P. Wolf. Higher-Order Kerr Terms Allow Ionization-Free Filamentation in Gases. Physical Review Letters, 104(10):103903, 2010.

[26] P. Béjot, E. Hertz, J. Kasparian, B. Lavorel, J. P. Wolf, and O. Faucher. Transition from Plasma-Driven to Kerr-Driven Laser Filamentation. Physical Review Letters, 106(24):243902, 2011.

[27] W. Ettoumi, P. Béjot, Y. Petit, V. Loriot, E. Hertz, O. Faucher, B. Lavorel, J. Kasparian, and J. P. Wolf. Spectral dependence of purely-Kerr-driven filamentation in air and argon. Physical Review A, 82(3):33826, 2010.

[28] V. Loriot, P. Béjot, W. Ettoumi, Y. Petit, J. Kasparian, S. Henin, E. Hertz, B. Lavorel, O. Faucher, and J. P. Wolf. On negative higher-order Kerr effect and filamentation. Laser Physics, 21(7):1319–1328, 2011.

[29] C. Köhler, R. Guichard, E. Lorin, S. Chelkowski, A. D. Bandrauk, L. Bergé, and S. Skupin. Saturation of the nonlinear refractive index in atomic gases. Physical Review A, 87(4):43811, 2013.

[30] E. A. Volkova, A. M. Popov, and O. V. Tikhonova. Nonlinear polarization response of an atomic gas medium in the field of a high-intensity femtosecond laser pulse. JETP Letters, 94(7):519–524, 2011.

[31] C. Bree, A. Demircan, and G. Steinmeyer. Method for Computing the Nonlinear Refractive Index via Keldysh Theory. IEEE Journal of Quantum Electronics, 46(4):433–437, 2010.

[32] C. Bree, A. Demircan, and G. Steinmeyer. Saturation of the All-Optical Kerr Effect. Physical Review Letters, 106(18):183902, 2011.

[33] M. Kolesik, E. M. Wright, and J. V. Moloney. Femtosecond filamentation in air and higher-order nonlinearities. Optics Letters, 35(15):2550–2552, 2010.

[34] J. Ni, J. Yao, B. Zeng, W. Chu, G. Li, H. Zhang, C. Jing, S. L. Chin, Y. Cheng, and Z. Xu. Comparative investigation of third- and fifth-harmonic generation in atomic and molecular gases driven by midinfrared ultrafast laser pulses. Physical Review A, 84(6):063846, 2011.

[35] G. O. Ariunbold, P. Polynkin, and J. V. Moloney. Third and fifth harmonic generation by tightly focused femtosecond pulses at 2.2 μm wavelength in air. Optics Express, 20(2):1662–1667, 2012.

[36] P. N. Butcher and D. Cotter. The Elements of Nonlinear Optics. Cambridge University Press, New York, New York, USA, 1990.

[37] K. C. Kulander, F. H. Mies, and K. J. Schafer. Model for studies of laser-induced nonlinear processes in molecules. Physical Review A, 53(4):2562–2570, 1996.

[38] M. P. de Boer and H. G. Muller. Observation of large populations in excited states after short-pulse multiphoton ionization. Physical Review Letters, 68(18):2747–2750, 1992.

[39] I. A. Ivanov and A. S. Kheifets. Harmonic generation for atoms in fields of varying ellipticity: Single-active-electron model with Hartree-Fock potential. Physical Review A, 79(5):053827, 2009.

[40] J. B. Krieger, Y. Li, and G. J. Iafrate. Systematic approximations to the optimized effective potential: Application to orbital-density-functional theory. Physical Review A, 46(9):5453–5458, 1992.

[41] X.-M. Tong and S.-I. Chu. Density-functional theory with optimized effective potential and self-interaction correction for ground states and autoionizing resonances. Physical Review A, 55(5):3406–3416, 1997.

[42] M. Abu-samha and L. B. Madsen. Single-active-electron potentials for molecules in intense laser fields. Physical Review A, 81(3):033416, 2010.

[43] X. M. Tong and C. D. Lin. Empirical formula for static field ionization rates of atoms and molecules by lasers in the barrier-suppression regime. Journal of Physics B: Atomic, Molecular and Optical Physics, 38(15):2593–2600, 2005.

[44] P. M. Morse and H. Feshbach. Methods of theoretical physics. International series in pure and applied physics. McGraw-Hill, New York, NY, 1953.

[45] T. E. Simos. A Numerov-type method for the numerical solution of the radial Schrödinger equation. Applied Numerical Mathematics, 7(2):201–206, 1991.

[46] G. Beylkin, M. J. Mohlenkamp, and F. Pérez. Approximating a wavefunction as an unconstrained sum of Slater determinants. Journal of Mathematical Physics, 49(3):032107, 2008.

[47] C. J. Cramer. Essentials of Computational Chemistry: Theories and Models. Wiley, 2013.

[48] R. J. LeVeque. Finite Difference Methods for Ordinary and Partial Differential Equations. Steady-State and Time-Dependent Problems. SIAM, 2007.

[49] L. Jianchun, G. A. Pope, and K. Sepehrnoori. A high-resolution finite-difference scheme for nonuniform grids. Applied mathematical modelling, 19(3):162–172, 1995.

[50] E. Tadmor. A Review of Numerical Methods for Nonlinear Partial Differential Equations. Bulletin of the American Mathematical Society, 49(4):507–554, 2012.

[51] M. Soriano and J. J. Palacios. Theory of projections with non-orthogonal basis sets: Partitioning techniques and effective Hamiltonians. Physical Review B, 90(7):075128, 2014.

[52] H. A. Bethe and E. E. Salpeter. Quantum mechanics of one- and two-electron atoms. Plenum, New York, NY, 1977.

[53] H. Bachau, E. Cormier, P. Decleva, J. E. Hansen, and F. Martín. Applications of B-splines in atomic and molecular physics. Reports on Progress in Physics, 64(12):1815–1943, 2001.

[54] C. de Boor. A Practical Guide to Splines. Springer, 2001.

[55] F. Martín. Ionization and dissociation using B-splines: Photoionization of the hydrogen molecule. Journal of Physics B: Atomic, Molecular and Optical Physics, 32(16):R197–R231, 1999.

[56] O. Zatsarinny and K. Bartschat. The B-spline R-matrix method for atomic processes: application to atomic structure, electron collisions and photoionization. Journal of Physics B: Atomic, Molecular and Optical Physics, 46(11):112001, 2013.

[57] J. C. Slater. Atomic Shielding Constants. Physical Review, 36(1):57, 1930.

[58] S. Datta. Evaluation of Coulomb integrals with hydrogenic and Slater-type orbitals. Journal of Physics B: Atomic and Molecular Physics, 18(5):853–857, 1985.

[59] W. J. Hehre, R. F. Stewart, and J. A. Pople. Self-Consistent Molecular-Orbital Methods. I. Use of Gaussian Expansions of Slater-Type Atomic Orbitals. The Journal of Chemical Physics, 2003.

[60] V. P. Majety, A. Zielinski, and A. Scrinzi. Photoionization of few electron systems: a hybrid coupled channels approach. New Journal of Physics, 17(6):063002, 2015.

[61] R. Kopold, W. Becker, M. Kleber, and G. G. Paulus. Channel-closing effects in high-order above-threshold ionization and high-order harmonic generation. Journal of Physics B: Atomic, Molecular and Optical Physics, 35(2):217–232, 2002.

[62] B. Yang, K. J. Schafer, B. Walker, K. C. Kulander, L. F. DiMauro, and P. Agostini. UP, 3UP, 11UP: Above-Threshold Ionization Revisited. Acta Physica Polonica A, 86(1-2):41–50, 1994.

[63] V. Pupyshev. The Lenz vector in the confined hydrogen atom problem. Chemical Physics Letters, 295(3):217–222, 1998.

[64] I. A. Stegun and M. Abramowitz. Handbook of mathematical functions with formulas, graphs, and mathematical tables. Dover books on intermediate advanced mathematics. U.S. National Bureau of Standards, New York, NY, 1964.

[65] M. Galassi, B. Gough, F. Rossi, M. Booth, G. Jungman, J. Theiler, and J. Davies. GNU Scientific Library. Reference Manual. Network Theory., 2001.

[66] L. N. Trefethen and D. Bau. Numerical Linear Algebra. Society for Industrial and Applied Mathematics, Philadelphia, PA, 1997.

[67] N. Michel, Bogoliubov Laboratory of Theoretical Physics JINR, J.-C. Str, Dubna, and Russia. Precise Coulomb wave functions for a wide range of complex ℓ, η and z. Computer Physics Communications, 176(3):232–249, 2007.

[68] A. Meurer, M. Paprocki, O. Čertík, M. Rocklin, S. Singh, R. P. Muller, F. Bonazzi, H. Gupta, S. Vats, F. Johansson, F. Pedregosa, M. J. Curry, A. R. Terrel, Š. Roučka, A. Saboo, I. Fernando, S. Kulal, R. Cimrman, and A. Scopatz. Sympy: Symbolic computing in python. PeerJ Computer Science, 3:e103, 2017.

[69] S. Chen, X. Gao, J. Li, A. Becker, and A. Jaroń-Becker. Application of a numerical-basis-state method to strong-field excitation and ionization of hydrogen atoms. Physical Review A, 86(1):013410–9, 2012.

[70] O. A. Sharafeddin, D. J. Kouri, and D. K. Hoffman. Time-dependent treatment of scattering: potential referenced and kinetic energy referenced modified Cayley approaches to atom–diatom collisions and time-scale separations. Canadian Journal of Chemistry, 70(2):686–692, 2011.

[71] J. Crank and P. Nicolson. A practical method for numerical evaluation of solutions of partial differential equations of the heat-conduction type [reprint of MR0019410 (8,409b)]. Advances in Computational Mathematics, 6(3-4):207–226 (1997), 1996.

[72] S. Balay, S. Abhyankar, M. F. Adams, J. Brown, P. Brune, K. Buschelman, L. Dalcin, V. Eijkhout, W. D. Gropp, D. Kaushik, M. G. Knepley, L. C. McInnes, K. Rupp, B. F. Smith, S. Zampini, and H. Zhang. PETSc Web page. `http://www.mcs.anl.gov/petsc`, 2016.

[73] S. Balay, S. Abhyankar, M. F. Adams, J. Brown, P. Brune, K. Buschelman, L. Dalcin, V. Eijkhout, W. D. Gropp, D. Kaushik, M. G. Knepley, L. C. McInnes, K. Rupp, B. F. Smith, S. Zampini, and H. Zhang. PETSc users manual. Technical Report ANL-95/11 - Revision 3.7, Argonne National Laboratory, 2016.

[74] S. Balay, W. D. Gropp, L. C. McInnes, and B. F. Smith. Efficient management of parallelism in object oriented numerical software libraries. In E. Arge, A. M. Bruaset, and H. P. Langtangen, editors, Modern Software Tools in Scientific Computing, pages 163–202. Birkhäuser Press, 1997.

[75] M. Nurhuda, A. Suda, and K. Midorikawa. Saturation of dynamic nonlinear susceptibility of noble gas atom in intense laser field. RIKEN REVIEW, (48):40–43, 2002.

[76] M. Nurhuda, A. Suda, and K. Midorikawa. Generalization of the Kerr effect for high intensity, ultrashort laser pulses. New Journal of Physics, 10(5):053006, 2008.

[77] A. McPherson, G. Gibson, H. Jara, U. Johann, T. S. Luk, I. A. McIntyre, K. Boyer, and C. K. Rhodes. Studies of multiphoton production of vacuum-ultraviolet radiation in the rare gases. Journal of the Optical Society of America B, 4(4):595–601, 1987.

[78] X. F. Li, A. L'Huillier, M. Ferray, L. A. Lompre, and G. Mainfray. Multiple-harmonic generation in rare gases at high laser intensity. Physical Review A, 39(11):5751–5761, 1989.

[79] A. Spott, A. Jaroń-Becker, and A. Becker. Ab initio and perturbative calculations of the electric susceptibility of atomic hydrogen. Physical Review A, 90(1):013426, 2014.

[80] F. Eilenberger, M. Bache, and S. Minardi. Higher-order Kerr effect and harmonic cascading in gases. Optics Letters, 37(22):4612–4614, 2012.

[81] J. M. Brown, E. M. Wright, J. V. Moloney, and M. Kolesik. On the relative roles of higher-order nonlinearity and ionization in ultrafast light-matter interactions. Optics Letters, 37(10):1604–1606, 2012.

[82] D. C. Yost, T. R. Schibli, J. Ye, J. L. Tate, J. Hostetter, M. B. Gaarde, and K. J. Schafer. Vacuum-ultraviolet frequency combs from below-threshold harmonics. Nature Physics, 5(11):815–820, 2009.

[83] C. H. García. Coherent attosecond light sources based on high-order harmonic generation: influence of the propagation effects. PhD thesis, Salamanca, 2013.

[84] A. Rundquist, C. G. Durfee, Z Chang, C. Herne, S. Backus, M. M. Murnane, and H. C. Kapteyn. Phase-Matched Generation of Coherent Soft X-rays. Science, 280(5368):1412–1415, 1998.

[85] J. A. Armstrong, N. Bloembergen, J. Ducuing, and P. S. Pershan. Interactions between Light Waves in a Nonlinear Dielectric. Physical Review, 127(6):1918–1939, 1962.

[86] C. Hernandez-Garcia, T. Popmintchev, M. M. Murnane, H. C. Kapteyn, L. Plaja, A. Becker, and A. Jaroń-Becker. Group velocity matching in high-order harmonic generation driven by mid-infrared lasers. New Journal of Physics, 18(7):073031–10, 2016.

[87] T. Popmintchev, M.-C. Chen, A. Bahabad, M. Gerrity, P. Sidorenko, O. Cohen, M. M. Christov, I. P. Murnane, and H. C. Kapteyn. Phase matching of high harmonic generation in the soft and hard X-ray regions of the spectrum. Proceedings of the National Academy of Sciences, 106(26):10516–10521, 2009.

[88] T. Popmintchev, M.-C. Chen, P. Arpin, M. M. Murnane, and H. C. Kapteyn. The attosecond nonlinear optics of bright coherent X-ray generation. Nature Photonics, 4(12):822–832, 2010.

[89] T. Popmintchev, M. C. Chen, D. Popmintchev, P. Arpin, S. Brown, S. Alisauskas, G. Andriukaitis, T. Balciunas, O. D. Mucke, A. Pugzlys, A. Baltuska, B. Shim, S. E. Schrauth, A. Gaeta, C. Hernandez-Garcia, L. Plaja, A. Becker, A. Jaroń-Becker, M. M. Murnane, and H. C. Kapteyn. Bright Coherent Ultrahigh Harmonics in the keV X-ray Regime from Mid-Infrared Femtosecond Lasers. Science, 336(6086):1287–1291, 2012.

[90] D. Popmintchev, C. Hernandez-Garcia, F. Dollar, C. Mancuso, J. A. Perez-Hernandez, M. C. Chen, A. Hankla, X. Gao, B. Shim, A. L. Gaeta, M. Tarazkar, D. A. Romanov, R. J. Levis, J. A. Gaffney, M. Foord, S. B. Libby, A. Jaroń-Becker, A. Becker, L. Plaja, M. M. Murnane, H. C. Kapteyn, and T. Popmintchev. Ultraviolet surprise: Efficient soft x-ray high-harmonic generation in multiply ionized plasmas. Science, 350(6265):1225–1231, 2015.

[91] J. K. Wahlstrand, Y. H. Cheng, and H. M. Milchberg. High Field Optical Nonlinearity and the Kramers-Kronig Relations. Physical Review Letters, 109(11):113904, 2012.

[92] J. K. Wahlstrand, Y. H. Cheng, Y. H. Chen, and H. M. Milchberg. Optical Nonlinearity in Ar and N_{2} near the Ionization Threshold. Physical Review Letters, 107(10):103901, 2011.

[93] J. K. Wahlstrand and H. M. Milchberg. Effect of a plasma grating on pump-probe experiments near the ionization threshold in gases. Optics Letters, (3):3, 2011.

[94] J. Allen. Short term spectral analysis, synthesis, and modification by discrete Fourier transform. IEEE Transactions on Acoustics, Speech, and Signal Processing, 25(3):235–238, 1977.

[95] G. DAntona and A. Ferrero. Digital Signal Processing for Measurement Systems. Theory and Applications. Springer Science & Business Media, 2006.

[96] F. J. Harris. On the use of windows for harmonic analysis with the discrete Fourier transform. Proceedings of the IEEE, 66(1):51–83, 1978.

[97] P. Lynch. The Dolph–Chebyshev window: A simple optimal filter. Monthly weather review, 125(4):655–660, 1997.

[98] R. R. Jones, D. W. Schumacher, and P. H. Bucksbaum. Population trapping in Kr and Xe in intense laser fields. Physical Review A, 47(1):R49–R52, 1993.

[99] T. Nubbemeyer, K. Gorling, A. Saenz, U. Eichmann, and W. Sandner. Strong-Field Tunneling without Ionization. Physical Review Letters, 101(23):233001, 2008.